# การศึกษาพลศาสตร์ของไหลเชิงคำนวณของกระบวนการรีฟอร์มมิงของมีเทน/เอทานอลด้วยไอน้ำที่เสริมด้วยการดูดซับ ในระบบฟลูอิไดซ์เบดแบบหมุนเวียน

นายเกียรติคุณ เผือกพ่วง

วิทยานิพนธ์นี้เป็นส่วนหนึ่งของการศึกษาตามหลักสูตรปริญญาวิศวกรรมศาสตรดุษฎีบัณฑิต
สาขาวิชาวิศวกรรมเคมี ภาควิชาวิศวกรรมเคมี
คณะวิศวกรรมศาสตร์ จุฬาลงกรณ์มหาวิทยาลัย
ปีการศึกษา 2560

# COMPUTATIONAL FLUID DYNAMIC STUDY OF SORPTION ENHANCED STEAM REFORMING OF METHANE/ETHANOL IN CIRCULATING FLUIDIZED BED SYSTEM

Mr. Kiattikhoon Phuakpunk

A Dissertation Submitted in Partial Fulfillment of the Requirements
for the Degree of Doctor of Engineering Program in Chemical Engineering
Department of Chemical Engineering
Faculty of Engineering
Chulalongkorn University
Academic Year 2017

| | |
|---|---|
| Thesis Title | COMPUTATIONAL FLUID DYNAMIC STUDY OF SORPTION ENHANCED STEAM REFORMING OF METHANE/ ETHANOL IN CIRCULATING FLUIDIZED BED SYSTEM |
| By | Mr. Kiattikhoon Phuakpunk |
| Field of Study | Chemical Engineering |
| Thesis Advisor | Professor Suttichai Assabumrungrat, Ph.D. |
| Thesis Co-Advisor | Associate Professor Benjapon Chalermsinsuwan, Ph.D.<br>Assistant Professor Sompong Putivisutisak, Ph.D. |

Accepted by the Faculty of Engineering, Chulalongkorn University in Partial Fulfillment of the Requirements for the Doctoral Degree

------------------------------------------------------------Dean of the Faculty of Engineering

(Associate Professor Supot Teachavorasinskun, D.Eng.)

THESIS COMMITTEE

----------------------------------------------------------------------Chairman

(Associate Professor Tawatchai Charinpanitkul, D.Eng.)

----------------------------------------------------------------------Thesis Advisor

(Professor Suttichai Assabumrungrat, Ph.D.)

----------------------------------------------------------------------Thesis Co-Advisor

(Associate Professor Benjapon Chalermsinsuwan, Ph.D.)

----------------------------------------------------------------------Thesis Co-Advisor

(Assistant Professor Sompong Putivisutisak, Ph.D.)

----------------------------------------------------------------------Examiner

(Akawat Sirisuk, Ph.D.)

----------------------------------------------------------------------Examiner

(Saran Salakij, Ph.D.)

----------------------------------------------------------------------External Examiner

(Assistant Professor Kaokanya Sudaprasert, Ph.D.)

เกียรติคุณ เผือกพ่วง : การศึกษาพลศาสตร์ของไหลเชิงคำนวณของกระบวนการรีฟอร์มมิงของมีเทน/เอทานอลด้วยไอน้ำที่เสริมด้วยการดูดซับ ในระบบฟลูอิไดซ์เบดแบบหมุนเวียน ( COMPUTATIONAL FLUID DYNAMIC STUDY OF SORPTION ENHANCED STEAM REFORMING OF METHANE/ETHANOL IN CIRCULATING FLUIDIZED BED SYSTEM) อ.ที่ปรึกษาวิทยานิพนธ์หลัก: ศ. ดร.สุทธิชัย อัสสะบำรุงรัตน์, อ.ที่ปรึกษาวิทยานิพนธ์ร่วม: รศ. ดร.เบญจพล เฉลิมสินสุวรรณ, ผศ. ดร.สมพงษ์ พุทธิวิสุทธิศักดิ์, 162 หน้า.

แบบจำลองพลศาสตร์ของไหลเชิงคำนวณในสองมิติถูกนำมาใช้ออกแบบระบบต้นแบบของกระบวนการรีฟอร์มมิงด้วยไอน้ำที่เสริมด้วยการดูดซับของมีเทน (Sorption enhanced steam methane reforming, SESMR) และของเอทานอล (Sorption enhanced steam reforming of ethanol, SESRE) ในระบบฟลูอิไดซ์เบดแบบหมุนเวียนที่ของแข็งในระบบประกอบด้วยตัวเร่งปฏิกิริยาชนิดผสมนิกเกิล และโดโลไมต์ที่เป็นตัวดูดซับ โดยแบ่งระบบออกมาศึกษาเป็นสามส่วน ได้แก่ ท่อตั้ง (Riser) ที่เกิดปฏิกิริยา SESMR ท่อตั้งที่เกิดปฏิกิริยา SESRE และถังฟื้นฟูตัวดูดซับ (Regenerator) ในส่วนของท่อตั้งที่เกิดปฏิกิริยา SESMR พบว่าสามารถผลิตไฮโดรเจนได้บริสุทธิ์สูงสอดคล้องกับค่าสูงสุดตามทฤษฎี ถึง 98.58% ของแก๊สแห้ง และได้ฟลักซ์การไหลออกของไฮโดรเจนสูงสุดถึง 0.301 กิโลกรัมต่อตารางเมตรวินาที เมื่อดำเนินกระบวนการด้วยอัตราส่วนไอน้ำต่อมีเทนที่ 4 โมลต่อโมล ความเร็วการไหลเข้าของแก๊สที่ 6 เมตรต่อวินาที อุณหภูมิขาเข้าของสารเท่ากับ 581 องศาเซลเซียส ในขณะที่ส่วนของท่อตั้งที่เกิดปฏิกิริยา SESRE พบว่าสามารถผลิตไฮโดรเจนได้บริสุทธิ์สูงสุดเพียง 91.30% ของแก๊สแห้ง และได้ฟลักซ์การไหลออกของไฮโดรเจนสูงสุด 0.147 กิโลกรัมต่อตารางเมตรวินาที เมื่อดำเนินกระบวนการด้วยอัตราส่วนไอน้ำต่อเอทานอลที่ 6 โมลต่อโมล ความเร็วการไหลเข้าของแก๊สที่ 3 เมตรต่อวินาที อุณหภูมิขาเข้าของสารเท่ากับ 600 องศาเซลเซียส โดยท่อตั้งของทั้งสองปฏิกิริยามีแบบที่ดีที่สุดเหมือนกัน คือ มีขนาดเส้นผ่านศูนย์กลาง 0.2 เมตร และสูง 7 เมตร ใช้ฟลักซ์การไหลเข้าของของแข็งเท่ากับ 200 กิโลกรัมต่อตารางเมตรวินาที ที่อัตราส่วนของตัวเร่งปฏิกิริยาต่อตัวดูดซับเท่ากับ 2.54 กิโลกรัมต่อกิโลกรัม ส่วนสุดท้ายที่ศึกษาคือส่วนของถังฟื้นฟูตัวดูดซับพบว่า ระบบถังฟื้นฟูเป็นแบบ 2 ขั้นที่แต่ละขั้นมีถังขนาดหน้าตัดกว้าง 1.2 เมตร และความสูงของเบดเท่ากับ 0.8 เมตร สามารถฟื้นฟูตัวดูดซับได้อย่างสมบูรณ์เมื่อดำเนินกระบวนการด้วยความเร็วการไหลเข้าของแก๊สที่ 0.2 เมตรต่อวินาที และของแข็งไหลเข้าด้วยอุณหภูมิ 950 องศาเซลเซียส ดังนั้น กระบวนการ SESMR และกระบวนการ SESRE มีความเป็นไปได้ที่จะผลิตไฮโดรเจนความบริสุทธิ์สูงและมีกำลังการผลิตสูงแบบต่อเนื่องได้ด้วยระบบฟลูอิไดซ์เบดแบบหมุนเวียนที่ออกแบบและดำเนินการดังในงานวิจัยนี้

| | | |
|---|---|---|
| ภาควิชา | วิศวกรรมเคมี | ลายมือชื่อนิสิต ........................................ |
| สาขาวิชา | วิศวกรรมเคมี | ลายมือชื่อ อ.ที่ปรึกษาหลัก ................................ |
| ปีการศึกษา | 2560 | ลายมือชื่อ อ.ที่ปรึกษาร่วม ................................ |
| | | ลายมือชื่อ อ.ที่ปรึกษาร่วม ................................ |

# # 5771404621 : MAJOR CHEMICAL ENGINEERING

KEYWORDS: SORPTION ENHANCED STEAM METHANE REFORMING / SORPTION ENHANCED STEAM REFORMING OF ETHANOL / COMPUTATIONAL FLUID DYNAMICS / CIRCULATING FLUIDIZED BED / MULTIPHASE FLOW MODELS / RISER / CALCIUM OXIDE REGENERATION / CALCINER

KIATTIKHOON PHUAKPUNK: COMPUTATIONAL FLUID DYNAMIC STUDY OF SORPTION ENHANCED STEAM REFORMING OF METHANE/ETHANOL IN CIRCULATING FLUIDIZED BED SYSTEM. ADVISOR: PROF. SUTTICHAI ASSABUMRUNGRAT, Ph.D., CO-ADVISOR: ASSOC. PROF. BENJAPON CHALERMSINSUWAN, Ph.D., ASST. PROF. SOMPONG PUTIVISUTISAK, Ph.D., 162 pp.

Two-dimensional fluid dynamic models were used to optimize and design a proper pilot-scale system for sorption enhanced steam methane reforming (SESMR) and sorption enhanced steam reforming of ethanol (SESRE) in a circulating fluidized bed reactor (CFBR) using Ni-based catalyst and dolomite as sorbent. The CFBR system was separately designed as 3 parts: including a SESMR riser, a SESRE and a regenerator. The SESMR riser could get $H_2$ purity reached equilibrium of 98.58% in dry basis with the highest $H_2$ flux of 0.301 kg/m$^2$s when operating with steam to carbon ratio of 4 mol/mol, gas velocity of 6 m/s, inlet temperature of 581°C. While the SESRE riser could get maximum $H_2$ purity only 91.30% in dry basis with the highest $H_2$ flux of 0.147 kg/m$^2$s when operating with steam to ethanol ratio of 6 mol/mol, gas velocity of 3 m/s, inlet temperature of 600°C. Both the risers for SESMR and SESRE had the best design with diameter of 0.2 m, height of 7 m operating with solid flux of 200 kg/m$^2$s and catalyst to sorbent ratio of 2.54 kg/kg. Lastly, in regenerator part, double-stage bubbling bed regenerators with 1.2 m width and 0.8 m height of bed could perfectly regenerate the sorbent when operating with gas velocity of 0.2 m/s and preheating the solids at 950°C. Overall, SESMR and SESRE had feasibility to continuously produce high purity with high production rate of $H_2$ by this preferred design and conditions of CFBR system.

Department: Chemical Engineering
Field of Study: Chemical Engineering
Academic Year: 2017

Student's Signature ....................................
Advisor's Signature ....................................
Co-Advisor's Signature ....................................
Co-Advisor's Signature ....................................

# ACKNOWLEDGEMENTS

First of all, the author would like to greatly appreciate his advisor, Professor Suttichai Assabumrungrat for a chance of this education, funding supports, encouragement, academic and non-academic helps, and always belief in the author until achieve the degree. Secondly, the author would like to appreciate his co-advisor, Associate Professor Benjapon Chalermsinsuwan, Ph.D., for guidelines and supervision, especially in this CFD and fluidization field, until complete this dissertation and get publications. Next, the author also would like appreciate another co-advisor, Assistant Professor Sompong Putivisutisak, Ph.D., for introducing the author to CFD field and other suggestions.

To complete this dissertation, the author would like to appreciate all other thesis committees including Associate Professor Tawatchai Charinpanitkul, D.Eng., as the chairman, Akawat Sirisuk, Ph.D., Saran Salakij, Ph.D., and Assistant Professor Kaokanya Sudaprasert, Ph.D., as the examiners for useful comments.

For publications, the author would like to acknowledge the Ratchadapisek Sompoch Endowment Fund (2016), Chulalongkorn University (CU-59-003-IC). This dissertation had been also supported by the Thailand Research Fund (RSA5980052), as well as the NSTDA Chair Professor Grant (No.5) funded by the Crown Property Bureau of Thailand and National Science and Technology Development Agency.

Furthermore, the author would like to announce his love to his wife, Wilasinee Phromsila, for all of supports, encouragement and shares in entire studying and living. The author also would like to announce his gratefulness to his father, mother and family for all supports.

Finally, the author would like to appreciate Energy Cluster, Chulalongkorn University cooperating with Chula Unisearch, Chulalongkorn University, and Energy Research Institute, Chulalongkorn University for a work in 2016-2017. The author also would like to appreciate Center of Excellence on Catalysis and Catalytic Reaction Engineering, Chulalongkorn University for facilities.

## CONTENTS

Page

Page

Page

# LIST OF TABLES

Table Page

## LIST OF FIGURES

# NOMENCLATURE

$C_D$ = Drag coefficient, [-]

$C_{fr,ls}$ = Friction coefficient between solid phases, [-]

$C_{p_g}$ = Heat capacity of gas phase, [$J \cdot kg^{-1} \cdot K^{-1}$]

$Cat/Sb$ = Catalyst to sorbent ratio, [$kg \cdot kg^{-1}$]

$D_{CO_2}^{m}$ = Molecular diffusion coefficient of $CO_2$, [$m^2 \cdot s$]

$d_p$ = Mean diameter of sorbent, [m]

$d_s$ = Particle diameter of solid phase, [m]

$e_{ss} \equiv e_{ls}$ = Restitution coefficient for solid-solid collisions, [-]

$\vec{F}_q$ = External body force to phase q, [$kg \cdot m^{-2} \cdot s^{-2}$, $N \cdot m^{-3}$]

$\vec{F}_{lift,q}$ = Lift force to phase q, [$kg \cdot m^{-2} \cdot s^{-2}$, $N \cdot m^{-3}$]

$\vec{F}_{vm,q}$ = Virtual mass force to phase q, [$kg \cdot m^{-2} \cdot s^{-2}$, $N \cdot m^{-3}$]

$\vec{F}_{td,q}$ = Turbulent dispersion force to phase q, [$kg \cdot m^{-2} \cdot s^{-2}$, $N \cdot m^{-3}$]

$\vec{F}_{wl,g}$ = Wall lubrication force to only gas phase, [$kg \cdot m^{-2} \cdot s^{-2}$, $N \cdot m^{-3}$]

$f_{drag}$ = Drag function

$G_s$ = Solid flux, [$kg \cdot m^{-2} \cdot s^{-1}$]

$\vec{g}$ = Gravity force, [$m \cdot s^{-2}$]

$g_{0,ls}$ = Radial distribution coefficient of mutual solid phases, [-]

$g_{0,ss}$ = Radial distribution coefficient of single solid phase, [-]

$H$ = Height of the riser, [m]

$H_g$ = Specific enthalpy of gas phase, [$m^2 \cdot s^{-2}$, $J \cdot kg^{-1}$]

$H_j$ = Specific enthalpy of species j in the reaction, [$m^2 \cdot s^{-2}$, $J \cdot kg^{-1}$]

$H_j^f$ = Specific heat of formation of species j in the reaction, [$m^2 \cdot s^{-2}$, $J \cdot kg^{-1}$]

$h_{sg} \equiv h_{gs}$ = Gas-solid interphase heat exchange coefficient, [$m^2 \cdot s^{-2}$, $J \cdot kg^{-1}$]

$\bar{I}$ = Unit tensor, [-]

$id$ = Diameter of the riser, [m]

$\vec{J}_k^q$ = Mass flux of species k into phase q, [$kg \cdot m^{-2} \cdot s^{-1}$]

$K_i$ = Equilibrium constants of reaction i

$K_k$ = Adsorption equilibrium constants of species k

$K_{ls} \equiv K_{sl}$ = Solid-solid interphase momentum exchange coefficient, [$kg \cdot m^{-3} \cdot s^{-1}$]

$K_{sg} \equiv K_{gs}$ = Gas-solid interphase momentum exchange coefficient, [$kg \cdot m^{-3} \cdot s^{-1}$]

$k_{carb}$ = Rate constants of carbonation

$k_g$ = Thermal conductivity of gas phase, [$W \cdot m^{-1} \cdot K^{-1}$]

$k_i$ = Rate constants of reaction i

$k_{\Theta_s}$ = Diffusion coefficient, [$m^2 \cdot s^{-1}$]

$M_j$ = Molecular weight of species j in the reaction, [$kg \cdot kmol^{-1}$]

$\dot{m}_{pq}$ = Mass transfer from phase p to phase q, [$kg \cdot m^{-3} \cdot s^{-1}$]

$Nu_s$ = Nusselt number of solid phase, [-]

$n$ = Degree of partial pressure, [-]

$n_k^{Sorbent}$ = Mole of species k in sorbent phase, [mol]

$Pr$ = Prandtl number of gas phase, [-]

$p$ = Static pressure, [Pa]

$p_{CO_2}$ = Partial pressure of $CO_2$, [Pa]

$p_{CO_2,eq}$ = Equilibrium pressures of $CO_2$, [Pa]

$p_g$ = Static pressure of gas phase, [Pa]

$p_k$ = Partial pressures of species k, [Pa]

$p_s$ = Solid pressure, [Pa]

$Q_{sg}$ = Intensity of heat exchange between solid phase and gas phase, [$W \cdot m^{-3}$]

$\vec{q}_g$ = Heat flux of gas phase, [$W \cdot m^{-2}$]

$\acute{R}$ = Rate of a heterogeneous reaction, [$kmol \cdot m^{-3} \cdot s^{-1}$]

$R_k^q$ = Net rate of species k produced by homogeneous reactions inside phase q, [$kg \cdot m^{-3} \cdot s^{-1}$]

$Re_p$ = Particle Reynolds number of sorbent phase, [-]

$Re_s$ = Particle Reynolds number of solid phase, [-]

$r_{carb}$ = Rate of carbonation, [$kmol \cdot kg_{sorb}^{-1} \cdot s^{-1}$]

$r_{deca}$ = Rate of decarbonation, [$kmol \cdot kg_{sorb}^{-1} \cdot s^{-1}$]

$r_i$ = Rates of reaction i on catalyst, [$kmol \cdot kg_{cat}^{-1} \cdot s^{-1}$]

$S_{h,g}$ = Heat source of gas phase, [$W \cdot m^{-3}$]

$S_k^q$ = Rate of creation of species k by addition from dispersed phase and other sources in phase q, [$kg \cdot m^{-3} \cdot s^{-1}$]

$S_{m,q}$ = Mass source of phase q, [$kg \cdot m^{-3} \cdot s^{-1}$]

$S_0$ = Initial specific surface area of CaO, [$m^2 \cdot kg_{sorb}^{-1}$]

S/C = Steam to carbon ratio, [$mol \cdot mol^{-1}$]

S/E = Steam/Ethanol molar ratio, [$mol \cdot mol^{-1}$]

Sc = Schmidt number, [-]

Sh = Sherwood number, [-]

$T_{in}$ = Temperature of inlets, [°C]

U = Gas inlet velocity, [$m \cdot s^{-1}$]

$U_{pg}$ = Particle-gas relative velocity, [$m \cdot s^{-1}$]

$\vec{v}_{ls}$ = Interphase velocity from phase l (solid or gas) to solid phase, [$m \cdot s^{-1}$]

$\vec{v}_q$ = Velocity of phase q, [$m \cdot s^{-1}$]

$\vec{v}_{r_j}$ = Velocity of a reactant j which involved in the reaction, [$m \cdot s^{-1}$]

$\vec{v}_{sg}$ = Interphase velocity from solid phase to gas phase, [$m \cdot s^{-1}$]

$X_{CaO}$ = Conversion of CaO, [-]

$x_k^{Sorbent}$ = Mole fraction of species k in sorbent phase, [-]

$Y_k^q$ = Mass fraction of species k in phase q, [-]

$\gamma_j$ = Stoichiometric coefficient of species j in the reaction, [-]

$\gamma_{\Theta_s}$ = Collisional dissipation of energy, [$W \cdot m^{-3}$]

$\varepsilon$ = Constant porosity of sorbent, [-]

$\varepsilon_q$ = Volume fraction of phase q, [-]

$\varepsilon_{s,max}$ = Maximum packing of solid phase, [-]

$\Theta_s$ = Granular temperature, [$m^2 \cdot s^{-2}$, $J \cdot kg^{-1}$]

$\lambda_q$ = Bulk viscosity of phase q, [$Pa \cdot s$]

$\lambda_s$ = Solid bulk viscosity, [$Pa \cdot s$]

$\mu_g$ = Viscosity of gas, [$kg \cdot m^{-1} \cdot s^{-1}$]

$\mu_q$ = Shear viscosity of phase q, [$Pa \cdot s$]

$\mu_s$ = Solid shear viscosity, [$Pa \cdot s$]

$\mu_{s,col}$ = Collisional viscosity of solid phase, [$Pa \cdot s$]

$\mu_{s,fr}$ = Friction viscosity of solid phase, [$Pa \cdot s$]

$\mu_{s,kin}$ = Kinetic viscosity of solid phase, [$Pa \cdot s$]

$\rho_g$ = Density of gas, [$kg \cdot m^{-3}$]

$\rho_p$ = Density of sorbent, [$kg \cdot m^{-3}$]

$\rho_q$ = Physical density of phase q, [$kg \cdot m^{-3}$]

$\bar{\bar{\tau}}_q$ = Stress tensor of phase q, [Pa]

$\tau_s$ = Particulate relaxation time in solid phase, [s]

$\phi_{ls}$ = Kinetic energy exchange between phase l (solid or gas) and solid phase, [W·m$^{-3}$]

# CHAPTER 1

# INTRODUCTION

## 1.1 Research background and signification

Nowadays, global fossil-fuel reservoirs are dramatically decreasing while the world’s energy-consumption tendency is higher. Hydrogen fuel is a promising alternative source. It has drawn widespread attention because it is a clean energy and can be derived from renewable energy sources. At end uses when $H_2$ is combusted in internal engines or fed in to fuel cells, only water is the outcome without emission of $CO_2$, a major cause of global warming (Joensen and Rostrup-Nielsen, 2002). However, hydrogen could not have been claimed totally renewable or green because its large-scale sources and productions come from petroleum industry.

Hydrogen is an element with the third-place amount in the world. Most of natural hydrogen does not exist in $H_2$ gas but is found in organic compounds. There are many organic compounds which can be converted into $H_2$ via many processes e.g. dehydrogenation, gasification and steam reforming. The steam reforming is the most effective process to produce $H_2$ in large scale.

Conventional industrial-level hydrogen production has used methane ($CH_4$), in natural gas or in tail gas from refinery process, as raw material via steam methane reforming (SMR) process. The conventional processes consist of three main sections i.e. reforming, shifting and gas separation (Harrison, 2008). In reforming and shifting section maximum $CH_4$ is converted to mainly $CO_2$ and $H_2$ (with little of CO) as overall reaction 1.1.

$$CH_4 + 2H_2O \rightleftharpoons CO_2 + 4H_2 \qquad \Delta H^{\circ}_{298} = +165.0 \text{ kJ/mol} \qquad (1.1)$$

In case that ethanol ($C_2H_5OH$) is a feed, $C_2H_5OH$ is also converted to mainly $CO_2$ and $H_2$ as overall reaction 1.2.

$$C_2H_5OH + 3H_2O \rightleftharpoons 2CO_2 + 6H_2 \qquad \Delta H^{\circ}_{298} = +173.4 \text{ kJ/mol} \qquad (1.2)$$

Thus, the conventional processes need the last section that consists of separation units, making conventional processes huge and complicated.

A new concept of steam reforming with sorption enhancement (SESR) has been raised because of advantages taken from that $CO_2$ can be adsorbed by sorbents in the same reforming reactor. First advantage is that equilibrium of reforming reactions (reactions 1.1 and 1.2) is shifted forward so more $H_2$ is produced and $CH_4/C_2H_5OH$ can be more completely converted. Another advantage is that effluent gas off the reformer has high $H_2$ purity reaching 99% (Harrison, 2008; Barelli *et al.*, 2008; Haryanto *et al.*, 2005; Cotton *et al.*, 2013; Rodrigues *et al.*, 2017) dry basis so separation units are unnecessary in the processes. But a disadvantage of SESR is discontinuous performance because when the sorbent is almost full of $CO_2$ captured, $H_2$ purity in effluent gas and feed conversion decrease to normal equilibrium of reforming reactions.

Several types of sorbent have been used and developed for $CO_2$ capture i.e. natural or pure metal oxides (e.g. CaO), akali mixed metal oxides (e.g. $Li_4SiO_4$) and hydrotalcite-like materials (HTCls). $CO_2$ capacity, rate of $CO_2$ caption and stability of the sorbents are important properties to performances of both sorption enhanced steam methane reforming (SESMR) and sorption enhanced steam reforming of ethanol (SESRE) (Barelli *et al.*, 2008; Haryanto *et al.*, 2005; Singh *et al.*, 2009). Advantages of natural CaO sorbents such as dolomite and limestone are inexpensive, easy to find and have higher $CO_2$ capacity than other sorbents but CaO sorbents have lower thermal cyclic stability than the others. Even though limestone has more $CO_2$ capacity than dolomite due to higher CaO content, but dolomite contains more MgO that makes dolomite more stable to cyclic usage (Comas *et al.*, 2004; Olivas *et al.*, 2014). Thus, dolomite is a suitable sorbent for large-scale processes of SESR which has to involve regeneration of the used sorbent. The reactions of $CO_2$ capture and regeneration of the dolomite is shown in reaction 1.3.

$$CaO + CO_2 \rightleftharpoons CaCO_3 \qquad \Delta H^{\circ}_{298} = -178 \text{ kJ/mol} \tag{1.3}$$

Due to the adsorption limits, SESR processes have been researched and developed mainly in two ways i.e. 1) improving sorbents with better properties and 2) developing and designing reactors/systems of the SESR processes for larger hydrogen production or better operation (lower materials or energy consumption).

Most of SESMR/SESRE reactors have still been typical fixed bed reactors in many researches and conventional processes. Because the single fixed reactor for SESR needs switching between reforming and regeneration period, this is complicated for operation and maintenance. So for continuous reforming in general fixed bed reactor, parallel reactors systems are typically applied (Lysikov *et al.*, 2015; Li *et al.*, 2006). In the meanwhile, fluidized bed reactors have been developed. Advantages of fluidized bed reactors over fixed bed reactors are lower pressure drop and more gas-solid (reactant-catalyst/sorbents) contacting throughout beds that give better mass and heat transfer. Bubbling bed reactors has been proved that give SESMR/SESRE performance as good as the fixed bed reactors (Chao *et al.*, 2012; Wang *et al.*, 2010; Johnsen *et al.*, 2006; Johnsen *et al.*, 2006) (Gayubo *et al.*, 2014; Vicente *et al.*, 2014). Nowadays, circulating fluidized bed reactors (CFBR) have been expected and developed for higher hydrogen production rate due to 1) using higher gas velocity i.e. higher feed and 2) blowing solid particles out of the reformer, also called a riser, that sorbent could been regenerated simultaneously in another unit. But due to high gas velocity, gas-solid contacting is theoretically non-uniform among dilute zone and dense zone. From these reasons, CFBR has unclear performance dependent on occurring regimes (Arstad *et al.*, 2012; Wang *et al.*, 2011; Rodríguez *et al.*, 2011). Thus, the CFBR system design has been interesting for SESMR/SESRE application with high efficiency as same as bubbling bed reactors.

In last decade, computational fluid dynamics (CFD) has been more interested and utilized in problems about fluid phenomena especially in system geometry design. CFD could give high accuracy and detailed results that could reduce time, resources and costs of experiment especially in large scales. Problem solving can be either in 2D or 3D models, results from 3D models were close to realistic but consumed much more computational demands and time than from 2D models. However in many cases especially in cylindrical geometry like the riser, 2D models could demonstrate sufficient accuracy details (Samruamphianskun *et al.*, 2012; Chalermsinsuwan *et al.*, 2014; Wu *et al.*, 2013; Wu *et al.*, 2014; Wang *et al.*, 2014). Thus, in this dissertation, CFD with 2D models were performed to design a pilot-scale CFBR system suitable for the highest hydrogen production via SESMR/SESRE by investigating the optimum design and reaction parameters.

## 1.2 Objective

To design a circulating fluidized bed reactor system for continuous hydrogen production via sorption enhanced steam reforming of methane (SESMR) and ethanol (SESRE).

### 1.3 Scopes of dissertation

1. CFBR systems were simulated in two-dimensional two-phase models combined with kinetic theory of granular flows (KTGF) which used for catalyst phase and sorbent phase.

2. Kinetics of steam reforming of methane and ethanol were chosen being based on Ni-based catalyst, while kinetics of carbonation and decarbonation were chosen being based on calcined dolomite.

3. Hydrogen production was operated in a circulating fluidized bed reactors (CFBR) system which consists of a riser (for SESMR/SESRE) as a reformer, a bubbling bed reactor (for decarbonation) as a regenerator and a 100% efficient cyclone connected.

4. Goal of the reforming riser design was to get maximum rate of hydrogen production with the perfect reaction performance i.e. $H_2$ purity of effluent gas should reach the equilibrium which fixed bed or bubbling bed reactors could get in experiments and CaO conversion of the sorbent should not be over 28% for stable $CO_2$ capture in continuous operation.

5. Goal of the regenerator design was to get CaO conversion of the sorbent nearly to 0% like fresh sorbent entering into the riser.

6. Parameters of the riser design to be investigated were chosen only the most effective including diameter, gas inlet velocity, inlet temperature, catalyst to sorbent ratio and solid flux.

7. Geometry design of the regenerator correlated with used solid resulted from the best designed riser of either SESMR or SESRE. Parameters to be investigated were only gas inlet velocity and inlet temperature of solid.

# CHAPTER 2

# THEORY AND LITERATURE REVIEW

## 2.1 Steam reforming processes

Generally, steam reforming is a term of complete hydrolysis or hydrocracking of hydrocarbons into smallest molecules (gases e.g. CO, $H_2$). Basic steam reforming reaction of generic hydrocarbon ($C_nH_m$) might be

$$C_nH_m + nH_2O \longrightarrow nCO + (m/2 + n)H_2 \qquad (2.1)$$

Steam reforming of various C2+ hydrocarbons often contains hydrocracking reaction to convert large hydrocarbon to methane and then methane is sequentially reformed to CO and $H_2$.

### 2.1.1 Steam methane reforming (SMR)

In case of methane, traditional steam methane reforming (SMR) processes contain three reversible reactions; steam reforming reactions of methane (reactions 2.2-2.3) and *"Water-gas shift reaction (WGS)"* (reaction 2.4).

$$CH_4 + H_2O \rightleftharpoons CO + 3H_2 \qquad \Delta H^\circ_{298} = +206.2 \text{ kJ/mol} \qquad (2.2)$$

$$CH_4 + 2H_2O \rightleftharpoons CO_2 + 4H_2 \qquad \Delta H^\circ_{298} = +165.0 \text{ kJ/mol} \qquad (2.3)$$

$$CO + H_2O \rightleftharpoons CO_2 + H_2 \qquad \Delta H^\circ_{298} = -41.2 \text{ kJ/mol} \qquad (2.4)$$

According to reaction 2.1, $CH_4$ is basically reformed to CO as reaction 2.2 called *"Basic SMR reaction (bSMR)"*. Then CO is shifted to $CO_2$ via WGS as reaction 2.4. The series of reaction 2.2 and 2.4 is totally equal to reaction 2.3, thus the reaction 2.3 is *"Overall reaction of SMR"* or could be called *"Global SMR reaction (gSMR)"*. However, in practice $CH_4$ is not only reformed through the reaction series, but also directly through the Global SMR reaction. By definition, SMR should contain only reaction 2.2 and 2.3 which $CH_4$ react with $H_2O$. But in almost works when SMR was mentioned, it was often well-known to consist of the WGS reaction as well.

To maximize hydrogen production, $CH_4$ should be converted as much as possible and CO should be mostly shifted to gain more $H_2$. Due to reversibility of SMR, it has to operates in proper conditions and steam to carbon ratio (S/C). Because both the reforming reactions are strongly endothermic but WGS is moderately exothermic, thus SMR has to perform on catalyst at high temperature but individual WGS is favored in lower temperature. Furthermore, the global reaction (reaction 2.3) represents that SMR is volume expensive, so low pressure is more preferable. In figure 2.1 Liu (2006) shows his simulation resulting thermodynamic equilibrium of each component as function of temperature only. SMR did not occur at temperature less than 200°C. Between 200 and 400°C, conversions of $CH_4$ and $H_2O$ increased slowly with temperature as well as amount of $H_2$ and $CO_2$ but CO did not exist in this temperature range, it meant WGS reaction is completely forward. When temperature was raised than 400°C, reforming reactions were rapidly more activated. Until up to 800°C, both $CH_4$ and $H_2O$ reached their maximum conversions and $H_2$ was highest produced. However, WGS activity declined rapidly with temperature in 400-800°C according to rising of CO. WSG deactivated because much higher concentration of $H_2$ made WSG turn in backward direction although normally WGS equilibrium is more forward when temperature increases. Lastly, the amount of each component was steady above 800°C. Due to different favorable temperature range between reforming reactions and WGS reaction, thus conventional hydrogen synthesis via SMR process consists of 2 stages of operation; the primary is reforming stage and the secondary is shifting stage (Liu, 2006).

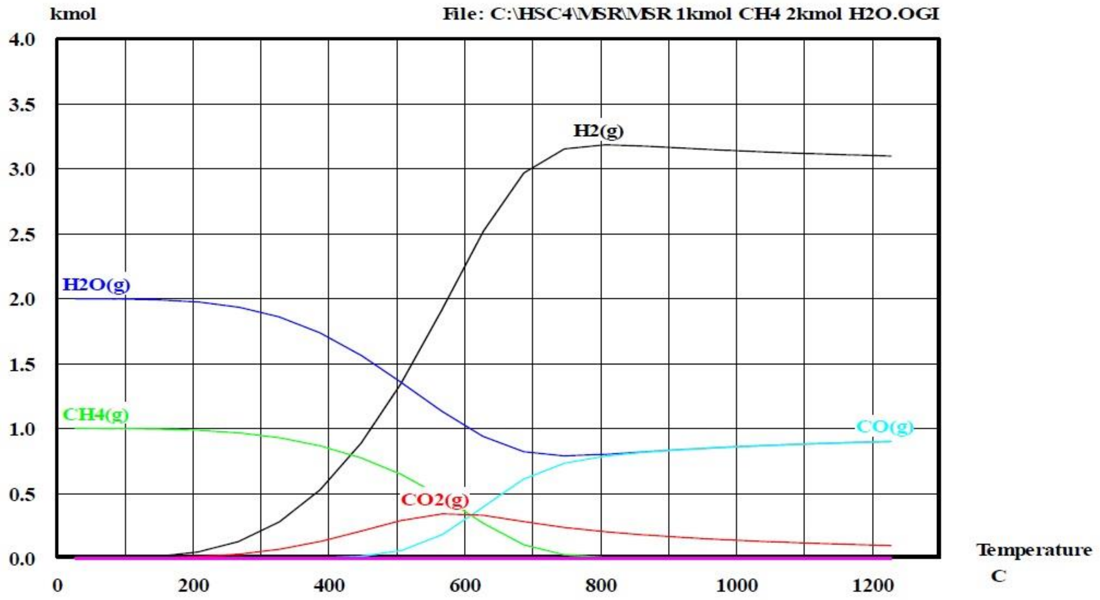

**Figure 2.1** Thermodynamic equilibrium simulation of SMR reactions with S/C = 2.

**Source:** Liu (2006)

The reforming stage operates above 800°C typically over a Ni-based catalyst. According to figure 2.2, Joensen and Rostrup-Nielsen (2002) show equilibrium conversion of $CH_4$ affected by temperature, pressure and S/C. In accordance with highly endothermic, volume expansive and reversible reactions of SMR, it is preferred to operate at high temperature (over 800°C), lowest pressure and higher-than-stoichiometric S/C (more than 2) to maximize the conversion. However, in practice, pressure occurred in reformer was typically 30-40 bar at 800-1,000°C (Liu, 2006) (but another process operated moderately 14–20 atm in this temperature range (Barelli *et al.*, 2008)) over a supported Ni catalyst.

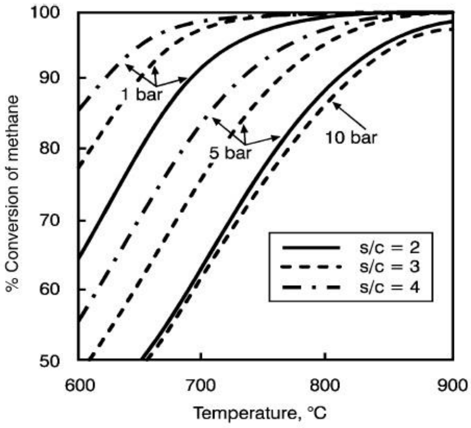

**Figure 2.2** Effect of temperature, pressure and S/C on equilibrium $CH_4$ conversion in SMR.

**Source:** Joensen and Rostrup-Nielsen (2002)

Although higher S/C would make $CH_4$ conversion better continually, but in practice S/C of 3 is typically sufficient to obtain maximum conversion. In other hand, if there is insufficient steam, undesired coke (C) formation of methane (reaction 2.5) or of carbon monoxide (reaction 2.6) might occur simultaneously (Liu, 2006).

$$CH_4 \longrightarrow C + 2H_2 \qquad \Delta H^{\circ}_{298} = +75 \text{ kJ/mol} \qquad (2.5)$$

$$2CO \rightleftharpoons C + CO_2 \qquad \Delta H^{\circ}_{298} = -173 \text{ kJ/mol} \qquad (2.6)$$

In shifting stage, although the kinetics of the catalytic WGS reaction are more favorable at higher temperature. But WGS reaction is moderately exothermic thus it is thermodynamically unfavorable at extremely high temperature as in reforming stage. To maintain high shifting rates and get higher conversion with this thermodynamic limitation, WGS is preferably divided into multiple adiabatic sub-stages with inter-cooling. WGS typically contains firstly high temperature shift (HTS) in temperature range of 350°C to 600°C with Fe-based catalysts and then low temperature shift (LTS) in temperature range of 150°C to 300°C with Cu-based catalysts (Callaghan, 2006).

### 2.1.2 Conventional processes of SMR

In conventional industry, hydrogen have been produced from natural gas via SMR processes through three separate sections i.e. reforming of methane, gas shifting and gas separation as figure 2.3. Due to thermodynamic equilibrium, a high temperature above 750°C is sufficient to maximize conversion of $CH_4$ and operated in a reforming furnace with fuel consumption. The effluent gas of the furnace, which still contains CO about 8–10% in dry basis, is fed forward to WGS reactors including HTS reactor which operated in 300–400°C then LTS reactor which operated in 200–300°C, in series. Then outlet gas from the second shift reactor, which mostly consists of $H_2$ and $CO_2$ (approximately $H_2$ 76%, $CO_2$ 17%, unreformed $CH_4$ 4% and CO 3% dry basis (Harrison, 2008)), will be sent into additional separation units, normally using either pressure swing adsorption (PSA) or amine scrubbing technology (Barelli *et al.*, 2008; Kenarsari *et al.*, 2013).

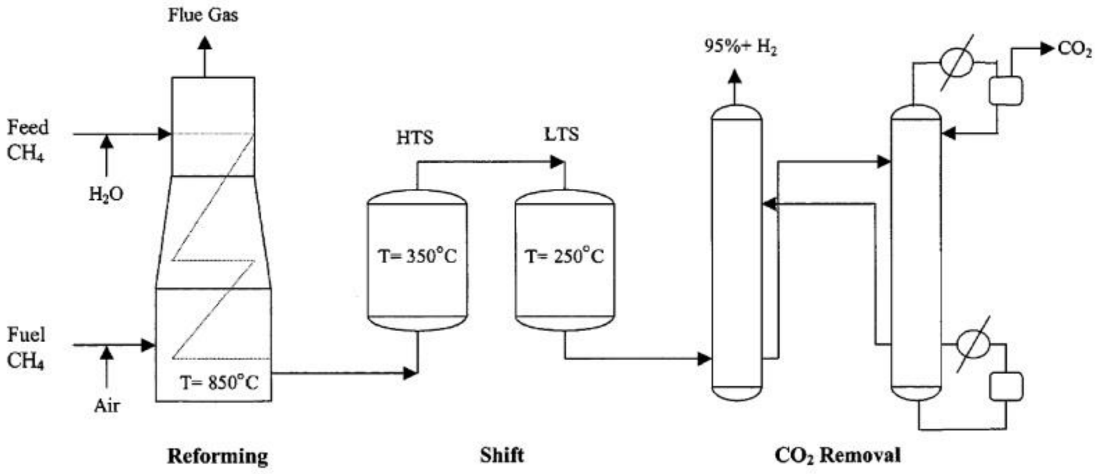

**Figure 2.3** Conventional SMR process removing $CO_2$ by PSA.

**Source:** Barelli *et al*. (2008)

### 2.1.3 Steam reforming of ethanol (SRE)

Ethanol (EtOH) is another excellent feed stock for hydrogen production via steam reforming process. Ethanol is renewable organic compound derived from fermentation of biomasses. The reforming pathways of ethanol are dependent on catalyst e.g. Ni-, Pt-, Pd- or Co-based catalysts, and their operation conditions (Vaidya and Rodrigues, 2006; Wu *et al.*, 2012; Ebiad *et al.*, 2012; Contreras *et al.*, 2014; Rautio *et al.*, 2015; Liu *et al.*, 2015; Zhao *et al.*, 2016) as shown in figure 2.4. By Ni-based catalysts used as same as SMR, the pathways are that EtOH is converted to acetaldehyde ($CH_3CHO$) and $CH_3CHO$ is converted to $CH_4$ then next to SMR on the same catalyst (Contreras *et al.*, 2014).

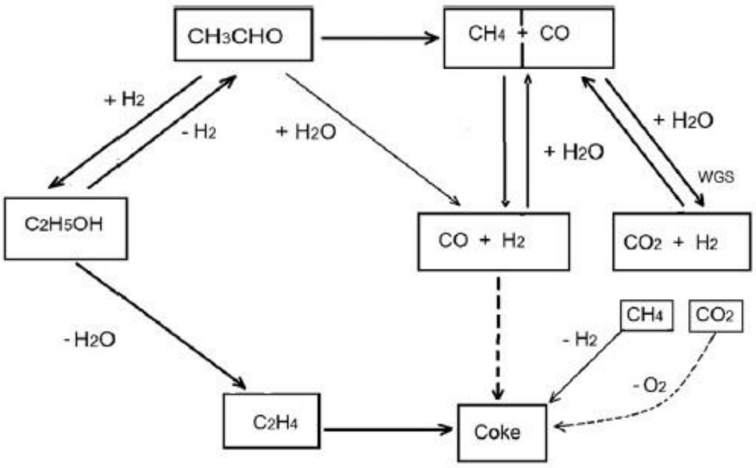

**Figure 2.4** Reaction pathways of steam reforming of ethanol.

**Source:** Contreras *et al*. (2014)

The reactions of EtOH to $CH_3CHO$ and $CH_3CHO$ to $CH_4$ are called *"Ethanol dehydrogenation reaction (ETD)"* and *"Acetaldehyde decomposition reaction (ACD)"* as reactions 2.7-2.8, respectively (Cunha *et al.*, 2012; Wu *et al.*, 2013; Wu *et al.*, 2014; Wu *et al.*, 2014; Wu *et al.*, 2014).

$$C_2H_5OH \rightleftharpoons CH_3CHO + H_2 \qquad \Delta H^{\circ}_{298} = +68.4 \text{ kJ/mol} \qquad (2.7)$$

$$CH_3CHO \rightleftharpoons CH_4 + CO \qquad \Delta H^{\circ}_{298} = -18.8 \text{ kJ/mol} \qquad (2.8)$$

In practice, acetaldehyde is unstable intermediate and quite totally converted to methane. Thus ethanol reforming with excess steam get EtOH conversion reach 100% according to a review of Haryanto *et al.* (2005) as table 2.1. Therefore De-Souza *et al.* (2013) can combined ETD with ACD into *"Ethanol decomposition reaction (EDC)"* that EtOH directly is converted to $CH_4$, CO and $H_2$ as reaction 2.9.

$$C_2H_5OH \rightarrow CH_4 + CO + H_2 \qquad \Delta H^{\circ}_{298} = +49.6 \text{ kJ/mol} \qquad (2.9)$$

Furthermore, steam could react directly with EtOH in another pathway which also get $CH_4$ similarly to EDC reaction. Here, this reaction will be called ethanol decomposition with steam (EDC/S) as reaction 2.10 (Vaidya and Rodrigues, 2006).

$$C_2H_5OH + H2O \rightarrow CH_4 + CO_2 + 2H_2 \qquad \Delta H^{\circ}_{298} = +8.4 \text{ kJ/mol} \qquad (2.10)$$

**Table 2.1** Suitable catalysts of ethanol steam reforming and their performances.

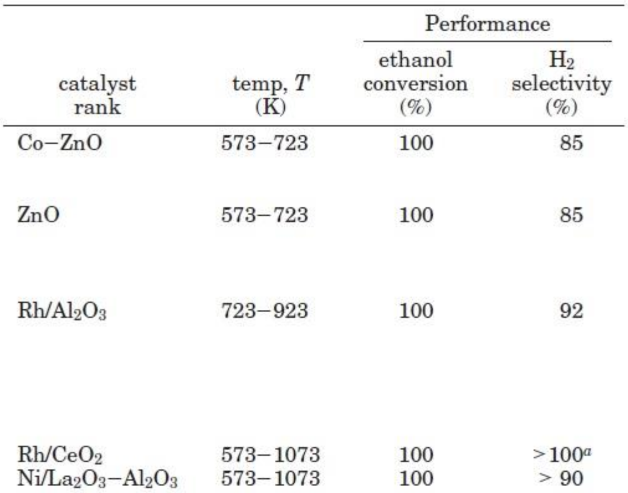

| | | Performance | |
|---|---|---|---|
| catalyst rank | temp, $T$ (K) | ethanol conversion (%) | $H_2$ selectivity (%) |
| Co–ZnO | 573–723 | 100 | 85 |
| ZnO | 573–723 | 100 | 85 |
| $Rh/Al_2O_3$ | 723–923 | 100 | 92 |
| $Rh/CeO_2$ | 573–1073 | 100 | $>100^a$ |
| $Ni/La_2O_3–Al_2O_3$ | 573–1073 | 100 | > 90 |

**Source:** Haryanto *et al*. (2005)

After ethanol is quite all converted to methane, methane will be reformed with steam via SMR as previous described reactions 2.2-2.4. Therefore the *"Overall reaction of SRE"* can be summarized as below.

$$C_2H_5OH + 3H_2O \rightleftharpoons 2CO_2 + 6H_2 \qquad \Delta H^{\circ}_{298} = +173.4 \text{ kJ/mol} \qquad (2.11)$$

The overall reforming reaction of ethanol is strongly endothermic as well the overall reforming reaction of methane.

## 2.2 Steam reforming with $CO_2$ sorption enhancement

When integrate sorbents in the reformers, produced $CO_2$ from reforming in reactions 2.3 and 2.11 has adsorbed then the equilibrium of the reforming reactions is shifted forward. Advantages of this sorption enhancement include that 1) higher conversion 2) $CO_2$ is separated from effluent gas 3) lower operation temperature due to exothermic adsorption and shifting of reforming reactions (Rodrigues *et al.*, 2017). For methane and ethanol, the reforming reaction with $CO_2$ sorption is called *"Sorption enhanced steam methane reforming reaction (SESMR)"* and *"Sorption enhanced steam reforming of ethanol reaction (SESRE)"*, respectively. The details are discussed in subtopics below.

### 2.2.1 $CO_2$ adsorption and desorption

There are many sorbents usable for $CO_2$ capture as shown in table 2.2. The suitable sorbents to capture $CO_2$ from reforming reactions should have excellent properties as follows:

1) High $CO_2$ capacity.

2) High stability after many cycles of re-usage.

3) High adsorption kinetics in the range of temperature 450–650°C.

4) Low temperature interval between adsorption and desorption.

And other properties such as high selectivity, good mechanical strength and low cost might be considered (Barelli *et al.*, 2008; Singh *et al.*, 2009).

**Table 2.2** Suitable sorbents for $CO_2$ capture and their performances.

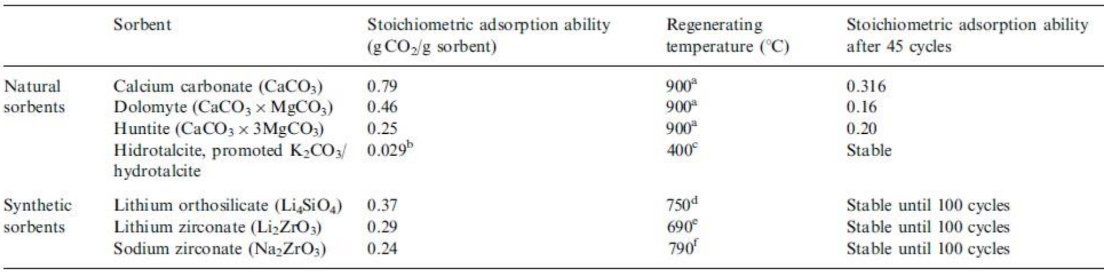

| | Sorbent | Stoichiometric adsorption ability ($gCO_2/g$ sorbent) | Regenerating temperature (°C) | Stoichiometric adsorption ability after 45 cycles |
|---|---|---|---|---|
| Natural sorbents | Calcium carbonate ($CaCO_3$) | 0.79 | 900[a] | 0.316 |
| | Dolomyte ($CaCO_3 \times MgCO_3$) | 0.46 | 900[a] | 0.16 |
| | Huntite ($CaCO_3 \times 3MgCO_3$) | 0.25 | 900[a] | 0.20 |
| | Hidrotalcite, promoted $K_2CO_3$/hydrotalcite | 0.029[b] | 400[c] | Stable |
| Synthetic sorbents | Lithium orthosilicate ($Li_4SiO_4$) | 0.37 | 750[d] | Stable until 100 cycles |
| | Lithium zirconate ($Li_2ZrO_3$) | 0.29 | 690[e] | Stable until 100 cycles |
| | Sodium zirconate ($Na_2ZrO_3$) | 0.24 | 790[f] | Stable until 100 cycles |

**Source:** Barelli *et al.* (2008)

Among all listed sorbents, CaO sorbents are the cheapest and have the highest $CO_2$ capacity, moderate adsorption rate but the lowest stability (Barelli *et al.*, 2008; Harrison, 2008; Sayyah *et al.*, 2013; Islam *et al.*, 2014; Ping and Wu, 2015). Hydrotalcite-like materials (HTCls) have the highest adsorption rate, good stability but very low $CO_2$ capacity (Koumpouras *et al.*, 2007; Barelli *et al.*, 2008; Harrison, 2008). Synthetic sorbents have high capacity, good stability and low to moderate adsorption rate but are the most expansive (Ochoa-Fernandez *et al.*, 2005; Koumpouras *et al.*, 2007; Barelli *et al.*, 2008; Harrison, 2008). Thus, for large-scale hydrogen production via SESMR, natural CaO sorbents are preferable due to their costs.

Reaction of CaO sorbents adsorbing $CO_2$ is as reaction 2.12 which forwardly called *“carbonation reaction”* and backwardly is called *“decarbonation reaction”*.

$$CaO + CO_2 \rightleftharpoons CaCO_3 \qquad \Delta H^{\circ}_{298} = -178 \text{ kJ/mol} \qquad (2.12)$$

Kinetics of carbonation and decarbonation depend on partial pressure of $CO_2$ and temperature of operation. The temperature effects to equilibrium pressure of $CO_2$ as shown in figure 2.5. When partial pressure of $CO_2$ is higher than the equilibrium pressure, $CO_2$ is adsorbed (carbonation occurs). Otherwise when partial pressure of $CO_2$ is lower, $CO_2$ is desorbed (decarbonation occurs). In case that partial pressure of $CO_2$ equals to atmosphere, the temperature must be much less than about 900°C (equilibrium temperature) to adsorb $CO_2$. After CaO adsorbs $CO_2$ and becomes $CaCO_3$, they can be refreshed by increasing the temperature to much more the equilibrium temperature.

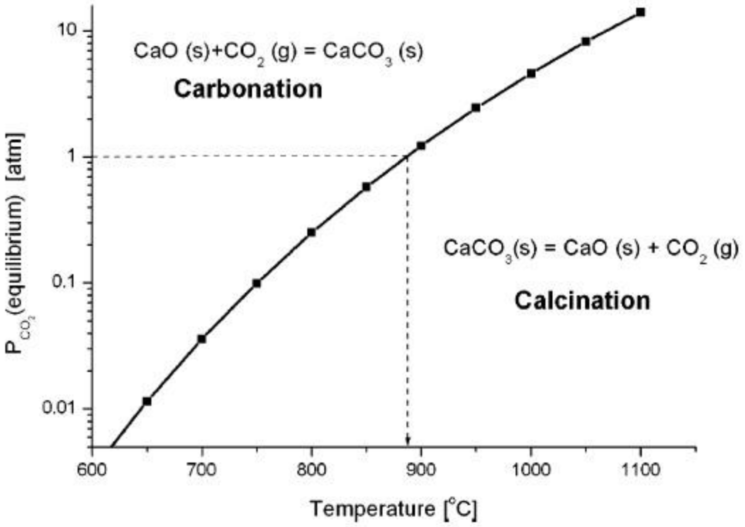

**Figure 2.5** Equilibrium pressure of $CO_2$ as a function of temperature.

**Source:** Johnsen *et al*. (2006)

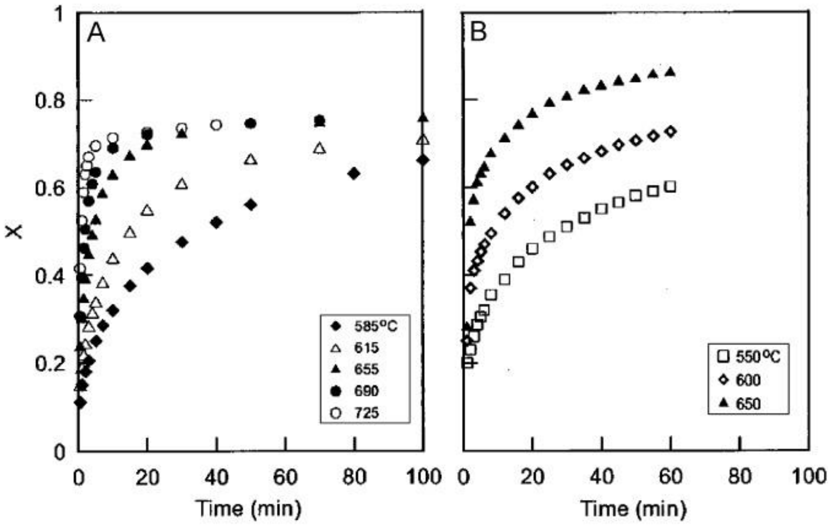

**Figure 2.6** Carbonation fraction (X) of CaO derived from experiments of Bathia and Pelmutter (left) and Gupta and Fan (right).

**Source:** cited in Barelli *et al.* (2008)

From figure 2.6 left is experimental results studied by Bhatia and Perlmutter (cited in Barelli *et al.*, 2008) and right relates to the experimental study of Gupta and Fan (cited in Barelli *et al.*, 2008). This has been reported that the carbonation does not proceed to the complete conversion of CaO but the maximum conversion is in the range of 70–80% or up to 90%. However, if spent CaO is reused by numbers of cycling, the maximum conversion or $CO_2$ capacity will be decreased as shown in figure 2.7. This is thermal deactivation which CaO sorbents have higher deactivation rate than other sorbents. $CO_2$ capacity of CaO will drop until steady to about 28% (Johnsen *et al.*, 2006).

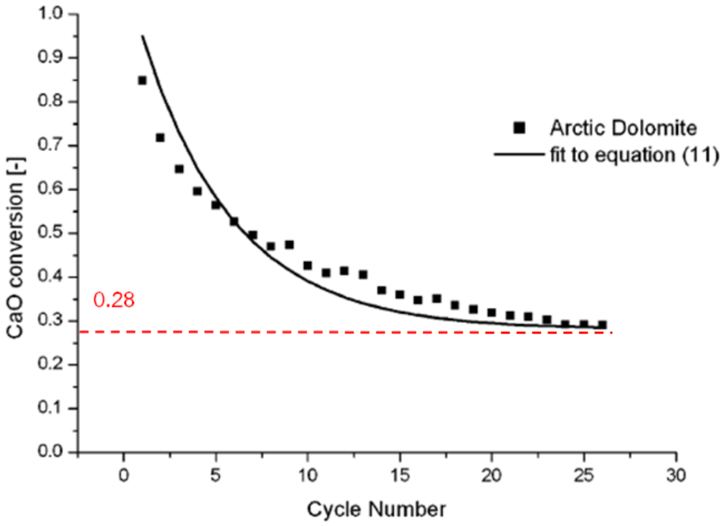

**Figure 2.7** Deactivation of dolomite after numbers of using time.

**Source:** Johnsen *et al*. (2006)

### 2.2.2 Sorption enhanced steam reforming

From figure 2.8 in the conventional SMR process (without CaO) the $H_2$ concentration increases at the temperature increment and reaches a maximum of 0.77 at 800°C but in the SESMR the maximum is reached at 580°C with a value of $H_2$ molar fraction of 0.98. Relative to the SESMR process, when the temperature is less than 580°C the equilibrium $H_2$ content curve shows two branches i.e. the lower one allows for the formation of both $CaCO_3$ and $Ca(OH)_2$ but $Ca(OH)_2$ is not formed in the upper branch. Molar fraction of $H_2$ is evidently higher for SESMR than SMR in range of 580-820°C. When temperature is over 820°C, the molar fraction of $H_2$ becomes the same for the two cases because carbonation turns to decarbonation instead (Barelli *et al.*, 2008).

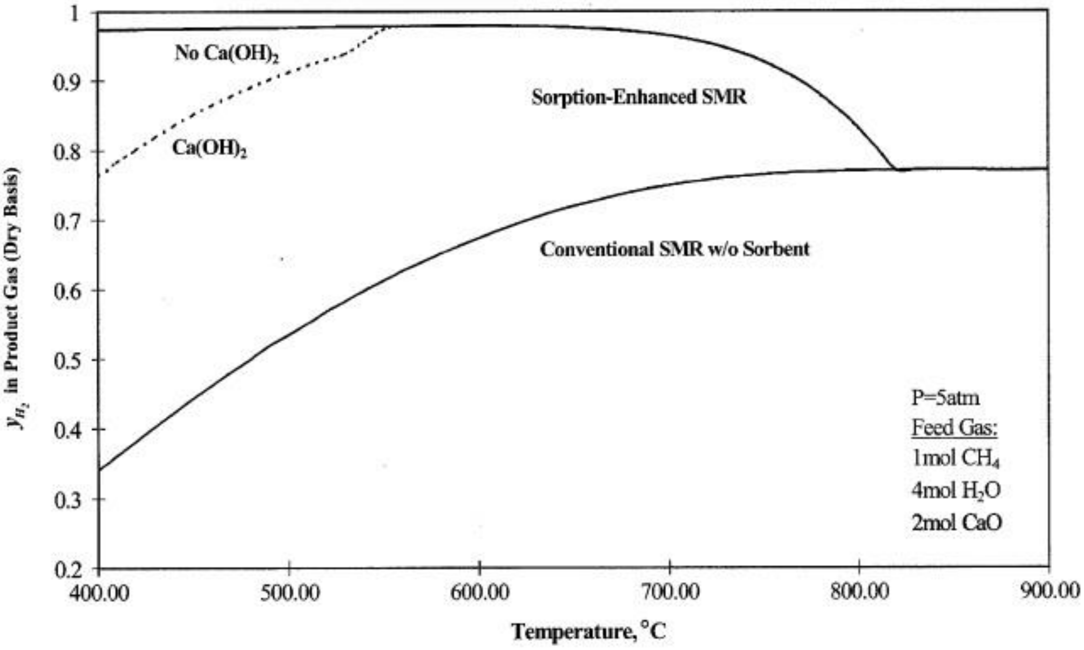

**Figure 2.8** SESMR process (using CaO sorbent) compared to conventional SMR process in which equilibrium $H_2$ dry molar fraction in product gas as a function of temperature at pressure = 5 atm and S/C = 4.

**Source:** Barelli *et al*. (2008)

The influence of operation pressure on range of SESMR temperature and equilibrium $H_2$ molar fraction is also shown in figure 2.9. When pressure is higher, maximum $H_2$ purity is little decreased but range of SESMR temperature is shifted to much higher. The shifting is not suitable because temperature of sorbent regeneration must also be shift and wasting energy. Thus SESMR with CaO sorbents prefers operation at atmosphere and temperature of 450-600°C (Barelli *et al.*, 2008).

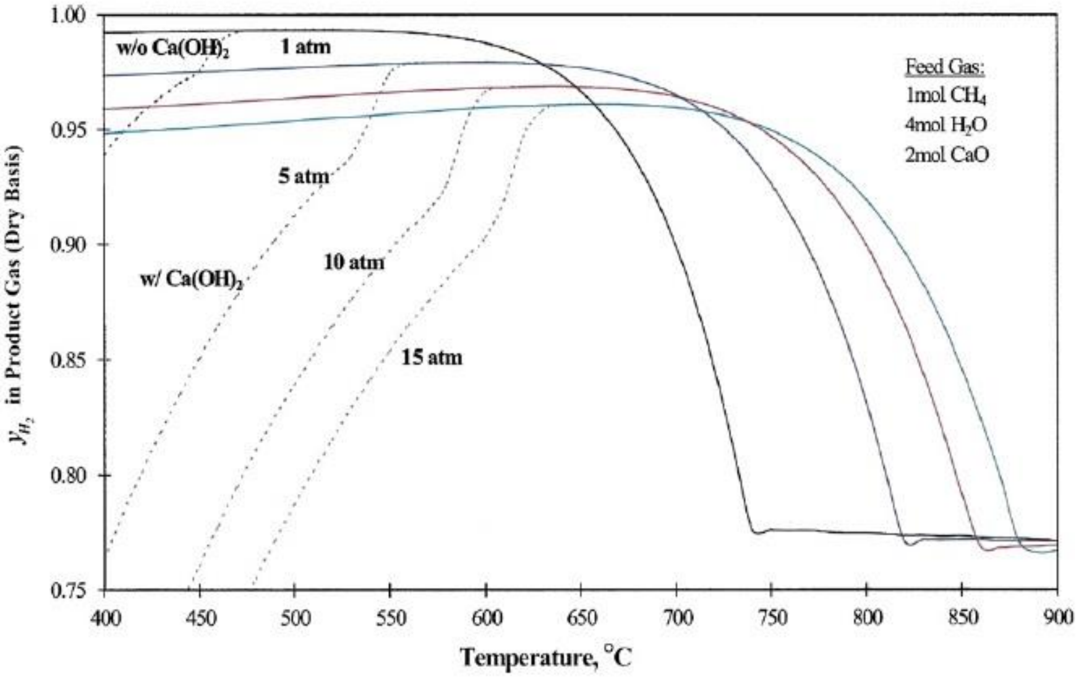

**Figure 2.9** Effect of pressure in SESMR process (using CaO sorbents) on equilibrium $H_2$ dry molar fraction in product gas as a function of temperature at S/C = 4.

**Source:** Barelli *et al*. (2008)

## 2.3 Fluidized bed reactors

Fluidized bed reactors are widely applied in processes containing gas and solids. Advantages of fluidized bed reactors over fixed bed reactors are lower pressure drop and more gas-solid (reactant-catalyst/sorbents) contacting throughout beds that give better mass and heat transfer. Types of gas-solid fluidized bed reactor are divided by gas-solid phenomena also called flow regimes as shown in figure 2.10. The typical regimes are bubbling bed, turbulent bed, fast fluidized and dilute transport regimes. The flow regimes depend on gas velocity, amount and properties of the solids (Kunii and Levenspiel, 1997).

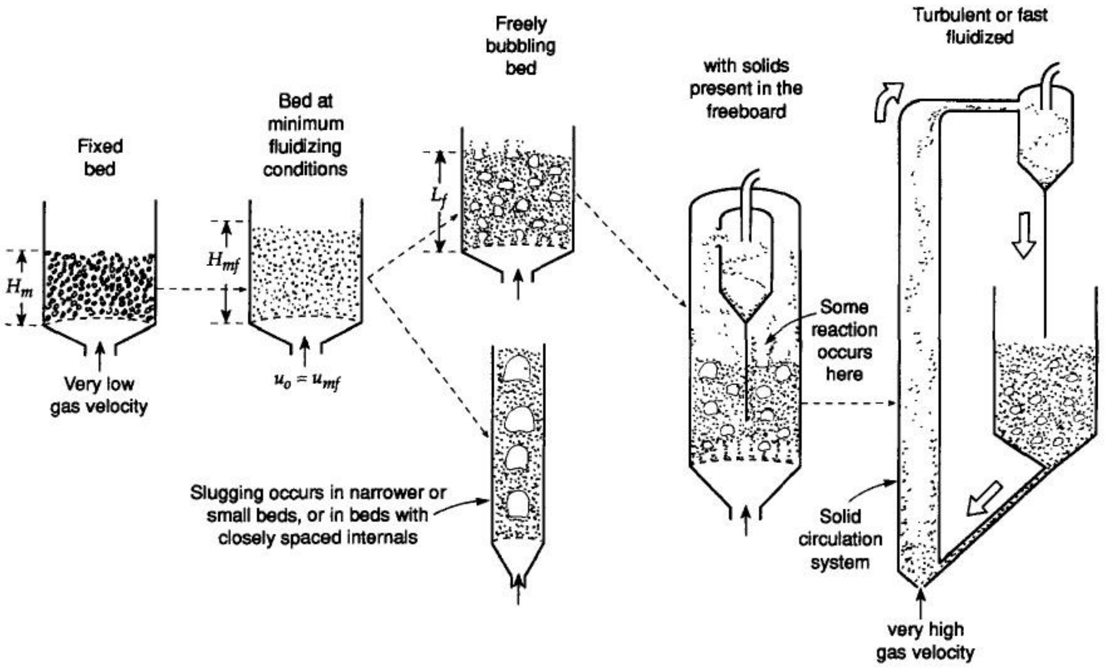

**Figure 2.10** Regimes of gas-solid fluidization.

**Source:** Kunii and Levenspiel (1997)

For gas-solid of both catalytic and non-catalytic reactions, fluidized bed reactors and their types have been applied in many conventional processes as shown in table 2.3. Circulating fluidized bed reactors (CFBR) have been utilized in commercial processes such as combustion boiler, fluidized bed catalytic cracking (FCC), Fischer-Tropsch synthesis, etc. For SESR application, CFBR has been developing and expected for large hydrogen production because feed increase with higher gas velocity and sorbents can be transported out of the reformer and regenerated simultaneously in another reactor (Kunii and Levenspiel, 1991). Other advantages of CFBR over Bubbling bed reactors and fixed bed reactors are shown in table 2.4 (Mousa *et al.*, 2014). A general CFBR system consists of four unit parts (Prajongkan, 2011) as follows:

**1) Riser**: Gas and solids come in at bottom. Solid particles are blown up and removed off with gas at top.

**2) Cyclone**: Solid particles are separated from gas and fall out at bottom.

**3) Downer**: Solids from cyclone fall in and move out at bottom. This unit could act like a receiver or another reactor.

**4) Solid return system**:  Solids return to bottom of the riser.

**Table 2.3** Industrial processes and applications of fluidization and their regime.

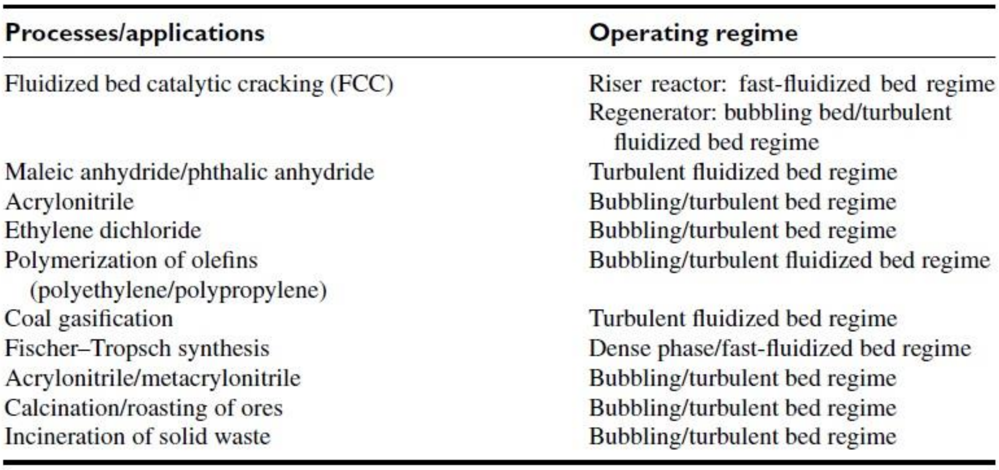

| Processes/applications | Operating regime |
|---|---|
| Fluidized bed catalytic cracking (FCC) | Riser reactor: fast-fluidized bed regime<br>Regenerator: bubbling bed/turbulent fluidized bed regime |
| Maleic anhydride/phthalic anhydride | Turbulent fluidized bed regime |
| Acrylonitrile | Bubbling/turbulent bed regime |
| Ethylene dichloride | Bubbling/turbulent bed regime |
| Polymerization of olefins (polyethylene/polypropylene) | Bubbling/turbulent fluidized bed regime |
| Coal gasification | Turbulent fluidized bed regime |
| Fischer–Tropsch synthesis | Dense phase/fast-fluidized bed regime |
| Acrylonitrile/metacrylonitrile | Bubbling/turbulent bed regime |
| Calcination/roasting of ores | Bubbling/turbulent bed regime |
| Incineration of solid waste | Bubbling/turbulent bed regime |

**Source:** Ranade (2002)

**Table 2.4** Comparison between fixed bed, bubbling fluidized bed and circulating fluidized bed reactors applied for steam reformer.

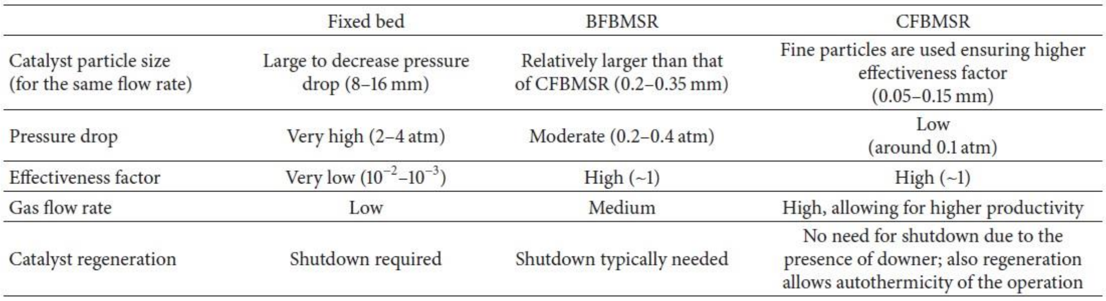

| | Fixed bed | BFBMSR | CFBMSR |
|---|---|---|---|
| Catalyst particle size (for the same flow rate) | Large to decrease pressure drop (8–16 mm) | Relatively larger than that of CFBMSR (0.2–0.35 mm) | Fine particles are used ensuring higher effectiveness factor (0.05–0.15 mm) |
| Pressure drop | Very high (2–4 atm) | Moderate (0.2–0.4 atm) | Low (around 0.1 atm) |
| Effectiveness factor | Very low ($10^{-2}$–$10^{-3}$) | High (~1) | High (~1) |
| Gas flow rate | Low | Medium | High, allowing for higher productivity |
| Catalyst regeneration | Shutdown required | Shutdown typically needed | No need for shutdown due to the presence of downer; also regeneration allows autothermicity of the operation |

**Source:** Mousa *et al.* (2014)

## 2.4 Kinetic modeling

Kinetic rates involved in SESMR and SESRE, had been studied and expressed from several different researches. But in literature review, the following kinetic rates of SMR, SRE, carbonation and decarbonation were chosen and applied with successful validations in many previous researches. The SMR kinetics from Xu and Froment (1989) and the carbonation kinetics from Sun *et al.* (2008) had been validated in fluidization with good results (Lindborg *et al.*, 2007) then were continuously applied in almost publications of the research group from NTNU (Wang *et al.*, 2010; Wang *et al.*, 2010; Wang *et al.*, 2011; Chao *et al.*, 2012; Sánchez *et al.*, 2012; Sánchez and Jakobsen, 2012; Solsvik *et al.*, 2012; Sánchez *et al.*, 2013; Solsvik *et al.*, 2013; Wang *et al.*, 2014; Solsvik *et al.*, 2014). In addition, this SMR kinetics was also validated in other studies with very good results, such as percentage of $H_2$ in effluent gas had deviation less than 0.5% in a work of Di Carlo *et al.* (2010) as well as deviation about 3.5% for SMR and 1% for SESMR in a work of Chen *et al.* (2013). This might prove that both kinetics were suitable for the future studies of fluidization with SESMR using the Ni-based catalyst and the dolomite. Several kinetic models of SRE on Ni-based catalyst were applied by some researches (Mas *et al.*, 2008; Wu *et al.*, 2013; De-Souza *et al.*, 2013; Wu *et al.*, 2014; Wu *et al.*, 2014; Wu *et al.*, 2014) but unfortunately, there was no application with fluidization. The only kinetics of SRE which applied on typical Ni-based catalyst like Ni-$Al_2O_3$ (Mas *et al.*, 2008; De-Souza *et al.*, 2013) would be studied as described next.

### 2.4.1 Kinetics of SMR

Xu and Froment (1989) investigated the intrinsic kinetics which account for the resistance to diffusion on a Ni/MgAl$_2$O$_4$ catalyst. The kinetic rates expressing reactions 2.2-2.4 are as eqs. 2.13-2.15, respectively.

$$r_{bSMR}=\frac{k_{bSMR}}{p_{H_2}^{2.5}}\left(p_{CH_4}p_{H_2O}-\frac{p_{H_2}^{3}p_{CO}}{K_{bSMR}}\right)\cdot\frac{1}{DEN^2} \tag{2.13}$$

$$r_{gSMR}=\frac{k_{gSMR}}{p_{H_2}^{3.5}}\left(p_{CH_4}p_{H_2O}^{2}-\frac{p_{H_2}^{4}p_{CO_2}}{K_{gSMR}}\right)\cdot\frac{1}{DEN^2} \tag{2.14}$$

$$r_{WGS}=\frac{k_{WGS}}{p_{H_2}}\left(p_{CO}p_{H_2O}-\frac{p_{H_2}p_{CO_2}}{K_{WGS}}\right)\cdot\frac{1}{DEN^2} \tag{2.15}$$

$$DEN=1+K_{CO}P_{CO}+K_{H_2}P_{H_2}+K_{CH_4}P_{CH_4}+\frac{K_{H_2O}P_{H_2O}}{P_{H_2}} \tag{2.16}$$

Where

$r_i$ = Rates of reaction i, [kmol·kg$_{cat}^{-1}$·s$^{-1}$]

$p_k$ = Partial pressures of species k, [Pa]

$k_i$ = Rate constants of reaction i according to Xu and Froment (1989) are as follows:

$$k_{bSMR}=9.708\cdot10^{-4}\exp\left[\frac{-240100}{R}\left(\frac{1}{T}-\frac{1}{648}\right)\right] \quad ,\ [\text{kmol}\cdot\text{Pa}^{0.5}\cdot\text{kg}_{cat}^{-1}\cdot\text{s}^{-1}] \tag{2.17}$$

$$k_{gSMR}=1.156\cdot10^{-4}\exp\left[\frac{-243900}{R}\left(\frac{1}{T}-\frac{1}{648}\right)\right] \quad ,\ [\text{kmol}\cdot\text{Pa}^{0.5}\cdot\text{kg}_{cat}^{-1}\cdot\text{s}^{-1}] \tag{2.18}$$

$$k_{WGS}=1.2597\cdot10^{-6}\exp\left[\frac{-67130}{R}\left(\frac{1}{T}-\frac{1}{648}\right)\right] \quad ,\ [\text{kmol}\cdot\text{kg}_{cat}^{-1}\cdot\text{Pa}^{-1}\cdot\text{s}^{-1}] \tag{2.19}$$

$K_i$ = Equilibrium constants of reaction i according to Xiu *et al.* (2002) are as follows:

$$K_{bSMR}=\frac{101325^2}{\exp(0.2513Z^4-0.3665Z^3-0.58101Z^2+27.1337Z-3.277)} \quad ,\ [\text{Pa}^2] \tag{2.20}$$

$$K_{gSMR}=K_{bSMR}K_{WGS} \quad ,\ [\text{Pa}^2] \tag{2.21}$$

$$K_{WGS}=\exp(-0.29353Z^3+0.63508Z^2+4.1778Z+0.31688) \quad ,\ [-] \tag{2.22}$$

$$Z=\frac{1000}{T}-1 \quad ,\ [-] \tag{2.23}$$

$K_k$ = Adsorption equilibrium constants of species k according to Xu and Froment (1989) are as follows:

$$K_{CH_4} = 1.791 \cdot 10^{-6} \exp\left[\frac{38280}{R}\left(\frac{1}{T} - \frac{1}{823}\right)\right] \quad , [Pa^{-1}] \quad (2.24)$$

$$K_{H_2O} = 0.4152 \exp\left[\frac{-88680}{R}\left(\frac{1}{T} - \frac{1}{823}\right)\right] \quad , [-] \quad (2.25)$$

$$K_{CO} = 4.091 \cdot 10^{-4} \exp\left[\frac{70650}{R}\left(\frac{1}{T} - \frac{1}{648}\right)\right] \quad , [Pa^{-1}] \quad (2.26)$$

$$K_{H_2} = 2.960 \cdot 10^{-7} \exp\left[\frac{82900}{R}\left(\frac{1}{T} - \frac{1}{648}\right)\right] \quad , [Pa^{-1}] \quad (2.27)$$

### 2.4.2 Kinetics of SRE

From literature review, two approaches were found for kinetic models of SRE reactions on Ni-based catalyst. The first SRE kinetics was applied in a study of De-Souza *et al.* (2013). Another one was modelled from kinetic study of Mas *et al.* (2008).

**Model A**: De-Souza *et al.* (2013) studied simulations of SRE using favorite kinetic models of the SMR reactions (reactions 2.2-2.4) next to kinetic model of the EDC reaction (reaction 2.9). Thus, this SRE approach included four reactions as follows:

EDC: $C_2H_5OH \rightarrow CH_4 + CO + H_2$ (2.9)

bSMR: $CH_4 + H_2O \rightleftharpoons CO + 3H_2$ (2.2)

gSMR: $CH_4 + 2H_2O \rightleftharpoons CO_2 + 4H_2$ (2.3)

WGS: $CO + H_2O \rightleftharpoons O_2 + H_2$ (2.4)

The power law kinetic rate of EDC is irreversible first order which derived from Sun *et al.* (2005) as the following.

$$r_{EDC} = k_{EDC} p_{EtOH} \quad (2.28)$$

Where

$r_{EDC}$ = Rate of EDC reaction, $[kmol \cdot kg_{cat}^{-1} \cdot s^{-1}]$

$p_{EtOH}$ = Partial pressure of ethanol, [Pa]

$k_{EDC}$ = Rate constant of EDC reaction, [kmol·Pa$^{-1}$·kg$_{cat}^{-1}$·s$^{-1}$], is as the following.

$$k_{EDC} = \frac{4.55\cdot 10^{-5}}{T}\exp\left[\frac{-2030}{T}\right] \tag{2.29}$$

While the set of kinetic models for the SMR reactions belongs to Xu and Froment (1989) as in the previous section.

**Model B**: Mas *et al.* (2008) studied kinetics of SRE and derived their own kinetic model. Their model involved four reactions as following.

$$\text{EDC:} \quad C_2H_5OH \rightarrow CH_4 + CO + H_2 \tag{2.9}$$

$$\text{EDC/S:} \quad C_2H_5OH + H_2O \rightarrow CH_4 + CO_2 + 2H_2 \tag{2.10}$$

$$\text{bSMR:} \quad CH_4 + H_2O \rightleftharpoons CO + 3H_2 \tag{2.2}$$

$$\text{gSMR:} \quad CH_4 + 2H_2O \rightleftharpoons CO_2 + 4H_2 \tag{2.3}$$

The reaction rates of these SRE reactions were expressed as follows:

$$r_{EDC} = k_{EDC}K_{EtOH}p_{EtOH}\cdot\frac{1}{DEN} \tag{2.30}$$

$$r_{EDC/S} = k_{EDC/S}K_{EtOH}K_{H_2O}p_{EtOH}p_{H_2O}\cdot\frac{1}{DEN^2} \tag{2.31}$$

$$r_{bSMR} = k_{bSMR}K_{CH_4}K_{H_2O}\left(p_{CH_4}p_{H_2O}-\frac{p_{H_2}^3p_{CO}}{K_{bSMR}}\right)\cdot\frac{1}{DEN^2} \tag{2.32}$$

$$r_{gSMR} = k_{gSMR}K_{CH_4}K_{H_2O}\left(K_{H_2O}p_{CH_4}p_{H_2O}^2-\frac{p_{H_2}^4p_{CO_2}}{K_{gSMR}}\right)\cdot\frac{1}{DEN^3} \tag{2.33}$$

$$DEN = 1+K_{EtOH}p_{EtOH}+K_{H_2O}p_{H_2O}+K_{CH_4}p_{CH_4} \tag{2.34}$$

Rate constants of reaction i were defined as follows:

$$k_{EDC} = 4.833\cdot 10^{-4}\exp\left[\frac{-278740}{R}\left(\frac{1}{T}-\frac{1}{873}\right)\right] \quad \text{, [kmol·kg}_{cat}^{-1}\text{·s}^{-1}] \tag{2.35}$$

$$k_{EDC/S} = 5.167\cdot 10^{-3}\exp\left[\frac{-235060}{R}\left(\frac{1}{T}-\frac{1}{873}\right)\right] \quad \text{, [kmol·kg}_{cat}^{-1}\text{·s}^{-1}] \tag{2.36}$$

$$k_{bSMR} = 1.667\cdot 10^{-3}\exp\left[\frac{-123500}{R}\left(\frac{1}{T}-\frac{1}{873}\right)\right] \quad \text{, [kmol·kg}_{cat}^{-1}\text{·s}^{-1}] \tag{2.37}$$

$$k_{gSMR} = 4.000 \cdot 10^{-3} \exp\left[\frac{-213900}{R}\left(\frac{1}{T} - \frac{1}{873}\right)\right] \quad , [\mathrm{kmol \cdot kg_{cat}^{-1} \cdot s^{-1}}] \quad (2.38)$$

And adsorption equilibrium constants of species k were expressed as follows:

$$K_{H_2O} = 3.691 \cdot 10^{-4} \exp\left[\frac{92400}{R}\left(\frac{1}{T} - \frac{1}{873}\right)\right] \quad , [\mathrm{Pa^{-1}}] \quad (2.39)$$

$$K_{EtOH} = 6.089 \cdot 10^{-4} \exp\left[\frac{199700}{R}\left(\frac{1}{T} - \frac{1}{873}\right)\right] \quad , [\mathrm{Pa^{-1}}] \quad (2.40)$$

$$K_{CH_4} = 1.120 \cdot 10^{-2} \exp\left[\frac{124700}{R}\left(\frac{1}{T} - \frac{1}{873}\right)\right] \quad , [\mathrm{Pa^{-1}}] \quad (2.41)$$

Lastly, equilibrium constants of reactions, $K_{bSMR}$ and $K_{gSMR}$ could be used eq. 2.20 and eq. 2.21, respectively.

### 2.4.3 Kinetics of carbonation

Sun *et al.* (2008) determined the rate constants of carbonation of calcined limestone and dolomite which both are natural CaO sorbents. The kinetics of carbonation by dolomite is expressed as the following.

$$r_{carb} = k_{carb}\left(p_{CO_2} - p_{CO_2,eq}\right)^n S_0 \left(1 - X_{CaO}\right) \quad (2.42)$$

Where

$r_{carb}$ = Rate of carbonation, [kmol·$\mathrm{kg_{sorb}^{-1} \cdot s^{-1}}$]

$p_{CO2}$ = Partial pressure of $CO_2$, [Pa]

$p_{CO2,eq}$ = Equilibrium pressures of $CO_2$, [Pa], are dependent on temperature ranges as follows:

- For $T >$ 1173.15 K according to Abanades *et al.* (2004);

$$p_{CO_2,eq} = 1.216 \cdot 10^{12} \exp\left[\frac{-19130}{T}\right] \quad (2.43)$$

- For $T \leq$ 1173.15 K according to Johnsen *et al.* (2006);

$$p_{CO_2,eq} = 4.1918 \cdot 10^{12} \exp\left[\frac{-20474}{T}\right] \quad (2.44)$$

$k_{carb}$ = Rate constants of carbonation and $n$ = Degree of partial pressure, [-], are dependent on $p_{CO2}$ ranges as follows:

- When $(p_{CO2}- p_{CO2,eq}) > 10{,}000$ Pa;

$$k_{carb} = 1.04\cdot10^{-6}\exp\left[\frac{-20400}{RT}\right] \qquad , [\mathrm{kmol\cdot m^{-2}\cdot s^{-1}}] \quad (2.45)$$

and $n = 0$

- When $0 < (p_{CO2}- p_{CO2,eq}) \leq 10{,}000$ Pa;

$$k_{carb} = 1.04\cdot10^{-10}\exp\left[\frac{-20400}{RT}\right] \qquad , [\mathrm{kmol\cdot m^{-2}\cdot Pa^{-1}\cdot s^{-1}}] \quad (2.46)$$

and $n = 1$

- When $(p_{CO2}-p_{CO2,eq}) \leq 0$ Pa;

There is no $CO_2$ captured (decarbonation occurs instead).

$S_0$ = Initial specific surface area of CaO = $3.1\times10^4$ $m^2\cdot kg_{sorb}^{-1}$ for dolomite

$X_{CaO}$ = Conversion of CaO, [-], which defined for dolomite as

$$X_{CaO} \equiv \frac{\langle n_{CaO}^{Sorbent}\rangle_{used}}{\langle n_{CaO}^{Sorbent}\rangle_{fresh}} = \frac{n_{CaCO3}^{Sorbent}}{n_{CaO,0}^{Sorbent}} = \frac{x_{CaCO3}^{Sorbent}}{x_{CaO,0}^{Sorbent}} = \frac{x_{CaCO3}^{Sorbent}}{0.5188} \quad (2.47)$$

### 2.4.4 Kinetics of decarbonation

Okunev *et al.* (2008) had analyzed kinetics of decarbonation of CaO sorbent (reverse of reaction 2.12) and found that the rate is dependent on particle size, temperature, $CO_2$ pressure and Sherwood number as the following.

$$r_{deca} = \frac{1}{M_{CO_2}} \frac{2.46\cdot10^4 S_{sp}\exp\left[\frac{-20474}{T}\right]}{\left[16\frac{d_p^2 S_{sp}\rho_p}{\varepsilon^2 Sh}\right]^{2/3} + \exp\left[7.8\left(\frac{p_{CO_2}}{p_{CO_2,eq}}\right)\right]} \left(1- \frac{p_{CO_2}}{p_{CO_2,eq}}\right) \quad (2.48)$$

Where

$r_{deca}$ = Rate of decarbonation, $[\mathrm{kmol\cdot kg_{sorb}^{-1}\cdot s^{-1}}]$

$M_{CO2}$ = Molecular weight of $CO_2$, $[\mathrm{kg\cdot kmol^{-1}}]$

$S_{sp}$ = Specific surface area of $CaCO_3$, $[\mathrm{m^2\cdot kg_{sorb}^{-1}}]$, is

$$S_{sp} = S_{sp,0}X_{CaO} = 380X_{CaO} \quad (2.49)$$

$X_{CaO}$ = Conversion of CaO, [-], which defined for dolomite as eq. (2.47)

$d_p$ = Mean diameter of particle, [m]

$\rho_p$ = Density of particle, [kg·m$^{-3}$]

$\varepsilon$ = Constant porosity of dolomite = 0.47 [-]

$p_{CO2}$ = Partial pressure of $CO_2$, [Pa]

$p_{CO2,eq}$ = Equilibrium pressure of $CO_2$, [Pa], is dependent on temperature ranges as eqs. 2.43-2.44.

$Sh$ = Sherwood number, [-], is a function of particle Reynolds number ($Re_p$) and Schmidt number ($Sc$) as follows:

$$Sh = 2+Re_p^{1/3}\cdot Sc^{1/3} \qquad (2.50)$$

$$Re_p = \frac{\rho_g U_{pg} d_p}{\mu_g} \qquad (2.51)$$

$$Sc = \frac{\mu_g}{\rho_g D^m_{CO_2}} \qquad (2.52)$$

$\mu_g$ = Viscosity of gas, [kg·m$^{-1}$·s$^{-1}$]

$\rho_g$ = Density of gas, [kg·m$^{-3}$]

$U_{pg}$ = Particle-gas relative velocity, [m·s$^{-1}$]

$D^m_{CO_2}$ = Molecular diffusion coefficient of $CO_2$ = 1.6x10$^{-4}$ [m$^2$·s$^{-1}$]

## 2.5 Computational fluid dynamics (CFD)

Computational fluid dynamics (CFD) is a modern branch of hydrodynamics using algorithms and numerical method i.e. discretization methods to solve complex fluid problems. CFD is an art of considering models of conservation combined with correlation equations (constitutive equations) and other involving models like chemical kinetic models, as shown in figure 2.11. In this case of fluidization which is gas-solid contacting transportation, multiphase flow models approach is siutable for utilization.

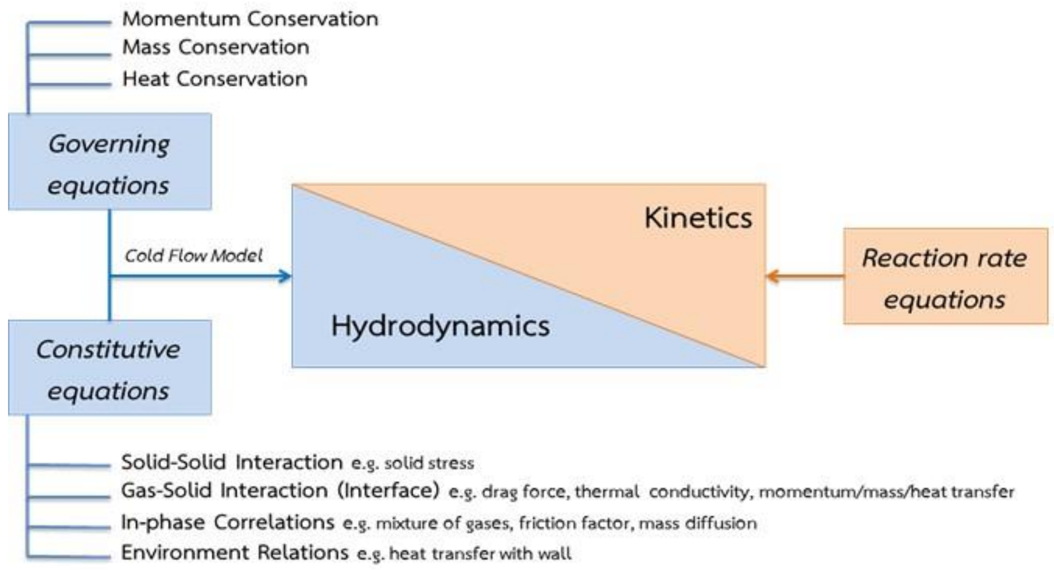

**Figure 2.11** Groups of models involving in CFD study.

### 2.5.1 Multiphase flow modeling

There are two main approaches for fluid-particle multiphase flow modeling (Ranade, 2002; Yeoh and Tu, 2010) as the following.

**1) Euler-Euler model** is also called granular flow model (GFM) in gas-solid flow system. An Eulerian framework is considered for all phases. The kinetic theory of granular flow (KTGF) that represents kinetic energy oscillation must be applied for any solid particle phase (Gidaspow, 1994). This Euler-Euler model with KTGF is suitable for this fluidization systems which have large amount of solid particles (Wang *et al.*, 2010; Di Carlo *et al.*, 2010; Wang *et al.*, 2010; Prajongkan, 2011; Wang *et al.*, 2011; Chao *et al.*, 2011; Chao *et al.*, 2012; Hodapp *et al.*, 2012; Sánchez *et al.*, 2012; Sánchez *et al.*, 2012; Solsvik *et al.*, 2012; Solsvik *et al.*, 2013; Solsvik *et al.*, 2014; Sánchez *et al.*, 2013; Wang *et al.*, 2014; Song *et al.*, 2016). The Euler-Euler model with KTGF is a principle of simulation in this dissertation described in next topic.

**2) Euler-Lagrange model** is also called discrete particle models (DPM) in gas-solid flow system. The Eulerian framework is considered for the continuum phase (gas phase) and a Lagrangian framework is considered for all the dispersed phases (solid phases).

### 2.5.2 Euler-Euler model with kinetic theory of granular flows (KTGF)

The concept of Euler-Euler approach (ANSYS, 2013) is that summary of volume fraction of each phase ($\varepsilon_q$) in each control volume is always unity.

$$\sum_{q=1}^{n} \varepsilon_q = 1 \tag{2.53}$$

The volume ($V_q$) and bulk density ($\rho_{bulk,q}$) of phase q are defined by

$$V_q = \int_V \varepsilon_q dV \tag{2.54}$$

$$\rho_{bulk,q} = \varepsilon_q \rho_q \tag{2.55}$$

where

$\rho_q$ = Physical density of phase q, [kg·m$^{-3}$]

The KTFG has extended from kinetic theory of gas by adding kinetic energy oscillation owing to inelastic collisions and fluctuating motions of the particles (ANSYS, 2013). A representative of the kinetic energy oscillation comes in terms of a granular temperature ($\Theta_s$) and can be evaluated from kinetic fluctuation energy conservation shown in eq. (2.86) later.

### 2.5.2.1 Governing equations

**1) Mass conservation**

The conservative equation of mass or called “continuity equation” can be expressed as the following (ANSYS, 2013).

$$\frac{\partial\rho}{\partial t}+\nabla\cdot(\rho\vec{v}) = S_m \tag{2.56}$$

For each phase q,

$$\frac{\partial}{\partial t}\left(\varepsilon_q\rho_q\right)+\nabla\cdot\left(\varepsilon_q\rho_q\vec{v}_q\right) = \sum_{p=1}^{n}\left(\dot{m}_{pq}-\dot{m}_{qp}\right)+S_{m,q} \tag{2.57}$$

where

$\vec{v}_q$ = Velocity of phase q, [m·s$^{-1}$]

$\dot{m}_{pq}$ = Mass transfer from phase p to phase q, [kg·m$^{-3}$·s$^{-1}$]

$S_{m,q}$ = Mass source of phase q, [kg·m$^{-3}$·s$^{-1}$]

**2) Momentum conservation**

The conservation equation of momentum can be written as the following (ANSYS, 2013).

$$\frac{\partial}{\partial t}(\rho\vec{v})+\nabla\cdot(\rho\vec{v}\vec{v}) = -\nabla p+\nabla\cdot\bar{\tau}+\rho\vec{g}+\vec{F} \tag{2.58}$$

Unlike mass conservation, interaction between solid phase and solid phase is difference from interaction between fluid phase and solid phase. Thus, for gas phase (g) the momentum conservation can be

$$\begin{aligned}\frac{\partial}{\partial t}\left(\varepsilon_g\rho_g\vec{v}_g\right)+\nabla\cdot\left(\varepsilon_g\rho_g\vec{v}_g\vec{v}_g\right) &= -\varepsilon_g\nabla p+\nabla\cdot\bar{\tau}_g+\varepsilon_g\rho_g\vec{g}\\ &\quad+\sum_{s=1}^{n}\left(K_{sg}\left(\vec{v}_s-\vec{v}_g\right)+\dot{m}_{sg}\vec{v}_{sg}-\dot{m}_{gs}\vec{v}_{gs}\right)\\ &\quad+\left(\vec{F}_g+\vec{F}_{lift,g}+\vec{F}_{wl,g}+\vec{F}_{vm,g}+\vec{F}_{td,g}\right)\end{aligned} \tag{2.59}$$

and the momentum conservation for solid phase (s) is

$$\begin{aligned}\frac{\partial}{\partial t}(\varepsilon_s\rho_s\vec{v}_s)+\nabla\cdot(\varepsilon_s\rho_s\vec{v}_s\vec{v}_s) &= -\varepsilon_s\nabla p-\nabla p_s+\nabla\cdot\bar{\tau}_s+\varepsilon_s\rho_s\vec{g} \\ &\quad +\textstyle\sum_{l=1}^{n}(K_{ls}(\vec{v}_l-\vec{v}_s)+\dot{m}_{ls}\vec{v}_{ls}-\dot{m}_{sl}\vec{v}_{sl}) \\ &\quad +\left(\vec{F}_s+\vec{F}_{lift,s}+\vec{F}_{vm,s}+\vec{F}_{td,s}\right) \qquad (2.60)\end{aligned}$$

where

$p$ = Static pressure, [Pa]

$p_s$ = Solid pressure, [Pa], described in eq. (2.83)

$\bar{\tau}_q$ = Stress tensor of phase q, [Pa], described in eq. (2.78)

$\vec{g}$ = Gravity force, [m·s$^{-2}$]

$\vec{v}_{sg}$ = Interphase velocity from solid phase to gas phase, [m·s$^{-1}$]

$\vec{v}_{ls}$ = Interphase velocity from phase l (could be either solid or gas) to solid phase, [m·s$^{-1}$]

$K_{sg} \equiv K_{gs}$ and $K_{ls} \equiv K_{sl}$ = Interphase momentum exchange coefficient, [kg·m$^{-3}$·s$^{-1}$], divided into gas-solid and solid-solid interphase as described in eqs. (2.89), (2.91) and (2.92)

$\vec{F}_q$ = External body force to phase q, [kg·m$^{-2}$·s$^{-2}$, N·m$^{-3}$]

$\vec{F}_{lift,q}$ = Lift force to phase q, [kg·m$^{-2}$·s$^{-2}$, N·m$^{-3}$]

$\vec{F}_{vm,q}$ = Virtual mass force to phase q, [kg·m$^{-2}$·s$^{-2}$, N·m$^{-3}$]

$\vec{F}_{td,q}$ = Turbulent dispersion force to phase q, [kg·m$^{-2}$·s$^{-2}$, N·m$^{-3}$]

$\vec{F}_{wl,g}$ = Wall lubrication force to only gas phase, [kg·m$^{-2}$·s$^{-2}$, N·m$^{-3}$]

### 3) Energy conservation

Analogous to velocities in momentum conservation, enthalpies take places in terms of mass flow in conservation of energy. For gas phase the equation of energy conservation can be written as the following (ANSYS, 2013).

$$\frac{\partial}{\partial t}\left(\varepsilon_g\rho_g H_g\right)+\nabla\cdot\left(\varepsilon_g\rho_g\vec{v}_g H_g\right)=\varepsilon_g\frac{\partial p_g}{\partial t}+\bar{\tau}_g:\nabla\vec{v}_g-\nabla\cdot\vec{q}_g$$
$$+S_{h,g}+\sum_{s=1}^{n}\left(Q_{sg}+\dot{m}_{sg}h_{sg}-\dot{m}_{gs}h_{gs}\right) \qquad (2.61)$$

Where

$H_g$ = Specific enthalpy of gas phase, [$m^2\cdot s^{-2}$, $J\cdot kg^{-1}$]

$p_g$ = Static pressure of gas phase, [Pa]

$\vec{q}_g$ = Heat flux of gas phase, [$W\cdot m^{-2}$]

$S_{h,g}$ = Heat source of gas phase, [$W\cdot m^{-3}$]

$Q_{sg}$ = Intensity of heat exchange between solid phase and gas phase, [$W\cdot m^{-3}$]

$h_{sg}\equiv h_{gs}$ = Interphase heat exchange coefficient between solid phase and gas phase, [$m^2\cdot s^{-2}$, $J\cdot kg^{-1}$], described in eq. (2.93)

For a solid phase, the energy conservation is derived with KTGF which also called the kinetic fluctuation energy conservation as the following (ANSYS, 2013).

$$\frac{3}{2}\left[\frac{\partial}{\partial t}\left(\varepsilon_s\rho_s\Theta_s\right)+\nabla\cdot\left(\varepsilon_s\rho_s\vec{v}_s\Theta_s\right)\right]=\left(-p_s\bar{I}+\bar{\tau}_s\right):\nabla\vec{v}_s+\nabla\cdot\left(k_{\Theta_s}\nabla\Theta_s\right)-\gamma_{\Theta_s}+\phi_{ls} \qquad (2.62)$$

Where

Term $\left(-p_s\bar{I}+\bar{\tau}_s\right):\nabla\vec{v}_s$ = Generation of energy by the solid stress tensor

Term $\nabla\cdot\left(k_{\Theta_s}\nabla\Theta_s\right)$ = Diffusion of energy

Term $\gamma_{\Theta_s}$ = Collisional dissipation of energy, defined by Lun *et al.* as eq. (2.63)

Term $\phi_{ls}$ = Kinetic energy exchange between phase l (could be either solid or gas) and solid phase, defined as eq. (2.64)

$\Theta_s$ = Granular temperature, [m$^{2}$·s$^{-2}$, J·kg$^{-1}$], described in eq. (2.86)

$\bar{\mathrm{I}}$ = Unit tensor, [-]

$k_{\Theta_s}$ = Diffusion coefficient, [m$^{2}$·s$^{-1}$]

and

$$\gamma_{\Theta_s} = \frac{12\left(1-e_{ss}^2\right)g_{0,ss}}{d_s\sqrt{\pi}}\rho_s\varepsilon_s^2\Theta_s^{3/2} \tag{2.63}$$

$$\phi_{ls} = -3K_{ls}\Theta_s \tag{2.64}$$

$e_{ss}$ = Restitution coefficient for solid-solid collisions, [-]

$d_s$ = Particle diameter of solid phase, [m]

$g_{0,ss}$ = Radial distribution coefficient, [-], described in eq. (2.84)

**4) Chemical species conservation**

General equation of chemical species conservation for a species k in a single phase is as the following (ANSYS, 2013).

$$\frac{\partial}{\partial t}(\rho Y_k)+\nabla\cdot(\rho\vec{v}Y_k) = -\nabla\cdot\vec{J}_k+R_k+S_k \tag{2.65}$$

In multiphase flow, the conservation of the species k in phase q is

$$\frac{\partial}{\partial t}\left(\varepsilon^q\rho^q Y_k^q\right)+\nabla\cdot\left(\varepsilon^q\rho^q\vec{v}^q Y_k^q\right) = -\nabla\cdot\left(\varepsilon^q\vec{J}_k^q\right)+\varepsilon^q R_k^q+\varepsilon^q S_k^q + \sum_{p=1}^{n}\left(\dot{m}_{p^k q^k}-\dot{m}_{q^k p^k}\right) \tag{2.66}$$

where

$Y_k^q$ = Mass fraction of species k in phase q, [-]

$\vec{J}_k^q$ = Mass flux of species k into phase q, [kg·m$^{-2}$·s$^{-1}$]

$R_k^q$ = Net rate of species k produced by homogeneous reactions inside phase q, [kg·m$^{-3}$·s$^{-1}$]

$S_k^q$ = Rate of creation of species k by addition from dispersed phase and other sources in phase q, [kg·m$^{-3}$·s$^{-1}$]

**5) Source terms due to heterogeneous reactions**

Previous conversation equations per phase, as eqs. (2.57), (2.59)-(2.61) and (2.66), can use for system which has no reaction or has only homogeneous reactions. Whereas when heterogeneous reactions occur, there are appearances and disappearance of some molecules in the phase, so a source of mass, momentum, energy or species transfer must be added in each regarding conversation equations. The sources terms due to heterogeneous reactions are described as follows:

**5.1) Mass transfer**

The reactant and the product side of a reaction are represented by r and p, respectively.

$$S_{r_q} = -\acute{R} \sum_{r_q} \left( \gamma_j^r M_j^r \right) \tag{2.67}$$

$$S_{p_q} = \acute{R} \sum_{p_q} \left( \gamma_j^p M_j^p \right) \tag{2.68}$$

The mass transfer to phase q due to a heterogeneous reaction (ANSYS, 2013) is

$$S_q = S_{p_q} + S_{r_q} \tag{2.69}$$

where

$\gamma_j$ = Stoichiometric coefficient of species j which involved in the reaction, [-]

$M_j$ = Molecular weight of species j which involved in the reaction, [kg·kmol$^{-1}$]

$\acute{R}$ = Rate of a heterogeneous reaction, [kmol·m$^{-3}$·s$^{-1}$]

### 5.2) Momentum transfer

The net velocity of the reactants is expressed as

$$\vec{v}_{net} = \frac{\Sigma_r\left(\gamma_j^r M_j^r \vec{v}_{r_j}\right)}{\Sigma_r\left(\gamma_j^r M_j^r\right)} \tag{2.70}$$

The momentum transfer to phase q due to a heterogeneous reaction (ANSYS, 2013) is

$$S_q^{\vec{v}} = S_{p_q}\vec{v}_{net} \text{-} \acute{R}\sum\nolimits_{r_q}\left(\gamma_j^r M_j^r \vec{v}_q\right) \tag{2.71}$$

where

$\vec{v}_{r_j}$ = Velocity of a reactant j which involved in the reaction, [m·s$^{-1}$]

$\vec{v}_q$ = Velocity of phase q, [m·s$^{-1}$]

### 5.3) Heat transfer

The net enthalpy of the reactants is expressed as

$$H_{net} = \frac{\Sigma_r\left(\gamma_j^r M_j^r \langle H_j^r + H_j^{f^r} \rangle\right)}{\Sigma_r\left(\gamma_j^r M_j^r\right)} \tag{2.72}$$

The heat transfer to phase q due to a heterogeneous reaction (ANSYS, 2013) is

$$S_q^H = S_{p_q} H_{net} \text{-} \acute{R}\left[\sum\nolimits_{r_q}\left(\gamma_j^r M_j^r H_j^r\right) + \sum\nolimits_{p_q}\left(\gamma_j^p M_j^p H_j^{f^p}\right)\right] \tag{2.73}$$

where

$H_j$ = Specific enthalpy of species j which involved in the reaction, [m$^2$·s$^{-2}$, J·kg$^{-1}$]

$H_j^f$ = Specific formation enthalpy (heat of formation) of species j which involved in the reaction, [m$^2$·s$^{-2}$, J·kg$^{-1}$]

### 5.4) Species transfer

Similar with mass transfer, sources terms for each species k are

$$S_{r_q^k} = \text{-}\acute{R}\sum\nolimits_{r_q^k}\left(\gamma_j^{r^k} M_j^{r^k}\right) \tag{2.74}$$

$$S_{p_q^k} = \acute{R} \sum_{p_q^k} \left( \gamma_j^{p^k} M_j^{p^k} \right) \tag{2.75}$$

The species transfer to phase q of the species k due to a heterogeneous reaction (ANSYS, 2013) is

$$S_q^k = S_{p_q^k} + S_{r_q^k} \tag{2.76}$$

### 2.5.2.2 Constitutive equations

**1) Stress tensor**

In a single phase, the stress tensor ($\bar{\tau}$) is given by

$$\bar{\tau} = \mu \left[ (\nabla\vec{v} + \nabla\vec{v}^{T}) - \frac{2}{3} \nabla\cdot\vec{v}\bar{I} \right] \tag{2.77}$$

and in multiphase, the stress tensor for phase q (ANSYS, 2013) is

$$\bar{\tau}_q = \varepsilon_q \mu_q \left( \nabla\vec{v}_q + \nabla\vec{v}_q^{T} \right) + \varepsilon_q \left( \lambda_q - \frac{2}{3} \mu_q \right) \nabla\cdot\vec{v}_q \bar{I} \tag{2.78}$$

where

$\mu_q$ = Shear viscosity of phase q, [Pa·s]. For solid phase, this is described in eq. (2.79)

$\lambda_q$ = Bulk viscosity of phase q, [Pa·s]. For solid phase, this is described in eq. (2.82)

**2) Solid shear viscosity**

In solid phase, the shear viscosity involves viscosities from collision, kinetics and friction (optional). Thus, the solid shear viscosity ($\mu_s$) is given as

$$\mu_s = \mu_{s,col} + \mu_{s.kin} + \mu_{s,fr} \tag{2.79}$$

where the collisional viscosity is

$$\mu_{s,col} = \frac{4}{5}\varepsilon_s\rho_s d_s g_{0,ss}(1+e_{ss})\left(\frac{\Theta_s}{\pi}\right)^{1/2}\varepsilon_s \quad (2.80)$$

and the kinetic viscosity is applied from Gidaspow *et al.* (ANSYS, 2013) as

$$\mu_{s,kin} = \frac{10\rho_s d_s\sqrt{\Theta_s\pi}}{96\varepsilon_s(1+e_{ss})g_{0,ss}}\left[1+\frac{4}{5}\varepsilon_s g_{0,ss}(1+e_{ss})\right]^2\varepsilon_s \quad (2.81)$$

### 3) Solid bulk viscosity

The solid bulk viscosity ($\lambda_s$) expression accords to Lun *et al.* (ANSYS, 2013) as

$$\lambda_s = \frac{4}{3}\varepsilon_s^2\rho_s d_s g_{0,ss}(1+e_{ss})\left(\frac{\Theta_s}{\pi}\right)^{1/2} \quad (2.82)$$

### 4) Solid Pressure

The solid pressure ($p_s$) is in functions of the granular temperature given by Lun *et al.* (ANSYS, 2013). The expression which consists of terms of kinetic energy and particle collision, is as the following.

$$p_s = \varepsilon_s\rho_s\Theta_s+2\varepsilon_s^2\rho_s\Theta_s g_{0,ss}(1+e_{ss}) \quad (2.83)$$

### 5) Radial distribution coefficient

For single solid phase, the radial distribution coefficient ($g_{0,ss}$) is modified by Lun *et al.* (ANSYS, 2013) as the following.

$$g_{0,ss} = \left[1-\left(\frac{\varepsilon_s}{\varepsilon_{s,max}}\right)^{1/3}\right]^{-1} \quad (2.84)$$

Where

$\varepsilon_{s,max}$ = Maximum packing of solid phase, [-]

For mutual solid phases between phase s and another solid phase l, the mutual radial distribution coefficient ($g_{0,ls}$) is given as

$$g_{0,ls} = \frac{d_s g_{0,ll} + d_l g_{0,ss}}{d_s + d_l} \tag{2.85}$$

**6) Granular temperature from KTGF**

The granular temperature ($\Theta_s$) is the representative of energy in KTGF as described previously and can be evaluated from the kinetic fluctuation energy conservation as eq. (2.62). Algebraic formulation is able to simplify the conservation equation by neglecting convection and diffusion term as an equation below (ANSYS, 2013).

$$\frac{3}{2}\frac{\partial}{\partial t}(\varepsilon_s \rho_s \Theta_s) = (-p_s \bar{I} + \bar{\tau}_s):\nabla \vec{v}_s - \gamma_{\Theta_s} + \phi_{ls} \tag{2.86}$$

**7) Gas-solid momentum exchange coefficient**

The gas-solid momentum exchange coefficient ($K_{sg}$) is defined as

$$K_{sg} \equiv K_{gs} = \frac{\varepsilon_s \rho_s f_{drag}}{\tau_s} \tag{2.87}$$

where

$\tau_s$ = Particulate relaxation time in solid phase, [s], given as

$$\tau_s = \frac{\rho_s d_s^2}{18\mu_g} \tag{2.88}$$

Due to drag function ($f_{drag}$) is dependent to drag coefficient ($C_D$) and one of the proper drag functions is Gidaspow's drag model, thus the gas-solid momentum exchange coefficients from Gidaspow's drag model are as follows (ANSYS, 2013):

- When $\varepsilon_g > 0.8$;

$$K_{sg} = \frac{3}{4} C_D \frac{\varepsilon_s \varepsilon_g \rho_g |\vec{v}_s - \vec{v}_g|}{d_s} \varepsilon_g\text{-}2.65 \tag{2.89}$$

$$C_D = \frac{24}{\varepsilon_g Re_s}\left[1 + 0.15(\varepsilon_g Re_s)^{0.687}\right] \tag{2.90}$$

- When $\varepsilon_g \leq 0.8$;

$$K_{sg} = 150\frac{\varepsilon_s(1-\varepsilon_g)\mu_g}{\varepsilon_g d_s^2} + 1.75\frac{\rho_g \varepsilon_s |\vec{v}_s - \vec{v}_g|}{d_s} \tag{2.91}$$

Where

$\mathrm{Re}_s$ = Particle Reynolds number of solid phase, [-], described in eq. (2.51)

**8) Solid-solid momentum exchange coefficient**

The solid-solid momentum exchange coefficient ($K_{ls}$, l is another solid phase) is expressed (ANSYS, 2013) as

$$K_{ls} \equiv K_{sl} = \frac{3(1+e_{ls})\left(\frac{\pi}{2}+C_{fr,ls}\frac{\pi^2}{8}\right)\varepsilon_s\rho_s\varepsilon_l\rho_l(d_l+d_s)^2 g_{0,ls}}{2\pi\left(\rho_l d_l^3+\rho_s d_s^3\right)}|\vec{v}_l-\vec{v}_s| \tag{2.92}$$

where

$e_{ls}$ = Restitution coefficient for solid-solid collisions, [-], means as same as $e_{ss}$

$C_{fr,ls}$ = Friction coefficient between solid phases, [-]

$g_{0,ls}$ = Radial distribution coefficient of mutual solid phases, [-], described in eq. (2.85)

**9) Gas-solid heat exchange coefficient**

The interphase heat exchange coefficient between solid phase and gas phase ($h_{sg}$) is expressed as an equation below (ANSYS, 2013).

$$h_{sg} \equiv h_{gs} = \frac{k_g \mathrm{Nu}_s}{d_s} \tag{2.93}$$

Where

$k_g$ = Thermal conductivity of gas phase, [$W \cdot m^{-1} \cdot K^{-1}$]

$\mathrm{Nu}_s$ = Nusselt number of solid phase, [-], which has a correlation from Gunn's model (ANSYS, 2013) as

$$\mathrm{Nu_s} = \left(7\text{-}10\varepsilon_g + 5\varepsilon_g^2\right)\left(1 + 0.7\mathrm{Re}_s^{0.2}\mathrm{Pr}^{1/3}\right) + \left(1.33\text{-}2.4\varepsilon_g + 1.2\varepsilon_g^2\right)\mathrm{Re}_s^{0.7}\mathrm{Pr}^{1/3} \qquad (2.94)$$

with $\mathrm{Pr}$ = Prandtl number of gas phase, [-], as

$$\mathrm{Pr} = \frac{C_{p_g}\mu_g}{k_g} \qquad (2.95)$$

$C_{p_g}$ = Heat capacity of gas phase, [J·kg$^{-1}$·K$^{-1}$]

### 2.5.3 Discretization

Discretization is mathematic process to calculate solutions from differential equations by transforming to algebraic equations. Problems are solved via numerical methods by computer programs. Conventional discretization methods which widely utilized are 3 methods i.e. finite difference method (FDM), finite element method (FEM) and finite volume method (FVM) (Prajongkan, 2011). FVM is the most suitable for fluid dynamics problems and used in this dissertation.

#### 2.5.3.1 Finite volume method (FVM)

FVM (ANSYS, 2013; Uriz *et al.*, 2013) is a discretization method which divides a domain of a problem into small control volumes (cells) and integrates the conservative equation on all control volumes as

$$\int_V \frac{\partial\rho\phi}{\partial t}\,dV + \oint \rho\phi\vec{v}\cdot d\vec{A} = \oint \Gamma\nabla\phi\cdot d\vec{A} + \int_V S_\phi\,dV \qquad (2.96)$$

where

$\phi$ = Properties parameter

$\vec{A}$ = Area vector

$\Gamma$ = Diffusion coefficient of $\phi$

$S_\phi$ = Source of $\phi$ per unit volume

Because integral forms of conservative equations are difficult to solve directly, differential forms of a cell are determined as

$$\frac{\partial\rho\phi}{\partial t}V+\sum_{f}^{N_{faces}}\left(\phi_f\rho_f\vec{v}_f\cdot\vec{A}_f\right) = \sum_{f}^{N_{faces}}\left(\Gamma\nabla\phi_f\cdot\vec{A}_f\right)+S_{\phi}V \qquad (2.97)$$

where

$N_{faces}$ = Number of faces enclosing the cell

$\phi_f$ = Value of $\phi$ convected through face f

$\vec{A}_f$ = Area of face f

$\rho_f\vec{v}_f\cdot\vec{A}_f$ = Mass flux through face f

$V$ = Cell volume

In eq. (2.97), the $\frac{\partial\rho\phi}{\partial t}V$ is time dependent term. This term is neglected if considered in steady state, but for transient problems this derivative must be discretized by small time different ($\Delta t$). Dividing the domain in to small cells is called "*spatial discretization*" and dividing time into time steps called "*temporal discretization*" (ANSYS, 2013).

To solve a time dependent problem, solutions of $\phi$ of cells in the domain will be calculated cell by cell firstly in a same time step then use these new $\phi$ of each cell for solving in the next time step.

**1) Spatial discretization**

Figure 2.12 demonstrates simple regular cell in 2D directions with a center of considered cell called node P. the differential form of conservation at node P is derived as the following (Uriz *et al.*, 2013).

$$\begin{aligned} 0 &= -(v_xA\phi)_e+(v_xA\phi)_w-(v_xA\phi)_n+(v_xA\phi)_s \\ &\quad +\left(\Gamma A\frac{\partial\phi}{\partial x}\right)_e-\left(\Gamma A\frac{\partial\phi}{\partial x}\right)_w+\left(\Gamma A\frac{\partial\phi}{\partial y}\right)_n-\left(\Gamma A\frac{\partial\phi}{\partial y}\right)_s+S_{\phi}V \end{aligned} \qquad (2.98)$$

The four-direction derivatives in eq. (2.98) can be calculated, for example in direction e, as

$$\left(\Gamma A\frac{\partial\phi}{\partial x}\right)_e = \Gamma_e A_e\left(\frac{\phi_P - \phi_E}{\delta_{x,EP}}\right) \tag{2.99}$$

where

$\delta_{x,EP}$ = distance between nodes E and P

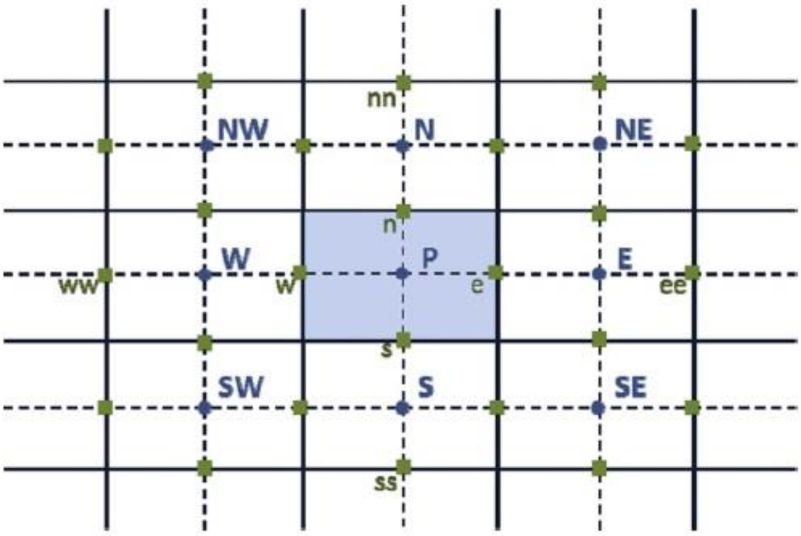

**Figure 2.12** The 2D regular mesh demonstrated relation between reference cell and it neighbor cells.

**Source:** Uriz *et al.* (2013)

The new values of $\phi_e$ at surface node e will able to be evaluated from known $\phi$ at center nodes nearby. There are several procedures (Uriz *et al.*, 2013) to calculate the $\phi_e$ as follows:

### 1.1) Upwind differencing scheme (UDS)

This scheme has two types to use i.e. first order upwind scheme and second order upwind scheme. The first order upwind scheme is simple and very stable but inaccuracy, wherase second order upwind scheme gives more accuracy. To prevent divergence due to negative values, direction of forces e.g. $F_e = \rho v_x$ is decided for evaluate $\phi_e$ as equations below (Prajongkan, 2011; Uriz *et al.*, 2013).

First order upwind;

$$\phi_e = \phi_P \quad \text{when } F_e > 0 \qquad (2.100)$$

$$\phi_e = \phi_E \quad \text{when } F_e < 0 \qquad (2.101)$$

Second order upwind;

$$\phi_e = \frac{3}{2}\phi_P - \frac{1}{2}\phi_w \quad \text{when } F_e > 0 \qquad (2.102)$$

$$\phi_e = \frac{3}{2}\phi_E - \frac{1}{2}\phi_{ee} \quad \text{when } F_e < 0 \qquad (2.103)$$

### 1.2) Central differencing scheme (CDS)

$$\phi_e = \frac{\delta_{x,Ee}\phi_E + \delta_{x,eP}\phi_P}{\delta_{x,EP}} \qquad (2.104)$$

### 1.3) Quadratic Upstream Interpolation for Convective Kinetics (QUICK)

$$\phi_e = -\frac{1}{8}\phi_{ee} + \frac{6}{8}\phi_E + \frac{3}{8}\phi_P \qquad (2.105)$$

Even though proper scheme is selected, after lots of iterations new value of $\phi$ is sometimes converged too early that brings an unstable situation or divergence. Under-relaxation factor (URF, $\alpha$) is coupled to reduce a large change of a new value in every iteration (Prajongkan, 2011) as

$$\phi_{eff} = \phi_{old} + \alpha\Delta\phi \tag{2.106}$$

where

$\phi_{eff}$ = Effective value of $\phi$ that to be used

$\phi_{old}$ = Old value of $\phi$ from previous iteration

$\Delta\phi$ = Difference between new and old value of $\phi$ after this iteration

**2) Temporal discretization**

The temporal discretization is a method to transform time derivative into algebraic from. Give time derivative of $\phi$ is a function of $\phi$ as

$$\frac{\partial\phi}{\partial t} = F(\phi) \tag{2.107}$$

There are two common types of temporal discretization (ANSYS, 2013) to solve the derivative as follows:

First order discretization;

$$\frac{\phi^{n+1}-\phi^{n}}{\Delta t} = G(\phi) \tag{2.108}$$

Second order discretization;

$$\frac{3\phi^{n+1}-4\phi^{n}+\phi^{n-1}}{2\Delta t} = G(\phi) \tag{2.109}$$

Where

$\phi^{n+1}$ = Value of $\phi$ at next time step ($t+\Delta t$)

$\phi^{n}$ = Value of $\phi$ at current step ($t$)

$\phi^{n-1}$ = Value of $\phi$ at previous time step ($t-\Delta t$)

$G(\phi)$ = New function of $\phi$ which defined from $F(\phi)$ dependent on a method as the following (Uriz *et al.*, 2013).

Explicit method;

$$G(\phi) = F(\phi^{n}) \tag{2.110}$$

Implicit method;

$$G(\phi) = F\left(\phi^{n+1}\right) \tag{2.111}$$

Crank-Nicolson method;

$$G(\phi) = \frac{F(\phi^{n}) + F\left(\phi^{n+1}\right)}{2} \tag{2.112}$$

If chose derivative discretization with second order as a function of implicit method, this well-known method is called the second order implicit method. This method is suitable for fluid dynamic problems (ANSYS, 2013).

### 2.5.3.2 SIMPLE (solution algorithm)

When solving the momentum and mass conservative (continuity) equations and find a new value of pressure or velocity. The values of pressures and velocities might not conform to the continuity equation. Semi Implicit Method for Pressure Linked Equations (SIMPLE) proposed by Patankar and Spalding (1972) has been utilized to find the conforming values. Then Patankar revised a new SIMPLE algorithm called SIMPLE revised (SIMPLER) in 1980 and afterward, van Doormal and Raithby proposed a variation of SIMPLE called SIMPLE consistent (SIMPLEC) in 1984 (Ranade, 2002). The algorithms of SIMPLE are shown in figure 2.13.

In SIMPLEC an initial guessed pressure field is used solving in discretized momentum equations to calculate a velocity field (if in SIMPLER the initial guessed velocity field is used to solve the pressure field, alternatively). Then use the velocity put in continuity equation with pressure-correction method to solve the pressure. Repeat calculations until the pressure and velocity are converged and conform to the both conservative equations (Ranade, 2002; Prajongkan, 2011).

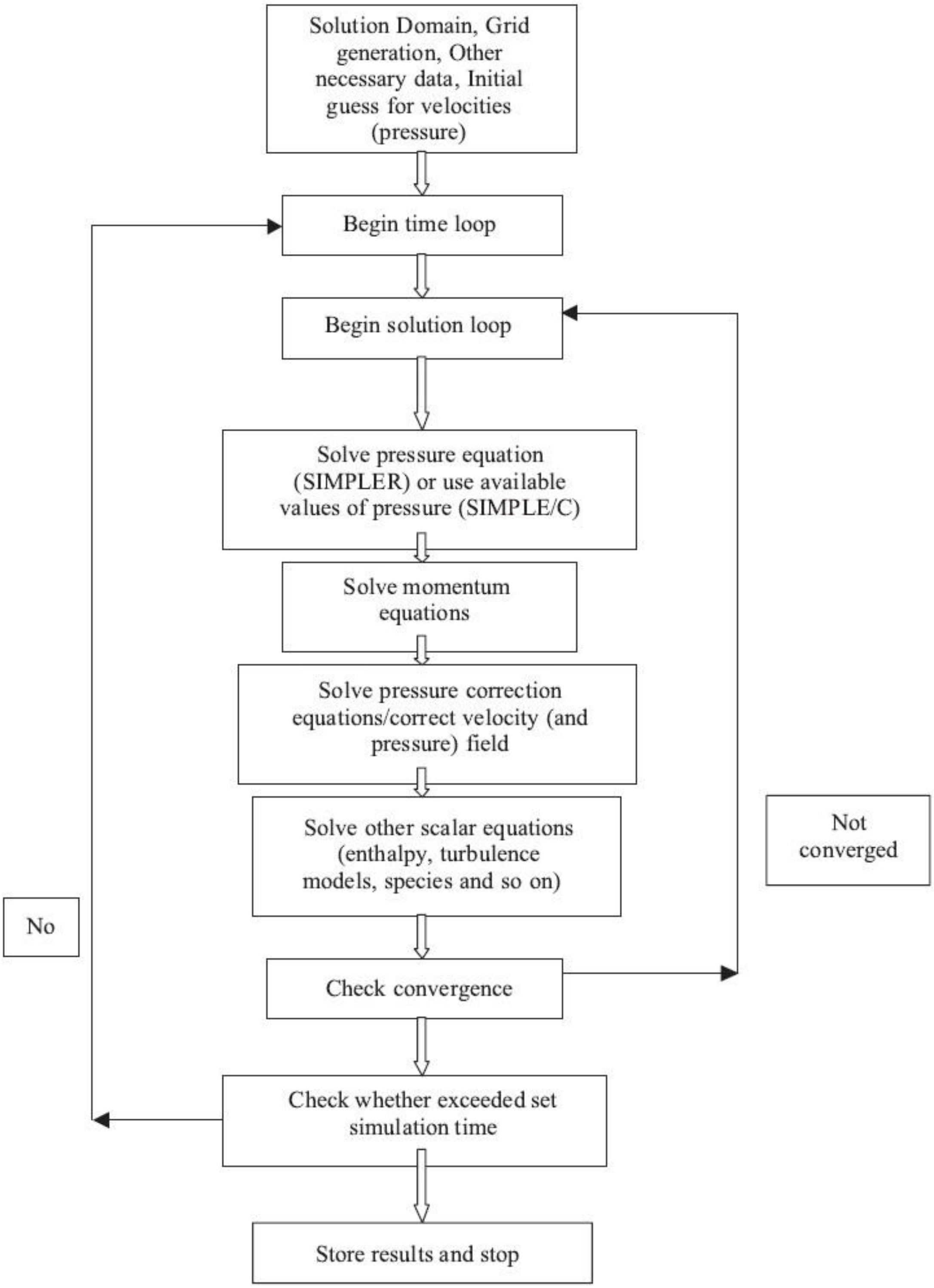

**Figure 2.13** Algorithms of Semi Implicit Method for Pressure Linked Equation (SIMPLE) for unsteady flows.

**Source:** Ranade (2002)

## 2.6 Relating literature

Mousa *et al.* (2014) investigated hydrodynamics of a riser part of CFBR applied for reforming catalyst which considered in Geldart's type A particles. The Euler-Euler models with KTGF and the standard k-ε turbulence model is applied in 2D cold-flow simulations by Fluent®. They investigated effects of solid flux in 250-1,500 kg·m$^{-2}$·s$^{-1}$ on appearance of different regime, i.e. fast fluidization, pneumatic transport and dense suspension upflow (DSU), and on mixing of the catalyst related to reaction performance. Results showed that the riser should be operated under high solid fraction (>15%) at inlet zone and high solids flux exceeding 500 kg·m$^{-2}$·s$^{-1}$ for the optimum condition of steam reforming (gas flux of 6.78 kg·m$^{-2}$·s$^{-1}$ operating at 5 atm and 923 K)

Johnsen *et al.* (2006) studied experiments of SESMR in a bubbling fluidized bed reactor (BFBR) of 0.1 m diameter and 0.66 heights. The reforming on Ni-based catalyst and dolomite were performed in cyclic modes at 1 atm, 600°C and S/C = 4. They investigated effects of different gas velocities of 0.032, 0.064 and 0.096 m·s$^{-1}$. The results showed that there was not different effect among various gas velocities due to SESMR is fast enough and complete reactions within dense beds. All effluent gas contained $H_2$ about 98-99% in dry basis after four reforming/calcination cycles. SESMR period time decreased after numbers of cycles.

Johnsen *et al.* (2006) extended their previous SESMR experiments to modeling of dual bubbling bed reactors with solid circulation. They investigated various solid recirculation rates and volumetric Cat/Sorb to optimize the system energy efficiency. The steady two-phase models were solved by coding in assumptions and conditions;

solids phase consists of Ni-based catalyst and dolomite, operate isothermal at 600°C, ambient pressure, and a superficial gas velocity of 0.1 m·s$^{-1}$. The reaction rates were not affected by the number of cycles and a make-up flow of fresh sorbent was added to the system if CaO conversion of sorbent is over 28%. The reactors were modeled in pilot-scale of 1 m diameter with static bed oh 0.3 m height. The results showed that high solids circulation rates reduced the need of adding fresh sorbent and gave higher system efficiencies than the case that fresh solid was added. For S/C = 4 and temperature of gas feed of 250°C, the best case showed that when solid recirculation rates is 5.1 kg$_{sorbent}$·min$^{-1}$ and volumetric Cat/Sorb is 0.9, the effluent gas contained $H_2$ 98% in dry basis.

Di Carlo *et al.* (2010) studied SESMR in a bubbling fluidized bed reactor of 0.1 m diameter simulated using 2D Euler-Euler models in Fluent®. The solids consisted of dolomite and Ni-based catalyst with a static bed height of 0.2 m. They investigated hydrodynamic behavior of the bed in various volumetric dolomite/catalyst ratios of 0-5. The results showed the optimum case that $H_2$ mole fraction was over 0.93 at temperatures of 900 K and a superficial gas velocity of 0.3 m·s$^{-1}$ with a dolomite/catalyst ratio is more than 2. And when the dolomite/catalyst ratio was higher than 2, the heat for the reforming endothermic reactions could be almost entirely supplied by the exothermic reaction of carbonation.

Wu *et al.* (2014) studied 2D models simulation of SESRE on K-Ni-Cu/HTCl multifunctional catalyst in four parallel fixed-bed adsorptive reactors. The reactors were pilot-scaled of horizontal tubes with 0.1 m diameter and 6 m bed length. The processes were operated by pressure swing concept with 7 steps i.e. reforming, rinse, pressurization, blowdown, regeneration, received pressurization and purge. The results showed that when SESRE was operated at 773 K and by 1000 s per cycle, hydrogen production was continuous and cyclically steady with $H_2$ purity more than 99% in dry basis and CO content 25 ppm. The ratio between energy output and input was found around 1.7.

Lysikov *et al.* (2015) experimented SESRE on admixture of CaO sorbent and Ni-based catalyst in dual fixed bed reactors. The processes operated periodically in 4 steps: sorption-reforming, regeneration, catalyst reduction and pressurization. Each of dual reactors had 16 mm diameter and 500 mm bed height consisting 50 g of sorbent and 5 g of catalyst. They focused on regeneration between using temperature swing adsorption (TSA) technique and pressure swing adsorption (PSA) technique. The results showed that maximum purity of hydrogen was approximately 99% in dry basis in which TSA was applied at the temperature gradient on at the range of 650-750°C of reforming step and 675-775°C of regeneration step. Both the CaO sorbent and the Ni-based catalyst had stable and effective operations over 250 cycles.

# CHAPTER 3

# METHODOLOGY

## 3.1 Basics

CFD modeling is consisted of three global processing steps i.e. pre-processing, processing and post-processing. Practical steps in general CFD process are as follows:

1. Defining geometry of the fluid system (pre-processing)
2. Locating boundary and defining boundary condition (pre-processing)
3. Specifying fluid models and properties (pre-processing)
4. Generating mesh (pre-processing)
5. Defining considering parameters (processing)
6. Solving the models (pre-processing)
7. Collecting and analyzing results (post-processing)

### 3.1.1 CFD process

There were amount of commercial CFD programs which could be utilized for each simulation steps including geometry drawing, meshing, setting up, solving (calculating) and post processing as shown in figure 3.1. CFD package and programs used in this dissertation were consisted of

- ANSYS® DesignModeler™ (Geometry)
- ANSYS® Meshing™ (Meshing)
- ANSYS® Fluent® (Set up and Calculation)
- ANSYS® CFD Post and Microsoft® Office Excel® (Post processing)

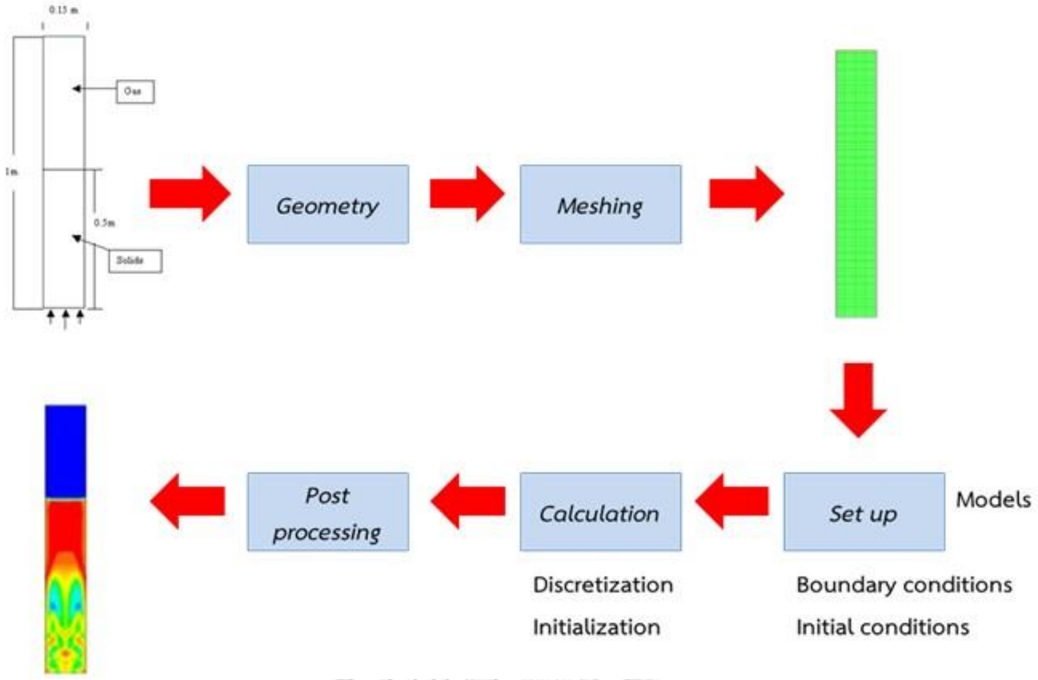

**Figure 3.1** Steps of CFD modeling.

Four of above ANSYS® products were connected in a series by ANSYS® Workbench™ 2.0 Framework and all were in version 15.0.7.

### 3.1.2 Pre-processing data

From literature reviews, Johnsen *et al.* (2006) extended his experiment, in single bubbling bed reformer, by scale-up simulating to pilot scale and included regenerator in dual bubbling fluidized bed reactors as well as Sánchez *et al.* (2012). They both simulated by coding that Johnsen *et al.* (2006) simulated with constant circulating solids but Sánchez *et al.* (2012) simulated solid return between the reactors, simultaneously. Their results were sufficient and helpful for more realistic design and investigating phenomena inside CFBR system via CFD programs such as ANSYS® Fluent®

which were used in this dissertation. The summary of pre-processing for preliminary data is shown in figure 3.2.

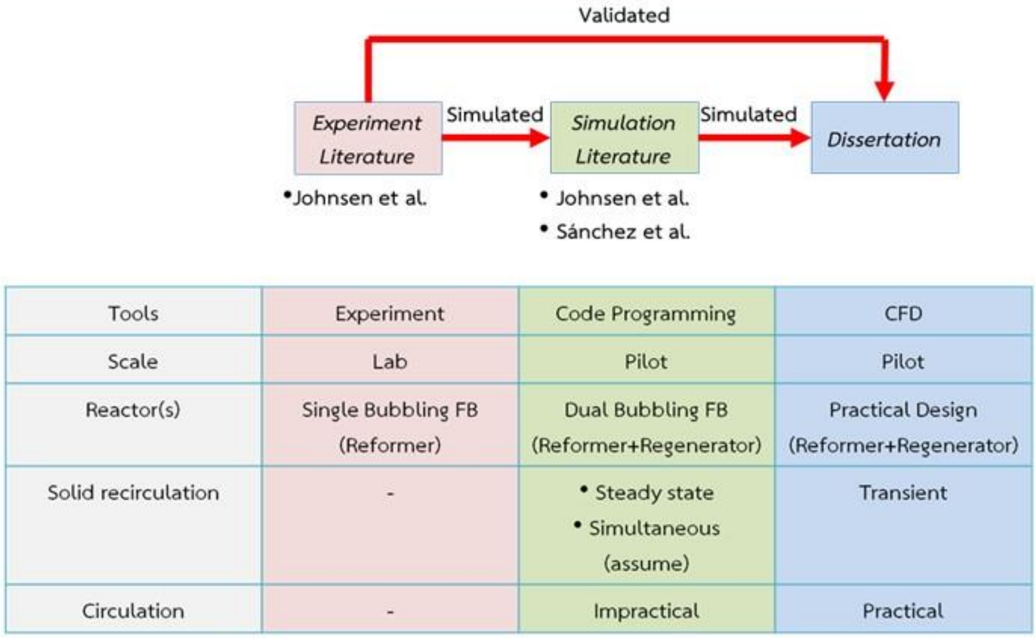

| Tools | Experiment | Code Programming | CFD |
|---|---|---|---|
| Scale | Lab | Pilot | Pilot |
| Reactor(s) | Single Bubbling FB (Reformer) | Dual Bubbling FB (Reformer+Regenerator) | Practical Design (Reformer+Regenerator) |
| Solid recirculation | - | • Steady state<br>• Simultaneous (assume) | Transient |
| Circulation | - | Impractical | Practical |

**Figure 3.2** Pathway of preliminary data involved in dissertation.

Because the dual bubbling fluidized bed reactors systems from both Johnsen *et al.* (2006) and Sánchez *et al.* (2012) were quite impractical or complicated to operate solid circulation. In this dissertation, one or both of reactors should be change to riser type with high gas velocity for blowing solids off. According to very fast kinetics of reforming and profit of feed increase via using higher velocity of gas, reformer was interesting to be the riser. Whereas regenerator needed sufficient resident time for slower kinetic of decarbornation to nearly complete removing undesired $CO_2$, so regenerator should still be bubbling bed reactor. A new preliminary reforming reactor was designed according to a basic design and calculation from Kunii and Levenspiel (1991), as well as other units of CFBR system were shown in figure 3.3. The preliminary parameters in table 3.1 were also chosen according to their previous works with the best results.

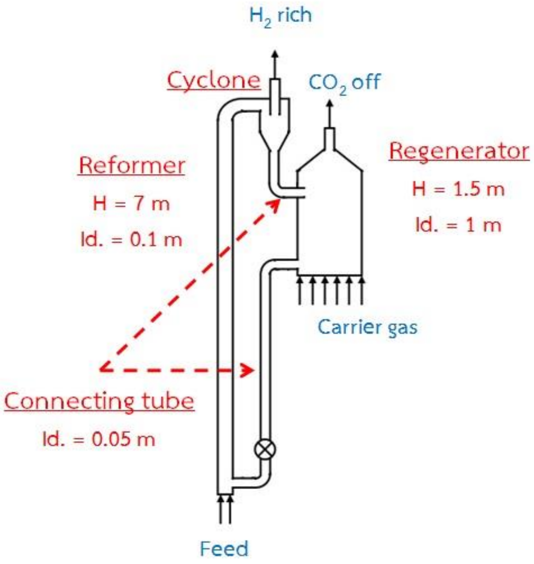

**Figure 3.3** Preliminary design of CFBR system.

**Table 3.1** Preliminary parameters of CFBR system design.

| Parameters | Value | |
|---|---|---|
| S/C (SESMR) | 4 | - |
| S/E (SESRE) | 6 | - |
| Cat/Sb | 0.16 | kg/m$^3$ |
| $T_{reformer}$ | 600 | °C |
| $T_{regenerator}$ | 900 | °C |
| $U_1$ (reformer) | 5 | m/s$^1$ |
| $U_2$ (regenerator) | 0.1 | m/s$^1$ |
| Catalyst density | 2,200 | kg/m$^3$ |
| Calcined dolomite density | 1,540 | kg/m$^3$ |
| Mean catalyst particle size | 200 | µm |
| Mean dolomite particle size | 250 | µm |

### 3.1.3 Goal and constraints of design

<u>Goal</u>

To maximize the rate of $H_2$ production under the following constraints.

<u>Constraints</u>

1. The reformer is operated the same or better performance compared to BFB or fixed operation (experiment case) i.e. high $H_2$ purity (∼99% in dry basis) of effluence.

2. CaO conversion ($X_{CaO}$) off the reformer should not over 28% for stable $CO_2$ capture in continuous operation.

3. Decarbonation of sorbent is sufficient that $X_{CaO}$ off the regenerator should drops close to 0% like fresh sorbent.

## 3.2 Global setting in ANSYS® Fluent®

<u>General</u>

**Solver type**: Pressure-base **Time**: Transient

**2D space**: Planar

<u>Models</u>

**Multiphase**: Eulerian **No. of Eulerian phases**: 3

**Vol. Fraction parameters**: Implicit scheme

Materials, phases and properties

**Materials**: 1) Gas phase = mixture of EtOH, $CH_4$, $H_2O$, CO, $CO_2$, $H_2$ and inert $N_2$ (for initial balance)

2) Catalyst phase = single fluid of Ni-base catalyst*

3) Sorbent phase = mixture of CaO, $CaCO_3$ and MgO*

*Ni-base catalyst and MgO are additional materials apart from Fluent® database

**Mixture properties**: see table 3.2

**Table 3.2** Property models for mixtures in each phase.

| Properties | Gas phase | Catalyst phase | Sorbent phase |
|---|---|---|---|
| Density | vol. weighted mixing law | constant | UDF |
| $C_P$ (specific heat) | mixing law | mixing law | |
| Thermal conductivity | mass weighted mixing law | mass weighted mixing law | |
| Viscosity | mass weighted mixing law | mass weighted mixing law | |
| Mass Diffusivity | constant dilute appx. | kinetic theory | |

**Phases**: 1) Gas phase = primary phase

2) Catalyst phase = secondary phase with Granular chosen

3) Sorbent phase = secondary phase with Granular chosen

**Granular phase properties**: see table 3.3

**Table 3.3** Property models of granular phases.

| Properties | Catalyst phase | Sorbent phase |
|---|---|---|
| Diameter | constant | constant |
| Granular viscosity | Gidaspow | Gidaspow |
| Granular bulk viscosity | Lun *et al.* | Lun *et al.* |
| Frictional viscosity | none | none |
| Granular temperature | algebraic | algebraic |
| Solids pressure | Lun *et al.* | Lun *et al.* |
| Radial distribution | Lun *et al.* | Lun *et al.* |
| Packing limit | constant | constant |

**Phase interaction**: see table 3.4

**Table 3.4** Coefficient values and models of phase interaction.

| Interaction | Catalyst-Gas | Sorbent-Gas | Sorbent-Catalyst |
|---|---|---|---|
| Drag coefficient | Gidaspow | Gidaspow | Symmetric |
| Restitution coefficient | constant | constant | constant |
| Heat transfer coefficient | Gunn | Gunn | none |

**<u>Reactions</u>**

Kinetic rates of SMR, SRE, carbonation and decarbonation as eqs. 2.12-2.14, 2.27 and 2.29 are derived to be compatible in Fluent® by writing in C-language user define functions (UDFs). These rates must be compiled and returned value in volumetric rates of heterogeneous reactions as the following derive.

$$R_i = \eta_i \varepsilon_p \rho_p r_i \tag{3.1}$$

Where

$R_i$ = Volumetric rate of reaction i, [kmol·m$^{-3}$·s$^{-1}$]

$\eta_i$ = Reaction effectiveness factor, [-], that involved pore diffusion resistance and surface phenomena. According to Di Carlo *et al.* (2010), choose 0.7, 0.8 and 0.4 for bSMR, WGS and gSMR, respectively, and assume 1.0 for other reactions as well as in Sánchez *et al.* (2012).

$\varepsilon_p$ = Volume fraction of particle phase, [-]

$\rho_p$ = Density of particle, [kg·m$^{-3}$]

<u>Boundary conditions</u>

**Inlet type**: Velocity-inlet / Magnitude, Normal to Boundary

**Outlet type**: Pressure-outlet / Atmosphere / Normal to Boundary (Backflow)

**Wall type**: Stationary Wall / No slip / Adiabtic

<u>Solution methods and controls</u>

**Pressure-velocity coupling scheme**: Phase coupled SIMPLE

**Transient formulation**: Second order implicit

<u>Calculation</u>

**Time step size**: 0.001 s

**Max iteration per time step**: 50 (for the riser part)

100 (for the regenerator part)

### 3.3 Study Methods

To achieve the objective of CFBR system design for SESMR/SESRE process, many parameters e.g. sizes of reformer and regenerator, gas velocity to reactors, circulated solid flux, steam to carbon ratio, catalyst to sorbent ratio and temperature of gas inlets, should be investigated. Due to complexity and large scale of system, the CFBR system had to be investigated separately into the riser part and the regenerator part. Firstly, the reforming riser of both SESMR and SESRE had been investigated to find the best suitable system of each process. Then some results from the riser part would be related and chosen in the regenerator part. In each part, grid and time refinement had to be performed before investigating any parameters. Generally, some phase and system properties were set the same in the both part as shown in table 3.5.

**Table 3.5** The phase and system properties used in models.

| Phase properties | Value | |
|---|---|---|
| Phase properties | | |
| Catalyst density | 2,200 | kg/m$^3$ |
| Calcined dolomite density | 1,540 | kg/m$^3$ |
| Mean catalyst particle size | 200 | μm |
| Mean dolomite particle size | 250 | μm |
| MgO content in dolomite | 40 | wt % |
| Inlet granular temperature of solid phases | 1x10$^5$ | m$^2$/s$^2$ |
| Packing limit of catalyst and sorbent phase | 0.60 | - |
| Restitution coefficient of all phase interactions | 0.90 | - |
| System properties | | |
| Outlet pressure | 1 | atm |
| Wall condition | Adiabatic* | |
| Shear condition | No slip | |

* Wall condition of top loop seal of regenerator reprocessed the experiment of Arstad *et al*. (2009, 2012) was set a temperature acting as a preheated zone.

### 3.3.1 Reforming riser design

This part consisted of simulations of SESMR/SESRE within only the reformer to find proper design and reaction parameters. The constraints and the goal used for determination were as follows:

1. No solid accumulation.
2. No tendency of long-term segregation between catalyst and sorbent.
3. $H_2$ purity of outlet gas reached the equilibrium which could be compared with experimental results in validations.
4. CaO conversion ($X_{CaO}$) in solid outlet not over 28%.
5. Highest $H_2$ flux out as possible.

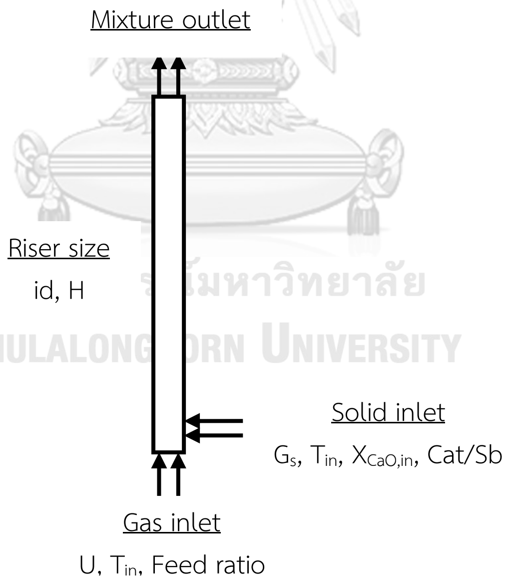

**Figure 3.4** Concerning parameters in the reformer design step.

Design parameters

1) Gas inlet velocity (U): To study

2) Solid flux ($G_s$): To study

3) Diameter of reformer (id): To study

4) Height of reformer (H): Chosen

Reaction parameters

1) Catalyst to sorbent ratio (Cat/Sb): To study

2) Feed ratio as

Steam to carbon ratio (S/C): Chosen

Steam to EtOH ratio (S/E): Chosen

3) Temperature of inlets ($T_{in}$): To study

4) CaO conversion of inlet sorbent ($X_{CaO,in}$): Chosen

From figure 3.4, there are a large number of parameters including the design parameters (sizes of reformer, gas velocity and solid flux) and the reaction parameters (reaction temperature, gas composition and solid composition). All of these parameters could mutually affect the performance of $H_2$. Because one-factor-at-a-time (OFAT) investigating would take lots of simulation cases to find the best case. A statistic method like $2^k$ full factorial design, which chose only 2 expected levels in each of k parameters, could make only $2^k$ different independent cases to investigate. The response variables i.e. $H_2$ flux and $H_2$ purity represented the performance of $H_2$ production. This method was also able to analyze significance of each single parameter and their interactions via analysis of variance (ANOVA) method. This method has linear assumption between the two experimental points because it is a screening method. Finally, the optimized case of SESMR/SESRE in the riser would be determined.

The computational domains of each riser configuration as shown in figure 3.5 were drawn by ANSYS® DesignModeler™ and its mesh was created by ANSYS® Meshing™. The uniform domains were chosen with 4 different cell sizes of mesh refinement.

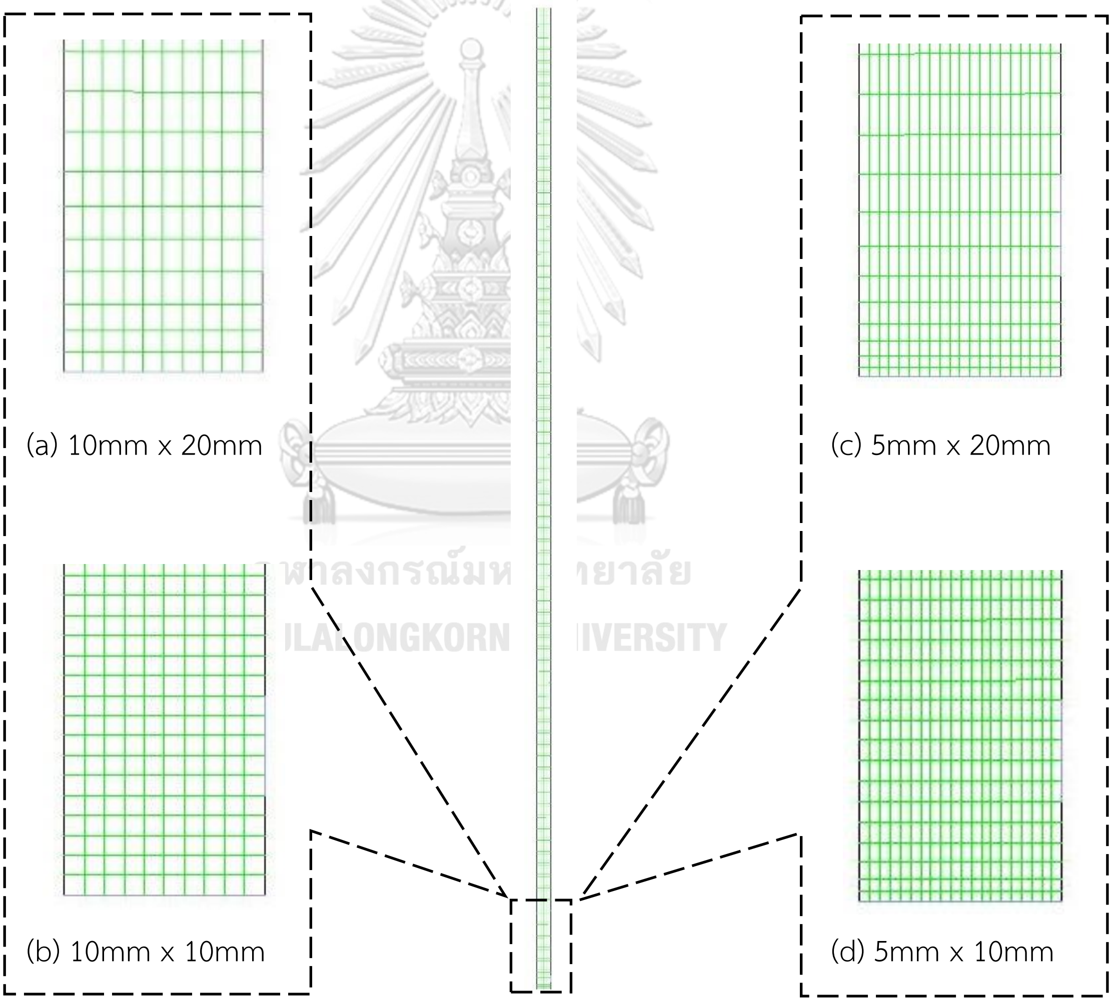

**Figure 3.5** The computational domains of the riser with different cell sizes.

The reforming operation was simulated using the time step of $1\text{x}10^{-3}$ s. At initial time, there was only inert $N_2$ in the domain. Then both fed gas and solid had entered through their inlet boundaries in normal direction. The calculated constant velocities and volume fraction were the inputs of each phase, but the inlet granular temperature was set for only solid phases. All feeds came in with the same temperature while the wall was adiabatic. The wall surface was set as no-slip condition. The product mixture discharges the riser to atmosphere.

### 3.3.2 Regenerator system design

Considering figure 3.6, after getting results from the designed risers, the most suitable values of the solid flux ($G_s$), the catalyst to sorbent ratio (Cat/Sb) and CaO conversion ($X_{CaO,in}$) of return solid were fixed in the regenerator design. Decarbonation kinetics was compiled in this part. The goal and the constraints were as follows:

1. No solid accumulation.
2. No tendency of long-term segregation between catalyst and sorbent.
3. Sufficient decarbonation (outlet $X_{CaO}$ should drop closely to 0%).

Design parameters

1) Gas inlet velocity (U): To study

2) Solid flux ($G_s$): Resulted from the riser

Reaction parameters

1) Catalyst to sorbent ratio (Cat/Sb): Resulted from the riser

2) Temperature of bed ($T_{bed}$): To study

3) CaO conversion of inlet sorbent ($X_{CaO,in}$): Resulted from the riser

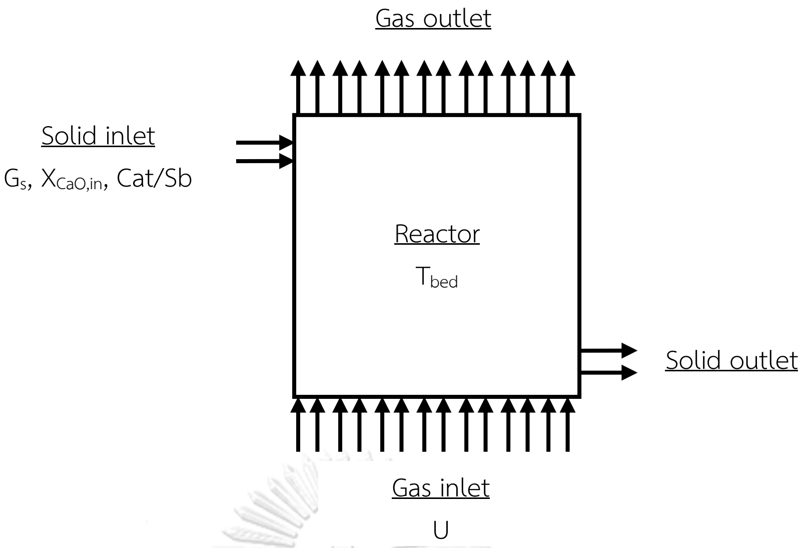

**Figure 3.6** Concerning parameters in the regenerator design step.

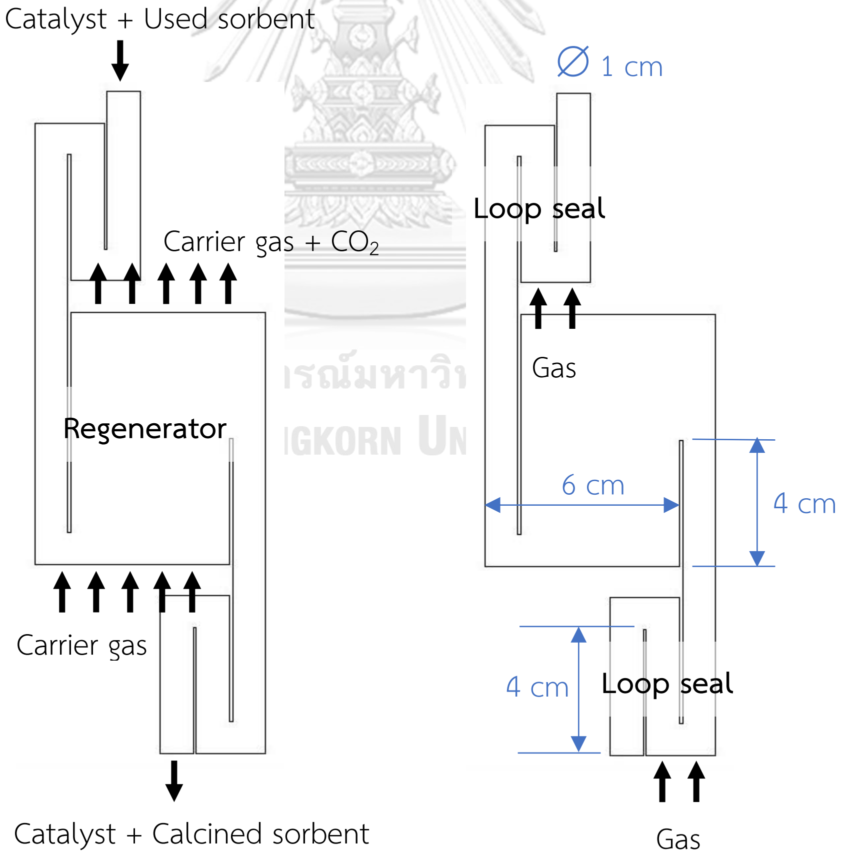

**Figure 3.7** The lab-scale regenerator reprocessed with experiment of Arstad *et al.* (2009, 2012).

In this part, the regenerator system design was divided into 2 steps as follows:

**Step 1. Design a regenerator in lab scale**: The system configuration in this step was modified from lab-scale circulating bubbling bed reactor of Arstad *et al*. (2009, 2012) as shown in figure 3.7. This regenerator included two loop seals which performed to prevent the gas inside the bubbling reactor pass through top and bottom channels. In this lab-scale regenerator, the top loop seal was also able to preheat solids before into the main reactor. The returning solids entered through the solid inlet in the top and the regenerated solids moved out of the regenerator in the bottom. In the experiment of Arstad *et al*. (2009, 2012), the carrier gas had inlet velocity of 0.056 m/s and the lifting gas in both loop seal had inlet velocity about 0.018 m/s. The bed in the reactor was controlled at 900°C. The simulation results in this step were also used for validation of the regeneration models with this experiment. Then the regenerator system would be modified, such as changing gas inlet velocity and/or design multi-stage of regenerator system, then scaling up to be matched with the designed risers.

**Step 2. Scale up and design an achieved system**: The regenerator scale would be matched with the size of the designed risers with the conditions of returning solid. In this step, one-factor-at-a-time (OFAT) was used for investigating remaining parameters i.e. the gas inlet velocity (U) and the temperature of bed ($T_{bed}$). The output of the regenerator system should satisfy the goal and constraints.

Similar with the riser part, the simulations in each step used the time step of $1x10^{-3}$ s. At initial time, there was only inert $N_2$ in the domain. The calculated constant velocities and volume fraction were the inputs of each phase. The walls in almost zone were defined adiabatic, except preheating in the top loop seal of lab-scale. All of the walls were assumed in no-slip condition.

# CHAPTER 4

# RESULTS AND DISCUSSION

## 4.1 Validations

There were two validations performed in this study i.e. cold flow validation and hot flow validations. In cold flow validation, chemical reactions were not involved in simulations. This validation was performed to test all chosen hydrodynamic models. In hot flow validations, the UDFs of kinetic rates of SESMR/SESRE/Decarbonation would be compiled into simulations to test the chosen kinetic models.

### 4.1.1 Cold flow validation

The cold flow validation compared the bed heights of bubbling bed to reference experiments of Lin *et al.* (1985) and simulation of Sánchez *et al.* (2012). The instantaneous contour of solid volume fraction and velocity vectors of solid at 10 s resulted from simulations at different gas velocities are shown in figure 4.1. At the lowest gas velocity (0.320 m/s), several small bubbles occurred and dispersed. When gas velocity was increased, some small bubbles collapsed into bigger bubbles and the bed was lifted higher. With much higher gas velocity (up to 0.892 m/s), the bubbles were much larger and more expanded the bed height. The time-averaged bed heights of the bed from these simulations, experiments of Lin *et al.* (1985) and simulations of Sánchez *et al.* (2012) are summarized in table 4.1. The results indicated that all of bed heights were very close.

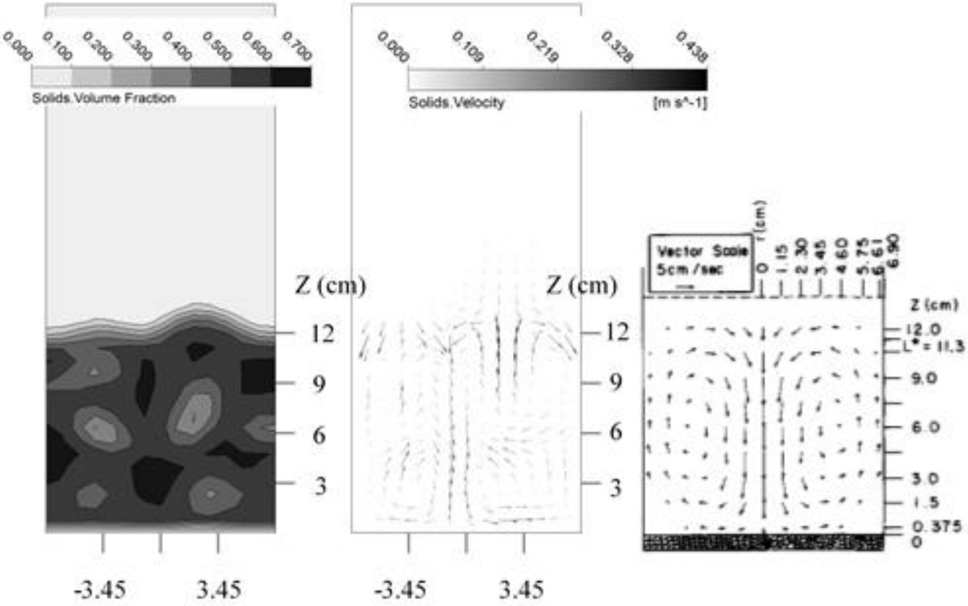

(a) U = 0.320 m/s

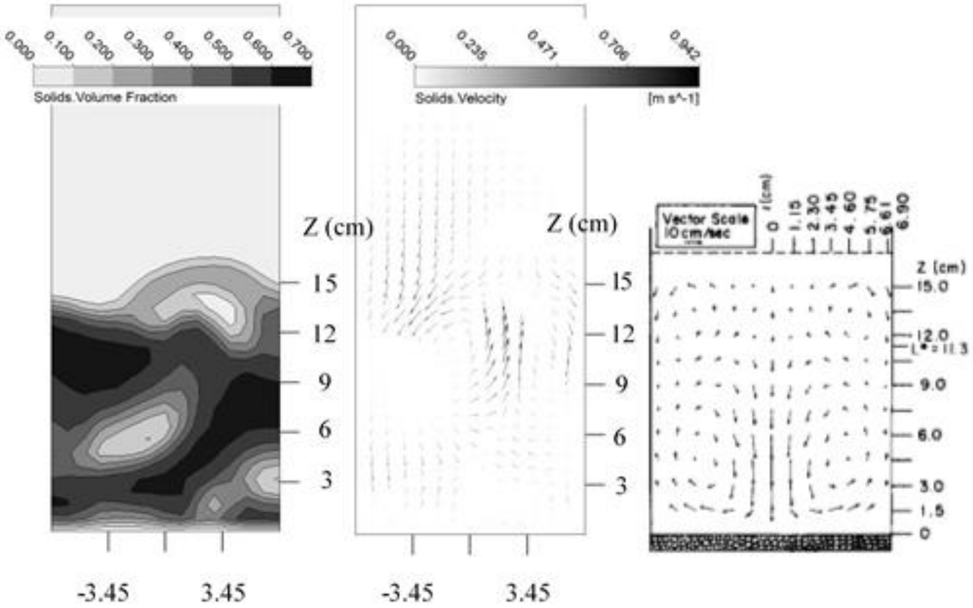

(b) U = 0.458 m/s

**Figure 4.1** The instantaneous solid volume fraction (left) and solid velocity (middle) of the bubbling bed reactor at 10 s relating to the experimental solid mean velocity (right) of Lin *et al*. (1985) with various gas velocities.

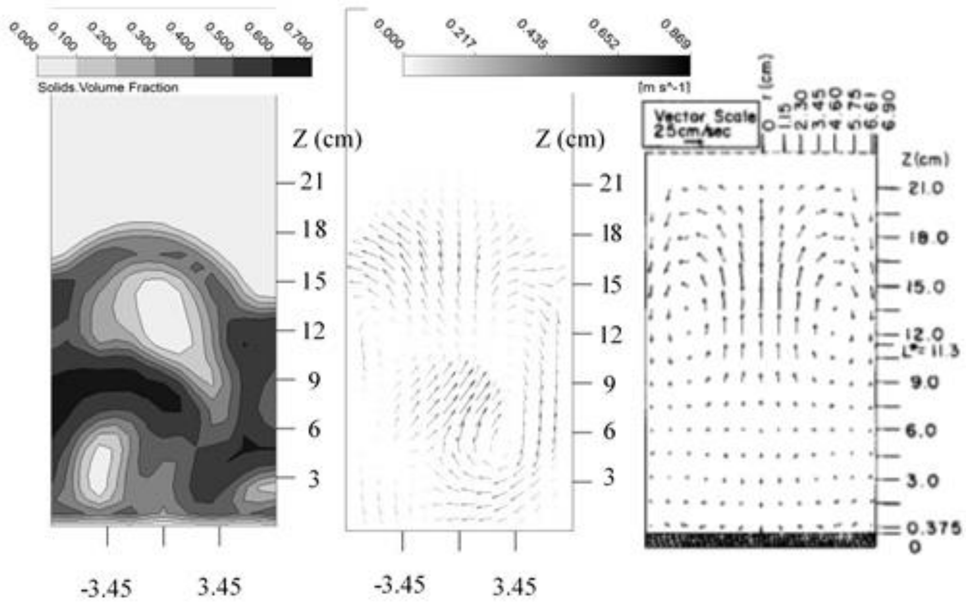

(c) U = 0.641 m/s

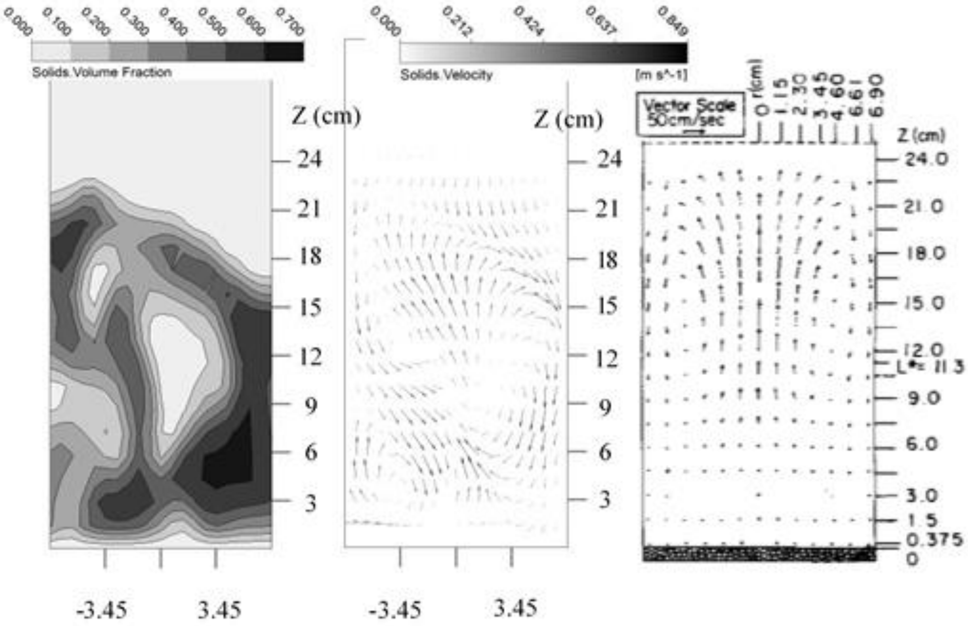

(d) U = 0.892 m/s

**Figure 4.1** (continued)

**Table 4.1** The comparison of time-averaged bed heights of cold flow validation with the experimental results of Lin *et al*. (1985) and the simulation results of Sánchez *et al*. (2012).

| | Bed height [m] | | |
|---|---|---|---|
| | Lin *et al*. | Sánchez *et al*. | This simulation |
| U = 0.320 m/s | 0.12 | 0.145 | 0.130 |
| U = 0.458 m/s | 0.15 | 0.16 | 0.155 |
| U = 0.641 m/s | 0.21 | 0.185 | 0.182 |
| U = 0.892 m/s | 0.23 | 0.225 | 0.234 |

### 4.1.2 SESMR validation

In SESMR validation, UDFs of SESMR kinetics were compiled to validate with experimental results from the bubbling bed reformer by Johnsen *et al.* (2006). This validation was separated into two cases, at first only SMR kinetics was compiled then additional carbonation kinetics was employed for SESMR in the other case. The comparison of simulation effluent gas compositions to experimental ones are shown in table 4.2. Most of them had good agreement with slight deviation. Different Ni content, different structure and different properties might affect the CO and $CO_2$ composition which were sensitive with WGS reaction.

**Table 4.2** The SMR and SESMR validation compared with experimental results of Johnsen *et al*. (2006).

| | | $H_2$ [% dry] | $CH_4$ [% dry] | CO [% dry] | $CO_2$ [% dry] |
|---|---|---|---|---|---|
| SMR | Johnsen *et al*. | 73.4 | 6.0 | 8.0 | 12.0 |
| | This simulation | 74.3 | 6.4 | 2.7 | 16.6 |
| SESMR | Johnsen *et al*. | 98.0 | 1.0 | 0.5 | 0.5 |
| | This simulation | 97.7 | 1.6 | 0.4 | 0.3 |

### 4.1.3 SESRE validation

Table 4.3 shows SRE/SESRE validations compared with experimental results and equilibrium reported in Olivas *et al.* (2014). There were two different kinetic models used for SRE i.e. model A which combined kinetics from Sun *et al.* (2005) and kinetics from Xu and Froment (1989), and model B which used kinetics from Mas *et al.* (2008). Next for SESRE, the carbonation kinetic model was compiled mutually with each SRE model. The results indicated that validations using model A had satisfied agreement with both experiments and equilibriums of both SRE and SESRE with only little deviations on CO which might because of different syntheses of the catalyst as well as similar case described in table 4.2. But when using model B, SRE validation had obviously differences on CO and $CO_2$. In addition, SESRE simulation using model B got gas compositions exactly similar to the compositions from the SRE simulation. There was little carbonation occurred at this operating condition. The serious deviations on CO, $CO_2$ compositions and $CO_2$ capture when using model B is because SRE kinetics of

Mas *et al.* (2008) did not involve WGS reaction that further converted CO to $CO_2$. Thus, the model A would be used for SRE kinetics in this study.

**Table 4.3** The SRE and SESRE validations compared with experimental results and equilibrium from Olivas *et al*. (2014).

| | | $H_2$ [% dry] | $CH_4$ [% dry] | CO [% dry] | $CO_2$ [% dry] | EtOH [% dry] |
|---|---|---|---|---|---|---|
| SRE | Olivas *et al*. | 64.7 | 0.7 | 4.6 | 30.0 | 0.0 |
| | Equilibrium | 69.6 | 3.3 | 8.3 | 18.7 | 0.0 |
| | Sim. using model A | 69.2 | 2.2 | 14.4 | 14.2 | 0.0 |
| | Sim. using model B | 62.5 | 4.2 | 33.3 | 0.1 | 0.0 |
| SESRE | Olivas *et al*. | 96.2 | 0.0 | 3.8 | 0.0 | 0.0 |
| | Equilibrium | 94.1 | 1.8 | 1.6 | 2.5 | 0.0 |
| | Sim. using model A | 98.5 | 0.5 | 0.6 | 0.4 | 0.0 |
| | Sim. using model B | 62.5 | 4.2 | 33.3 | 0.1 | 0.0 |

### 4.1.4 Decarbonation validation

For decarbonation validation, the experiment of Arstad *et al*. (2009, 2012) was reprocessed in a simulation using reported sorbent (natural dolomite) conversion in the bubbling bed reactor and in the loop seals as references. The CaO conversion of inlet sorbent was set equal to the reference value while the averaged CaO conversion of bed in the reactor and averaged CaO conversion at the outlet from the simulation was validated with sorbent conversion in the bed and in bottom loop seal, respectively. Because in the experiment, temperature of the bed could be controlled in the furnace but in this simulation, the top loop seal was set as preheater through the temperature-adjusted wall for controlling the bed temperature instead. After trials until the averaged and steady temperature of the bed equaled to exact 900°C of the experiment, the simulated CaO conversion are shown in table 4.4. There was slight deviations occurred so the decarbonation kinetics of Okunev *et al.* (2008) was acceptable for further simulations.

**Table 4.4** The CaO conversion of sorbent in the regenerator validated with experimental results of Arstad *et al*. (2012).

| | $X_{CaO}$ [%] | | |
|---|---|---|---|
| | Inlet | In the bed | Outlet |
| Arstad *et al*. | 15.27 | 4.15 | 3.05 |
| This study | 15.27 | 5.05 | 3.39 |

## 4.2 SESMR performance in the riser

### 4.2.1 Time average and mesh refinement of the SESMR reformer

Because instantaneous flow of each particle and amount of each substance have fluctuated within fluidized bed reactors, thus, time-dependent simulation had to be performed rather than steady-state simulation. A quasi-steady state value from selected time-averaged range was used to represent the result. The riser with diameter of 0.1 m operating with inlet temperature of 600°C, catalyst to sorbent ratio of 0.16, gas velocity of 6 m/s and 200 kg/m$^2$s solid flux, $H_2$ flux out of the riser at every 0.1 s was plotted as an example case in figure 4.2. The results showed that the fluctuation of $H_2$ flux seemed stable after approximately 5 s as well as in other cases. Thus, a time-averaged range of 10–20 s would be used to represent further simulation results in this study.

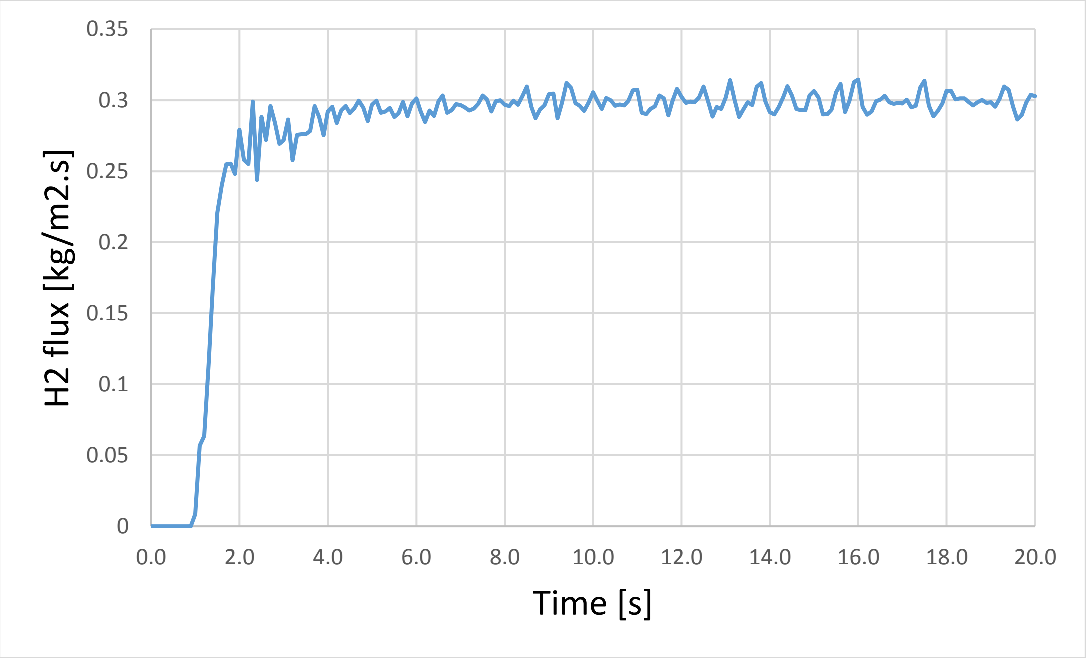

**Figure 4.2** The $H_2$ flux out of the SESMR riser as a function of time in case of id = 0.1 m, $T_{in}$ = 600°C, Cat/Sb = 0.16, U = 6 m/s and $G_s$ = 200 $kg/m^2s$.

Next to investigate the mesh refinement, the same example cases were performed and time-averaged axial profiles of $H_2$ flux with different sizes of cell ($\Delta x \cdot \Delta y$) were displayed as shown in figure 4.3. The results showed that the 10 mm·20mm size was insufficiently fine while the 5mm·10mm size took more unnecessary calculating time. Although the 5mm·20mm size and the 10mm·10mm size had equivalent the numbers of cells but the 5mm·20mm size was chosen for further simulation because in the riser, radial profile had more effects than the axial profile.

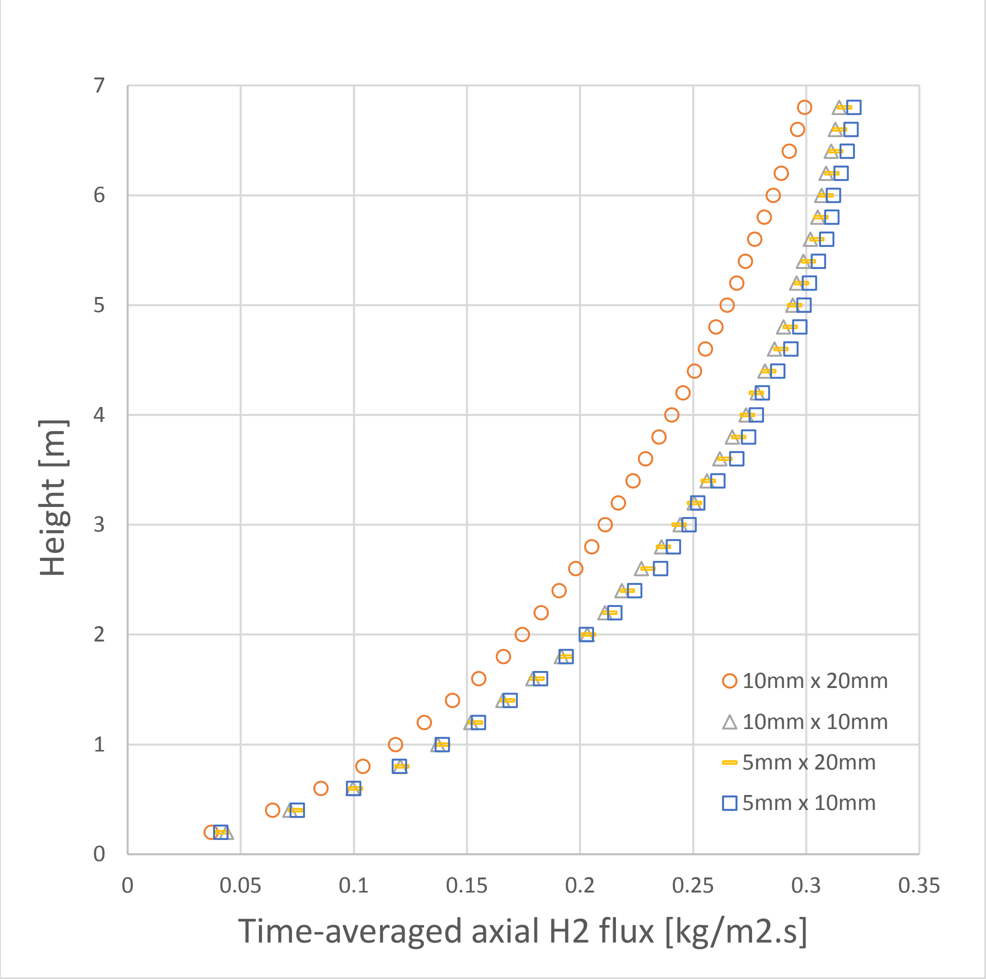

**Figure 4.3** The time-averaged axial profiles of $H_2$ flux out of the SESMR riser with different cell sizes in case of id = 0.1 m, $T_{in}$ = 600°C, Cat/Sb = 0.16, U = 6 m/s and $G_s$ = 200 kg/$m^2$s.

### 4.2.2 Parametric analysis for SESMR operation

From all concerning parameters in figure 3.4, only five parameters of the system including the gas inlet velocity, the solid flux, the diameter of riser, the catalyst to sorbent ratio and the temperature of inlets were explored with $2^5$ factorial design. Two levels of these parameters and the fixed value of other parameters are shown in table 4.5.

**Table 4.5** The parameters chosen in the $2^5$ full factorial design of the SESMR riser.

| Parameters | Value | |
|---|---|---|
| Design parameters | | |
| Gas inlet velocity (U) | 4 and 6 | m/s |
| Solid flux ($G_s$) | 50 and 200 | kg/m$^2$s |
| Diameter of the riser (id) | 0.05 and 0.2 | m |
| Height of the riser (H) | 7 (Chosen) | m |
| Reaction parameters | | |
| Catalyst to sorbent ratio (Cat/Sb) | 0.16 and 2.54 | kg/kg |
| Steam to carbon (S/C) | 4 (Chosen) | mol/mol |
| Temperature of inlets ($T_{in}$) | 575 and 665 | °C |
| CaO conversion of inlet sorbent ($X_{CaO,in}$) | 0 (Chosen) | % |

Next to analyze $2^5$ factorial design results from all 32 runs, the area average near the outlet with the time average of 10-20 s was used to report values of each $H_2$ flux, $H_2$ purity and others, e.g. CaO conversion, as shown in table 4.6. The $H_2$ flux and the $H_2$ purity, which both represented $H_2$ production performance, were response variables of 32 runs of the factorial design. As previously described constraint, Johnsen *et al.* (2006) specified that the limitation of using dolomite as the sorbent in CFBR was losing CaO capacity in long term re-usage until the CaO conversion could not be over 28% steadily. In every run, none of CaO conversion reached 28%, thus the limitation of CaO capacity was not needed to be concerned and long-term circulating of the dolomite was feasible in ranges of this studied system. The other results showed that there was no run which get the maximum $H_2$ flux together with the maximum $H_2$ purity, thus both needed further statistical analysis like the ANOVA for determining the best practice and sensitivity analyses. The riser diameter (id), the inlet temperature ($T_{in}$), the catalyst to sorbent ratio (Cat/Sb), the solid flux ($G_s$), the gas velocity (U), the $H_2$ flux and the $H_2$ purity were coded as A, B, C, D, E, R1 and R2, respectively, in the ANOVA.

**Table 4.6** The area-averaged $H_2$ flux, $H_2$ purity and CaO conversion ($X_{CaO}$) at the outlet of the SESMR riser from parametric study with the $2^5$ factorial design.

| Factor: | A | B | C | D | E | R1 | R2 | |
|---|---|---|---|---|---|---|---|---|
| Run | id [m] | $T_{in}$ [°C] | Cat/Sb [kg/kg] | $G_s$ [kg/m$^2$s] | U [m/s] | $H_2$ flux [kg/m$^2$s] | $H_2$ purity [% dry] | $X_{CaO}$ [%] |
| 1 | 0.05 | 575 | 2.54 | 50 | 4 | 0.172422 | 93.90 | 12.70 |
| 2 | 0.05 | 575 | 2.54 | 50 | 6 | 0.189089 | 79.71 | 10.04 |
| 3 | 0.05 | 575 | 2.54 | 200 | 4 | 0.197854 | 98.36 | 4.01 |
| 4 | 0.05 | 575 | 2.54 | 200 | 6 | 0.267603 | 94.86 | 5.28 |
| 5 | 0.05 | 575 | 0.16 | 50 | 4 | 0.13552 | 89.73 | 3.37 |
| 6 | 0.05 | 575 | 0.16 | 50 | 6 | 0.109459 | 70.37 | 2.55 |
| 7 | 0.05 | 575 | 0.16 | 200 | 4 | 0.178654 | 96.43 | 1.25 |
| 8 | 0.05 | 575 | 0.16 | 200 | 6 | 0.21108 | 90.63 | 1.41 |
| 9 | 0.05 | 665 | 2.54 | 50 | 4 | 0.201309 | 96.80 | 14.94 |
| 10 | 0.05 | 665 | 2.54 | 50 | 6 | 0.258555 | 88.17 | 14.92 |
| 11 | 0.05 | 665 | 2.54 | 200 | 4 | 0.206029 | 97.67 | 3.89 |
| 12 | 0.05 | 665 | 2.54 | 200 | 6 | 0.303812 | 96.56 | 5.85 |
| 13 | 0.05 | 665 | 0.16 | 50 | 4 | 0.176828 | 94.66 | 4.38 |
| 14 | 0.05 | 665 | 0.16 | 50 | 6 | 0.177717 | 82.56 | 4.04 |
| 15 | 0.05 | 665 | 0.16 | 200 | 4 | 0.201382 | 97.34 | 1.33 |
| 16 | 0.05 | 665 | 0.16 | 200 | 6 | 0.272869 | 95.03 | 1.77 |
| 17 | 0.2 | 575 | 2.54 | 50 | 4 | 0.200761 | 98.60 | 4.02 |
| 18 | 0.2 | 575 | 2.54 | 50 | 6 | 0.27316 | 95.32 | 5.32 |
| 19 | 0.2 | 575 | 2.54 | 200 | 4 | 0.204256 | 99.17 | 1.07 |
| 20 | 0.2 | 575 | 2.54 | 200 | 6 | 0.297392 | 98.37 | 1.50 |

**Table 4.6** (continued)

| Factor: | **A** | **B** | **C** | **D** | **E** | **R1** | **R2** | |
|---|---|---|---|---|---|---|---|---|
| Run | id [m] | $T_{in}$ [°C] | Cat/Sb [kg/kg] | $G_s$ [kg/m$^2$s] | U [m/s] | $H_2$ flux [kg/m$^2$s] | $H_2$ purity [% dry] | $X_{CaO}$ [%] |
| 21 | 0.2 | 575 | 0.16 | 50 | 4 | 0.190798 | 97.47 | 1.27 |
| 22 | 0.2 | 575 | 0.16 | 50 | 6 | 0.216396 | 91.04 | 1.45 |
| 23 | 0.2 | 575 | 0.16 | 200 | 4 | 0.203383 | 99.10 | 0.34 |
| 24 | 0.2 | 575 | 0.16 | 200 | 6 | 0.279256 | 97.48 | 0.43 |
| 25 | 0.2 | 665 | 2.54 | 50 | 4 | 0.206551 | 97.72 | 3.92 |
| 26 | 0.2 | 665 | 2.54 | 50 | 6 | 0.305924 | 96.93 | 5.50 |
| 27 | 0.2 | 665 | 2.54 | 200 | 4 | 0.203183 | 96.08 | 0.92 |
| 28 | 0.2 | 665 | 2.54 | 200 | 6 | 0.297275 | 91.89 | 1.08 |
| 29 | 0.2 | 665 | 0.16 | 50 | 4 | 0.202109 | 96.36 | 1.19 |
| 30 | 0.2 | 665 | 0.16 | 50 | 6 | 0.276525 | 95.26 | 1.71 |
| 31 | 0.2 | 665 | 0.16 | 200 | 4 | 0.205234 | 97.51 | 0.31 |
| 32 | 0.2 | 665 | 0.16 | 200 | 6 | 0.300787 | 95.98 | 0.40 |

In the ANOVA, any main effect or interaction which significantly affected the $H_2$ flux or the $H_2$ purity had to have P-value less than 0.05 (Montgomery, 2012). The ANOVA results of both the $H_2$ flux and the $H_2$ purity are shown in tables 4.7 and 4.8, respectively. The main effects and their interactions in significant order were descending sorted by obvious to the p-values. Furthermore, regression models for prediction the $H_2$ flux and the $H_2$ purity were determined as eqs. 4.1 and 4.2, respectively.

$$H_2 \text{ flux} = 0.222599 + 0.019A + 0.015B + 0.014C + 0.017D + 0.030E + 0.00970AE + 0.00967DE \qquad (4.1)$$

$$H_2 \text{ purity} = 93.97 + 2.55A + 1.04C + 2.43D - 2.71E - 1.36AB - 2.00AD + 1.48AE - 1.21BD + 1.41DE - 1.19ADE \quad (4.2)$$

where A, B, C, D and E in the regression models were coded variables which transformed low to high levels of considered parameters into -1 to +1 range.

**Table 4.7** The results of the ANOVA of the $H_2$ flux out of the SESMR riser.

| Source | Sum of squares | Degree of freedom (DF) | Mean square | F-value | P-value |
|---|---|---|---|---|---|
| E (U) | 0.028240 | 1 | 0.028240 | 51.39508 | <0.0001 |
| A (id) | 0.011356 | 1 | 0.011356 | 20.66646 | 0.000132 |
| D ($G_s$) | 0.009009 | 1 | 0.009009 | 16.39574 | 0.000465 |
| B ($T_{in}$) | 0.006874 | 1 | 0.006874 | 12.51014 | 0.001681 |
| C (Cat/Sb) | 0.006249 | 1 | 0.006249 | 11.37263 | 0.002523 |
| AE | 0.003008 | 1 | 0.003008 | 5.474424 | 0.027946 |
| DE | 0.002995 | 1 | 0.002995 | 5.450380 | 0.028259 |
| Residual | 0.013187 | 24 | 0.000549 | | |
| Cor Total | 0.080918 | 31 | | | |

The P-values from both the tables and the coefficients in the both regression models indicated that most top-three significant main effects/interactions on both the $H_2$ flux and the $H_2$ purity were the same, i.e. the gas velocity (E), the riser diameter (A) and the solid flux (D) in descending order. The next descending significant main effects/interactions were different between on the $H_2$ flux and on the $H_2$ purity. The inlet temperature (B) significantly affected only the $H_2$ flux but its interactions (AB and BD) occurred significant to the $H_2$ purity. On overall $H_2$ production performance, the design parameters including the gas velocity (E), the riser diameter (A) and the solid flux (D), in descending order, had more effect than the reaction parameters including the inlet temperature (B) and the catalyst to sorbent ratio (C).

**Table 4.8** The results of the ANOVA of the $H_2$ purity out of the SESMR riser.

| Source | Sum of squares | Degree of freedom (DF) | Mean square | F-value | P-value |
|---|---|---|---|---|---|
| E (U) | 235.0490 | 1 | 235.0490 | 39.22010 | <0.0001 |
| A (id) | 207.6093 | 1 | 207.6093 | 34.64154 | <0.0001 |
| D ($G_s$) | 189.5516 | 1 | 189.5516 | 31.62844 | <0.0001 |
| AD | 128.5148 | 1 | 128.5148 | 21.44388 | 0.000144 |
| AE | 69.79685 | 1 | 69.79685 | 11.64625 | 0.002619 |
| DE | 63.32517 | 1 | 63.32517 | 10.56639 | 0.003826 |
| AB | 59.46191 | 1 | 59.46191 | 9.921771 | 0.004833 |
| BD | 46.79862 | 1 | 46.79862 | 7.808784 | 0.010865 |
| ADE | 45.29247 | 1 | 45.29247 | 7.557468 | 0.012023 |
| C (Cat/Sb) | 34.34780 | 1 | 34.34780 | 5.731249 | 0.026079 |
| Residual | 125.8546 | 21 | 5.993074 | | |
| Cor Total | 1205.602 | 31 | | | |

Next for the sensitivity analyses, the main effects and interactions on the $H_2$ flux and the $H_2$ purity were plotted as shown in figures 4.4 and 4.5, respectively. The slopes showed either positive or negative effects on the response variable and the steepness of slope could indicate the significant order like the P-value and the regression coefficients. In case that the $H_2$ flux was the response variable in figure 4.4a, all of the main effects were positive as well as their coefficients in the regression model. Among these main effects, the slope of the gas velocity (E) was obviously the steepest, following by the riser diameter (A), the solid flux (D), the inlet temperature

(B) and the catalyst to sorbent ratio (C), in descending order. The positive effect of the gas velocity (E) described that increasing of the gas velocity made feed increased despite the residence time must be less. But for the rapid reaction like SESMR, the reaction had sufficient time to produce more $H_2$. In case of the riser diameter (A), the larger diameter get more $H_2$ flux because the bigger area of gas inlet made the feed increased as well, even though the dilute region of solid might be wider. Comparison of the solid flux (D) indicated that the low flux (50 kg/$m^2$s) was insufficient contact between gas (reactant) and solid (catalyst/sorbent). Lastly, both of the inlet temperature (B) and the catalyst to sorbent ratio (C) prefer the high level (665°C and 2.54 kg/kg, respectively) comparing to the low levels.

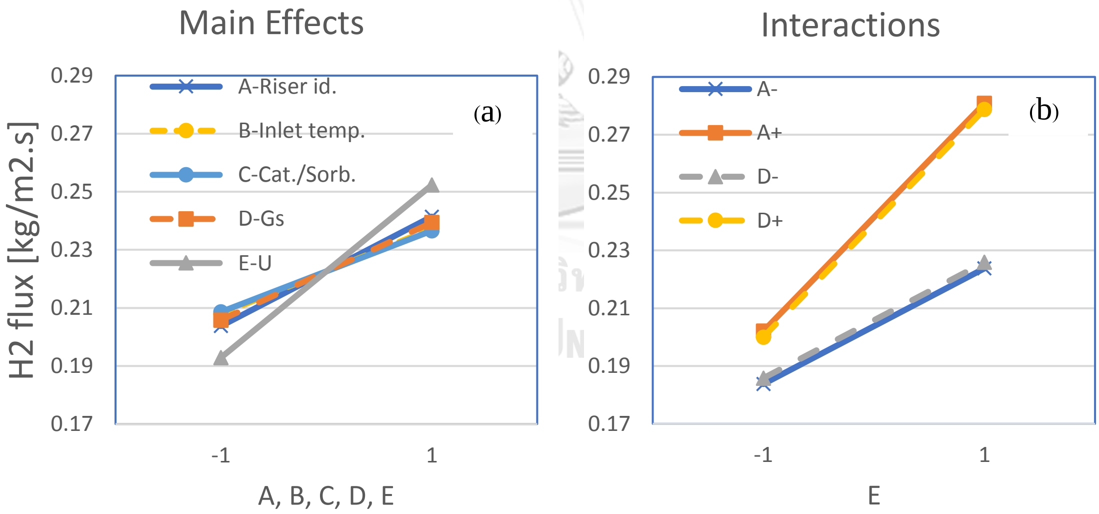

**Figure 4.4** The main effects and the interactions on the $H_2$ flux out of the SESMR riser.

From the interaction effects on the $H_2$ flux as plotted in figure 4.4b, when the gas velocity (E) was operated with the low riser diameter (A-) or the low solid flux (D-), the slopes had the same direction as the main effect (E) but were slightly less steep. On the other hand, when the gas velocity (E) was operated with the high riser diameter (A+) or the high solid flux (D+), the slopes had the same direction as the main effect (E) but were slightly steeper. Because all of the main effects (E, A and D) were positive, thus their interactions (AE and DE) were more positive to the $H_2$ flux. The high gas velocity interacted with the high riser diameter (A+E+) get higher $H_2$ flux because they both made more feed mutually. However, the little changes of the steepness indicated that the interactions (AE and DE) were less effective than the main effect (E) and corresponding to their P-values in table 4.7 and regression coefficients in eq. 4.1.

In figure 4.5a, the riser diameter (A), the solid flux (D) and the catalyst to sorbent ratio (C) had positive effects on the $H_2$ purity as well as $H_2$ flux. This meant that at the high levels of these parameters (id = 0.2 m, $G_s$ = 200 kg/m$^2$s and Cat/Sb = 2.54 kg/kg), contact of gas-solid (reactant-catalyst/sorbent) was better than at the low levels. Only the gas velocity (E) had negative effect on the $H_2$ purity which was opposed to the $H_2$ flux. This is because the higher gas velocity (6 m/s) made more feed but the residence time was less and insufficient to reach SESMR equilibrium.

When the gas velocity (E) was operated with the low riser diameter (A-) or the low solid flux (D-) in figure 4.5b, the slopes of the $H_2$ purity had the same negative direction as the main effect (E) but were slightly steeper. Whereas when the gas velocity (E) was operated with the high riser diameter (A+) or the high solid flux (D+), the slopes had the same negative direction as the main effect (E) but were slightly less steep. This meant that even though the higher riser diameter or the higher solid flux made better contact of gas-solid enhancing the $H_2$ purity, the less residence time with the higher gas velocity still had more effect to lower the $H_2$ purity. This was consistent to ANOVA (table 4.8) which the gas velocity (E) was much more significant (higher P-value) than their interaction (AE and DE).

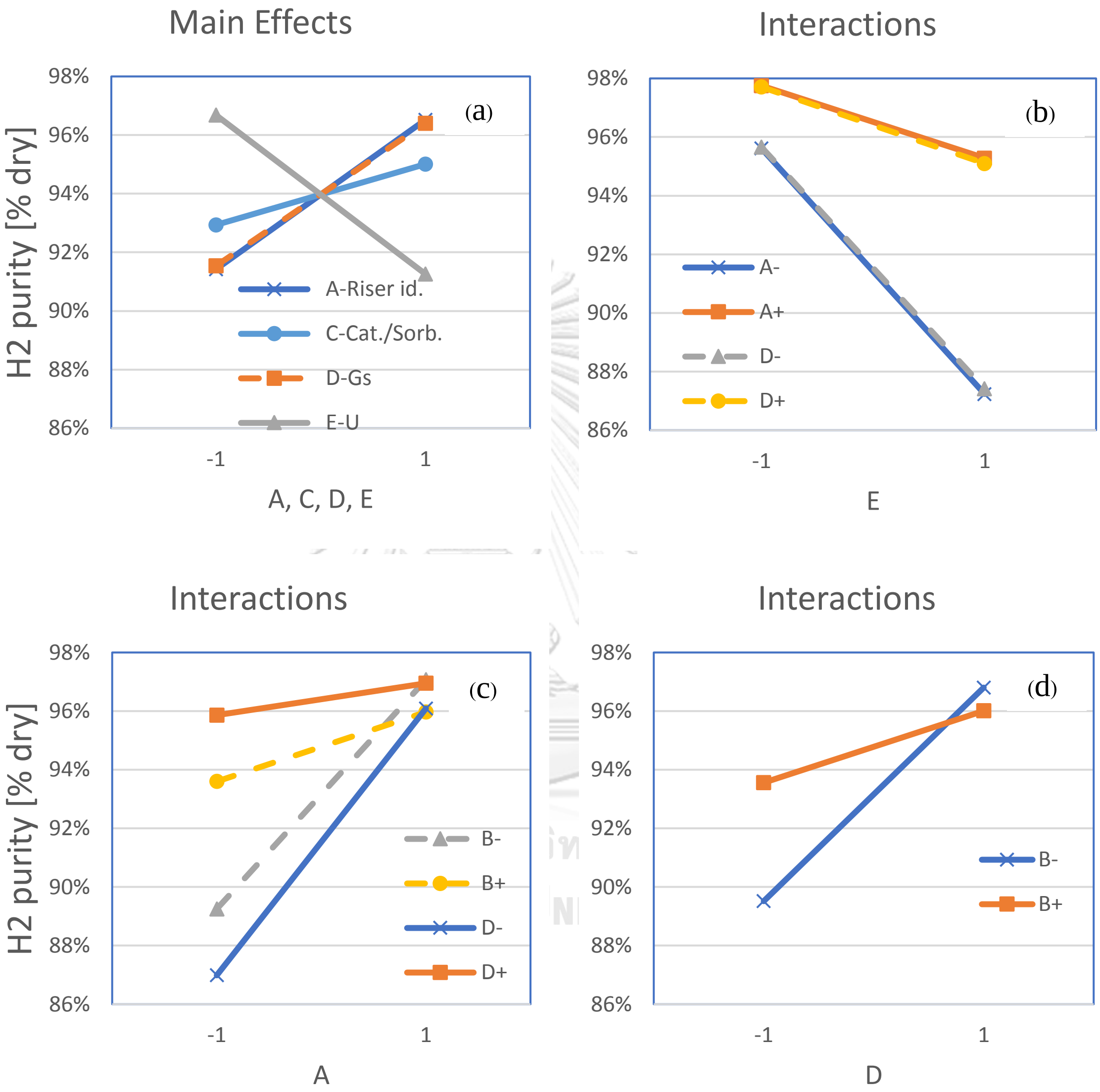

**Figure 4.5** The main effects and the interactions on the $H_2$ purity out of the SESMR riser.

Similarly in figure 4.5c, when the riser diameter (A) was operated with the inlet temperature (B) or the solid flux (D), the slopes were the same in positive direction as the main effect (A) and slightly steeper at the low level (B- and D-) but slightly less steep at the high level (B+ and D+). As well as in figure 4.5d, when the solid flux (D) interacted with the inlet temperature (B), the slopes showed the same in positive direction as the main effect (D) with being slightly steeper at the low inlet temperature (B-) but being slightly less steep at the high inlet temperature (B+).

Lastly, from all of the interaction plots in figure 4.5, the little changes of the steepness of the interactions (AE, DE, AB, AD and BD) indicated that these interactions were less effective than the main effects (A, D and E) consistent with their P-values in table 4.8 and regression coefficients in eq. 4.2.

**Table 4.9** The optimum $H_2$ flux and $H_2$ purity out of the SESMR riser predicted from the regression models and a simulation.

| Factor: | A | B | C | D | E | R1 | R2 | |
|---|---|---|---|---|---|---|---|---|
| | id [m] | $T_{in}$ [°C] | Cat/Sb [kg/kg] | $G_s$ [kg/m$^2$s] | U [m/s] | $H_2$ flux [kg/m$^2$s] | $H_2$ purity [% dry] | $X_{CaO}$ [%] |
| Optimizing R2 prior to R1 | 0.200 | 581.48 | 2.540 | 199.98 | 6.00 | 0.308708 | 99.17 | |
| Optimizing R1 prior to R2 | 0.200 | 581.40 | 2.540 | 199.82 | 6.00 | 0.308523 | 99.17 | |
| Simulation (Run 33) | 0.200 | 581.00 | 2.540 | 200.00 | 6.00 | 0.300574 | 98.58 | 1.48 |

Table 4.9 shows the optimized results of the regression models of the $H_2$ flux and the $H_2$ purity. Either the $H_2$ purity or the $H_2$ flux was optimized prior to the another, the predicted $H_2$ purity was maximum at 99.17% in dry basis and the $H_2$ flux reached 0.309 kg/m$^2$s in the riser with 0.2 m diameter, the inlet temperature of 581°C, the catalyst to sorbent ratio of 2.54 kg/kg, the solid flux of 200 kg/m$^2$s and the gas velocity

of 6 m/s. To confirm the results from the prediction, another case with those values of parameters was simulated as run 33. The $H_2$ purity and the $H_2$ flux from the simulation were 98.58% in dry basis and 0.301 kg/m$^2$s, respectively, which both agreed very well with the results from the prediction.

### 4.2.3 Hydrodynamics of SESMR in the riser

First of all, an optimum case would be visually analyzed. The instantaneous contour plots of volume fraction of solid phases (catalyst and sorbent) and gas phase at 20 s of run no. 33 are displayed in figure 4.6. The gradient shades of colors from blue to red represent low volume fraction to high volume fraction of each phases. The contour plots show that both the catalyst and the sorbent phases were denser near the wall all along the height of the riser while the volume fraction of gas phase was dense in the center line of the riser. These volume fraction contour plots confirmed that the fast fluidization occurred in the riser. The similarity of volume fraction of the catalyst phase and the sorbent phase indicated very good mixing of the catalyst and the sorbent, thus SESMR could performed very well in this CFB riser.

Figure 4.7 displays the instantaneous contour plots of mole fraction of $H_2$, $CH_4$ and $CO_2$ in the gas phase at 20 s in the same case of run no. 33. The contour plots show the development of $H_2$ produced along the height of the riser. In this case, $H_2$ fraction reached in equilibrium, $CH_4$ was fully converted as well as $CO_2$ was fully adsorbed before exiting the riser. Area-averaged fractions of $H_2$ and $H_2O$ near the outlet were 0.6453 and 0.3554, respectively, and the little remaining fraction was the other gases such as 0.0062 of $CH_4$ and 0.0030 of $CO_2$. This fraction of $H_2$ equaled to $H_2$ purity of 98.58% in dry basis.

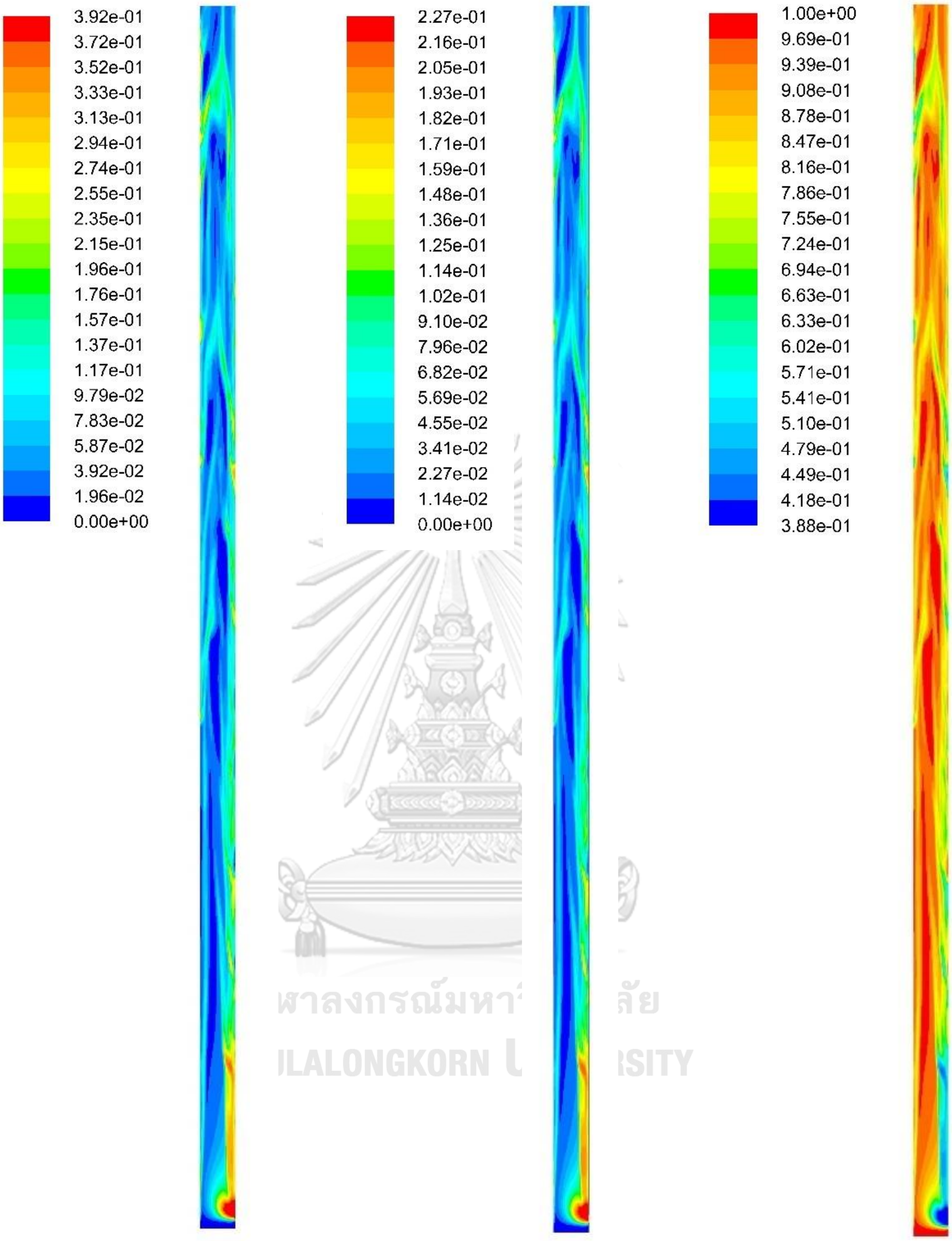

(a) Catalyst (b) Sorbent (c) Gas

**Figure 4.6** The instantaneous volume fraction of each phase in the SESMR riser at 20 s in the best performance case (run 33).

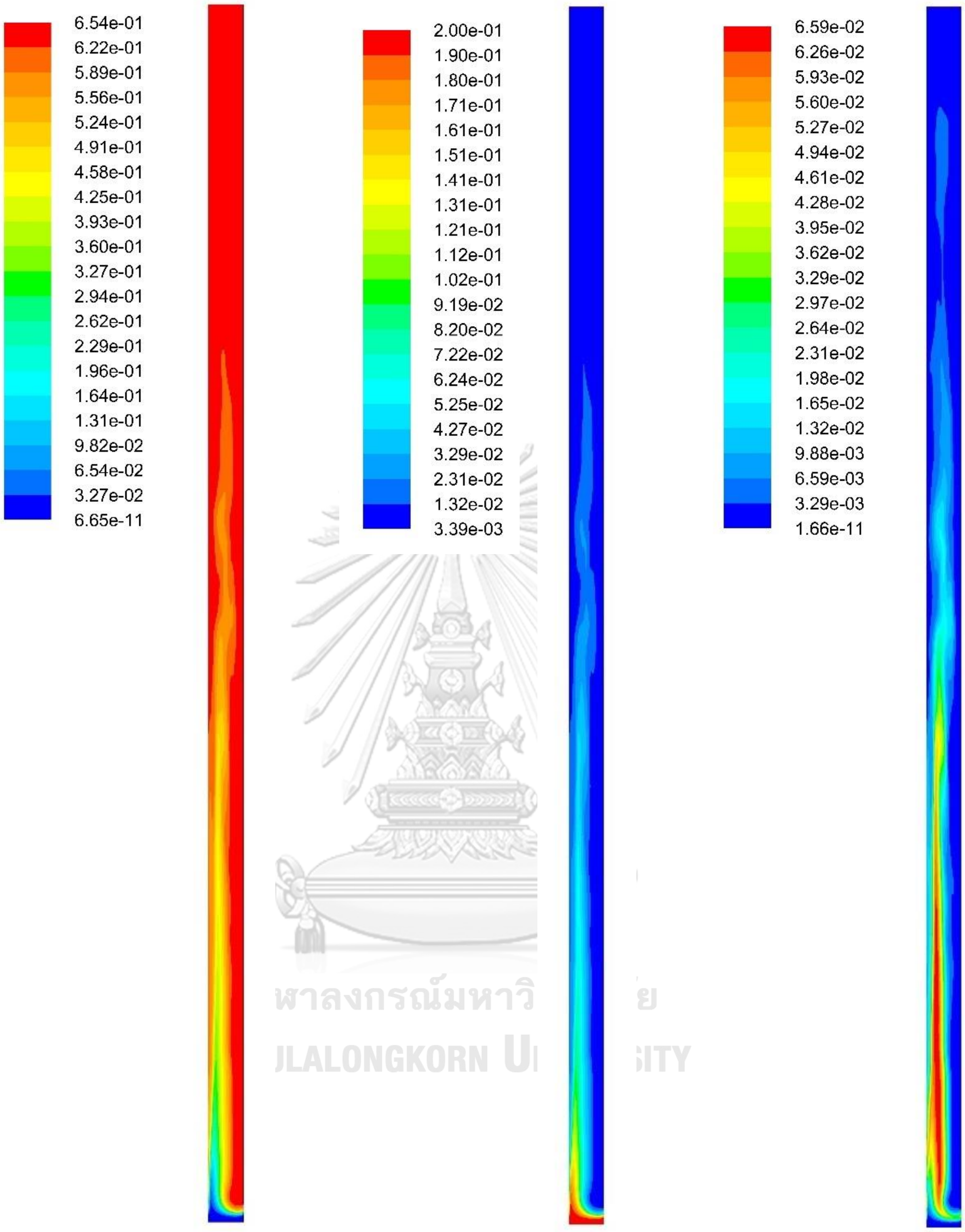

(a) $H_2$ (b) $CH_4$ (c) $CO_2$

**Figure 4.7** The instantaneous mole fraction (wet basis) of $H_2$, $CH_4$ and $CO_2$ in gas phase of the SESMR riser at 20 s in the best performance case (run 33).

Next, the instantaneous contour plots of temperature of each phase at the same time and the same run are shown in figure 4.8. The temperature contours of all phase looked similar with slight deviation from the inlet temperature of 854 K. The decreaseing of the temperature (to 840 K minimum) was caused by highly endothermic of SMR but the increasing of the temperature (to 863 K maximum), which obviously occurred in lower half of the core in sorbent phase, was caused by exothermic of carbonation. In balance of SESMR, especially at the right wall since the entrance of solids, the temperature of each phase was constant about 856-857 K which rarely changed from the inlet temperature. Whereas at the left side of the wall, the temperature of each phase gradually increased along the height of the riser in accordance with the increasing of $H_2$ and the decreasing of $CH_4$ and $CO_2$ as shown in figure 4.7. These indicated that the carbonation, which was slower reaction than SMR, proceeded gradually in the left side until all gases reached in equilibrium before leaving the riser.

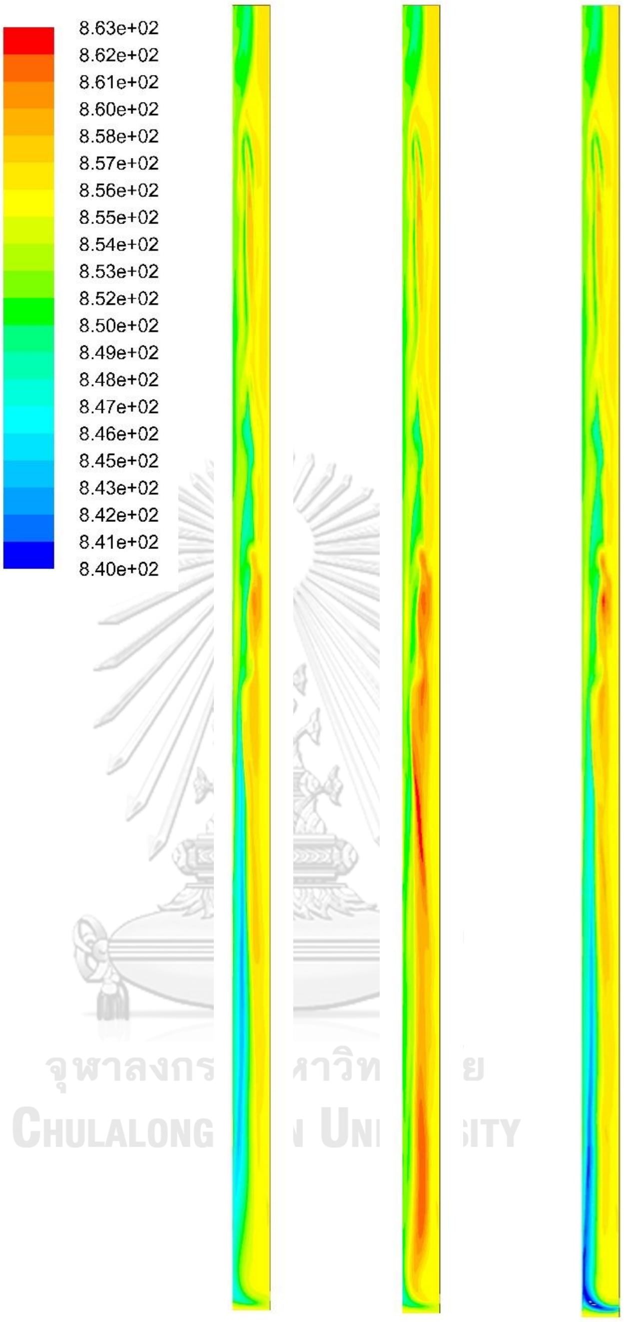

(a) Catalyst (b) Sorbent (c) Gas

**Figure 4.8** The instantaneous temperature (in Kelvin) of each phase in the SESRE riser at 20 s for the best performance case (run 33).

In this part, the catalyst and sorbent distributions along axial and radial direction were expected key hydrodynamics which explained how SESMR performed well in this riser system. Inside the riser of the optimum case (run 33), the volume fraction of both catalyst and sorbent phase, volumetric catalyst to sorbent ratio were compared to the $H_2$ flux and the $H_2$ purity.

In figure 4.9, the time-averaged of the $H_2$ flux in axial direction was plotted from 0.1 m height which was the exact height above the solid inlet channel. The $H_2$ flux accumulated rapidly in the lower height and reached steady in the upper height near the outlet (7 m). Figure 4.10 shows the time-averaged radial distributions of the $H_2$ purity at different heights. Radial distance at 0.0 m was the position of left wall and at 0.2 m was the position of right wall where solid inlet was on this right side at 0.05-0.1 m height. At above solid inlet (0.1 m height), the $H_2$ purity suddenly approached equilibrium at the solid inlet (0.2 m distance). The $H_2$ purity decreased along to left direction far from the solid inlet but was higher at the left wall. At higher height, the $H_2$ purity profile was rapidly higher even in the middle distance. Until over 5.0 m height, the $H_2$ purity profiles approached the equilibrium and were quite steady and uniform along the radial distance.

From both figures 4.9 and 4.10, these profiles could explain that SESMR was extremely rapid. It approached equilibrium since solid (catalyst/sorbent) had started to contact the gas (reactant) at the inlet. In this system of run 33, SESMR could be close to complete since 5.0 m height thus the 7 m height of the riser was sufficient to design.

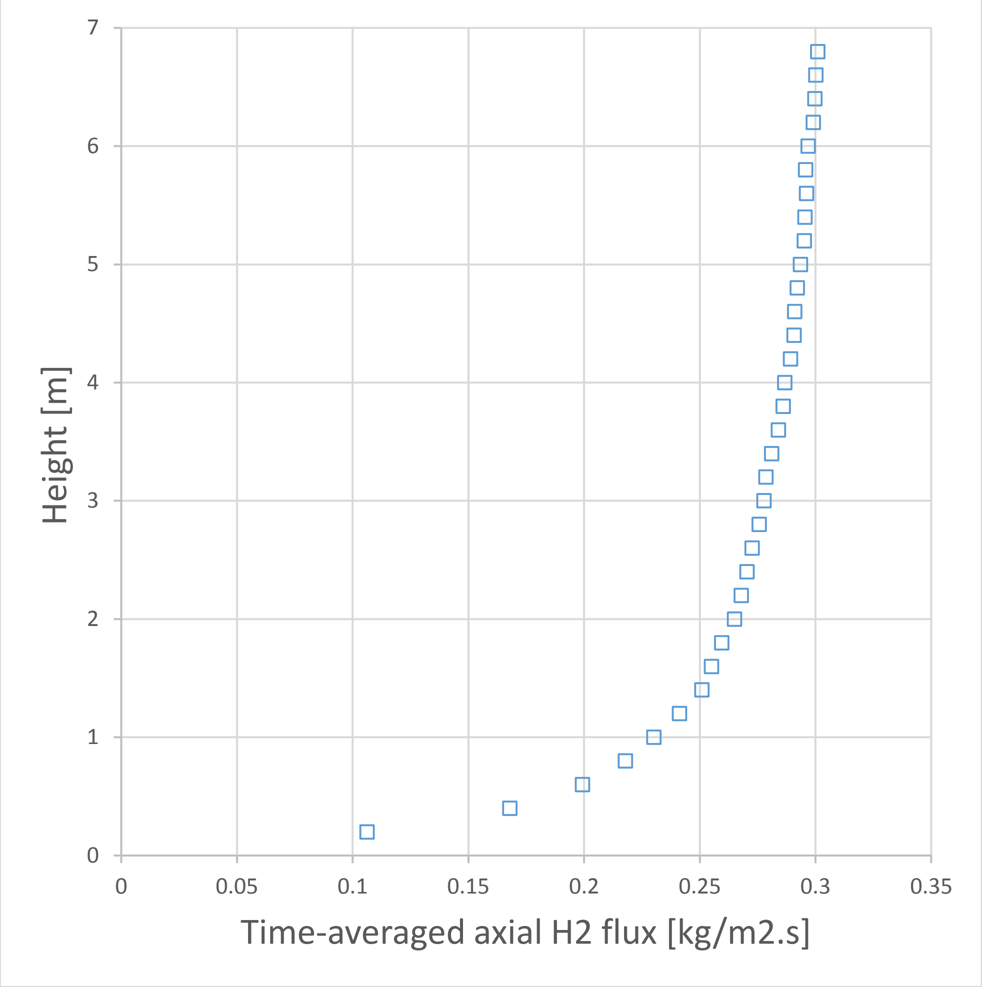

**Figure 4.9** The time-averaged axial profile of $H_2$ flux out of the SESMR riser in the best performance case (run 33).

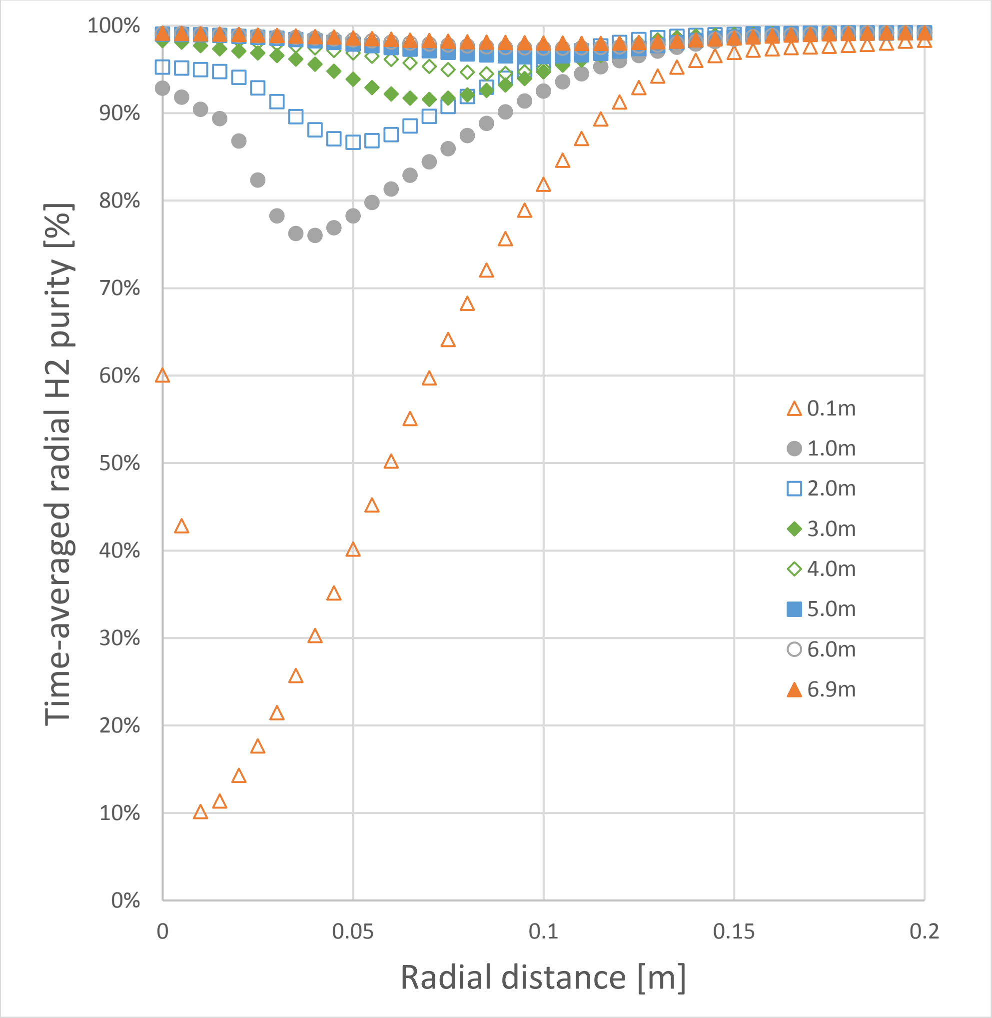

**Figure 4.10** The time-averaged radial profiles of $H_2$ purity at different heights of the SESMR riser in the best performance case (run 33).

Because SESMR was a very rapid reaction, solid distribution and mixing of the catalyst and the sorbent were expected as the keys to make SESMR developed in the system as previous discussion. Figure 4.11 shows time- and area-averaged axial profiles of volume fraction of the solid phases. The amount of catalyst, sorbent and total solid were most dense at height over the solid inlet (volume fraction of total solid was about 0.25). All the volume fractions of each solid were gradually decreased along axial direction until the volume fraction of total solid was in 0.06-0.20 which was the range of fast fluidized bed regime and close to be in 0.01-0.06 range of pneumatic transport regime (Kunii and Levenspiel, 1997). Due to dense zone in the lower height thus the axial profile of $H_2$ flux in figure 4.9 increased obviously in this lower zone.

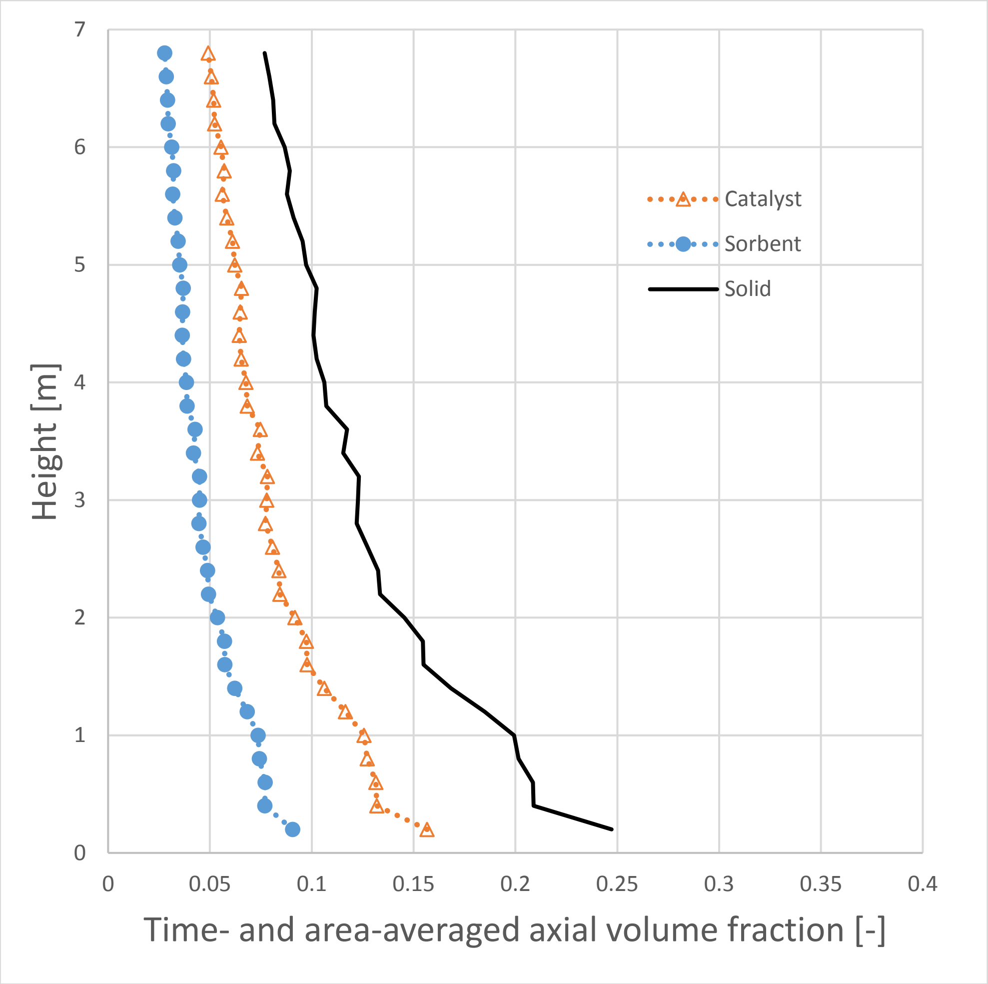

**Figure 4.11** The time- and area-averaged axial profiles of volume fraction of solid phases in the SESMR riser in the best performance case (run 33).

In figure 4.12, the time- and area-averaged axial profile of volumetric catalyst to sorbent ratio was plotted comparing with the ratio where the solid entranced (1.778

vol./vol.). The results showed that in the lower zone, the ratio was lower but still more than 1.7 vol./vol. then back to the inlet ratio in the zone above 5.0 m height. This meant there was good mixing of the catalyst and the sorbent, and thus SESMR could be well performed all along axial direction. The ratio decreased because the catalyst had higher density (2,200 kg/m$^3$) than the sorbent (approximately 1,540 kg/m$^3$) so the lighter sorbent was lifted easier.

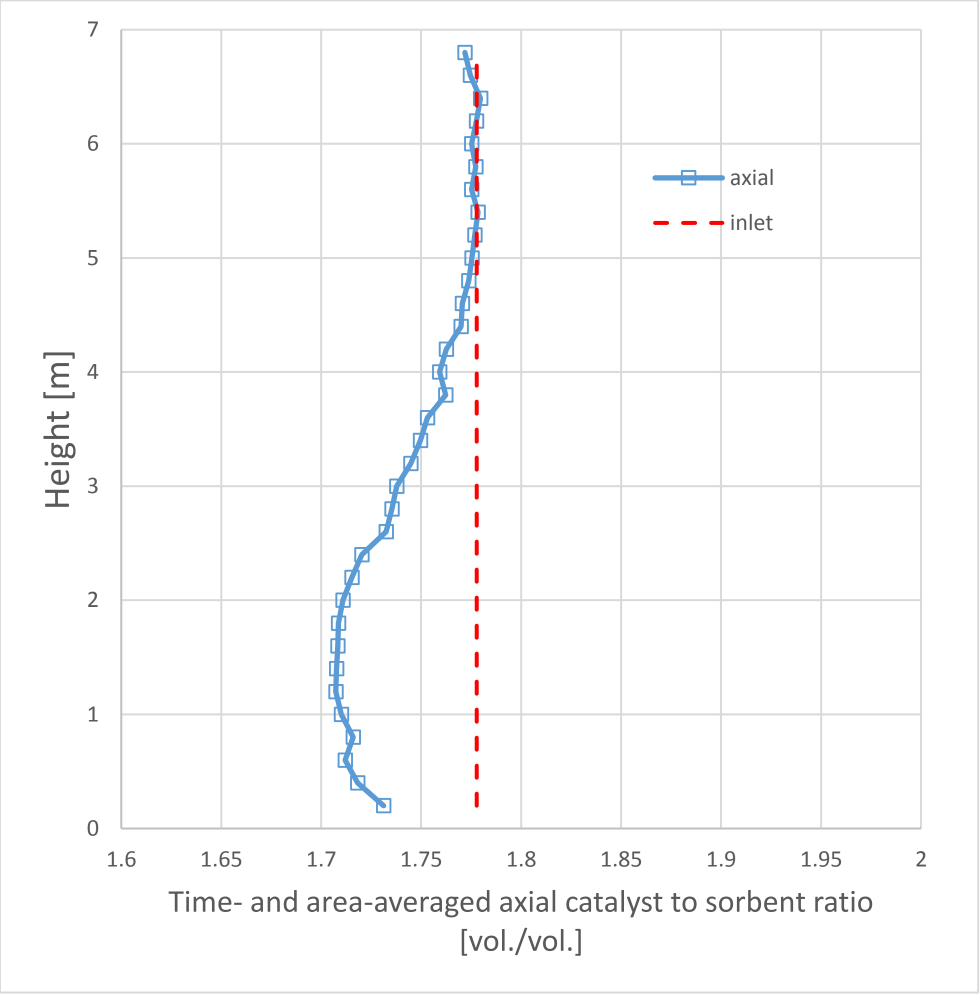

**Figure 4.12** The time- and area-averaged axial profile of volumetric catalyst to sorbent ratio in the SESMR riser in the best performance case (run 33).

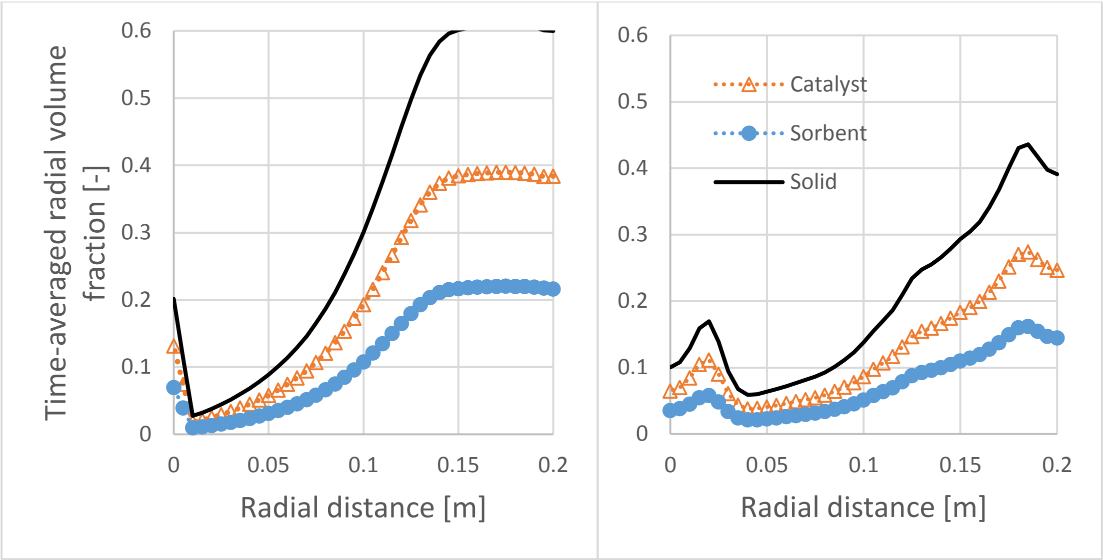

(a) 0.1 m height (b) 1.0 m height

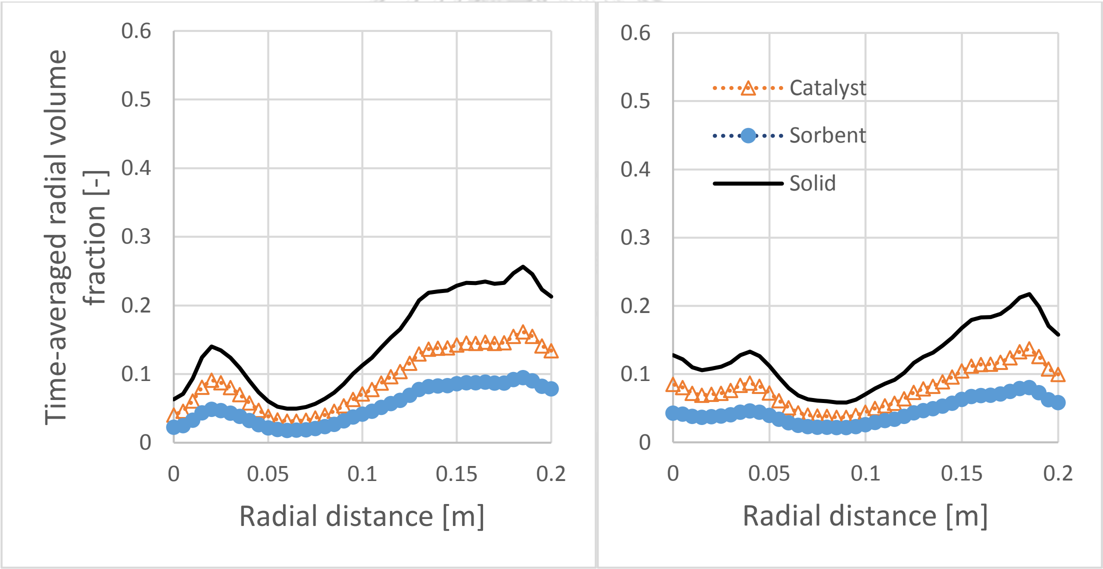

(c) 2.0 m height (d) 3.0 m height

**Figure 4.13** The time-averaged radial profiles of volume fraction of solid phases at different heights of the SESMR riser in the best performance case (run 33).

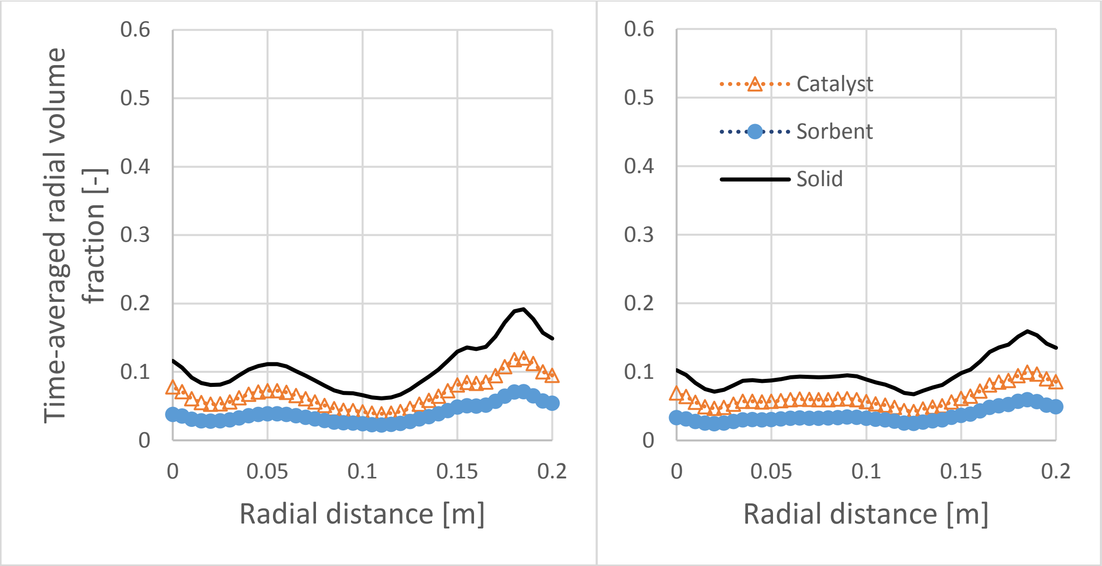

(e) 4.0 m height (f) 5.0 m height

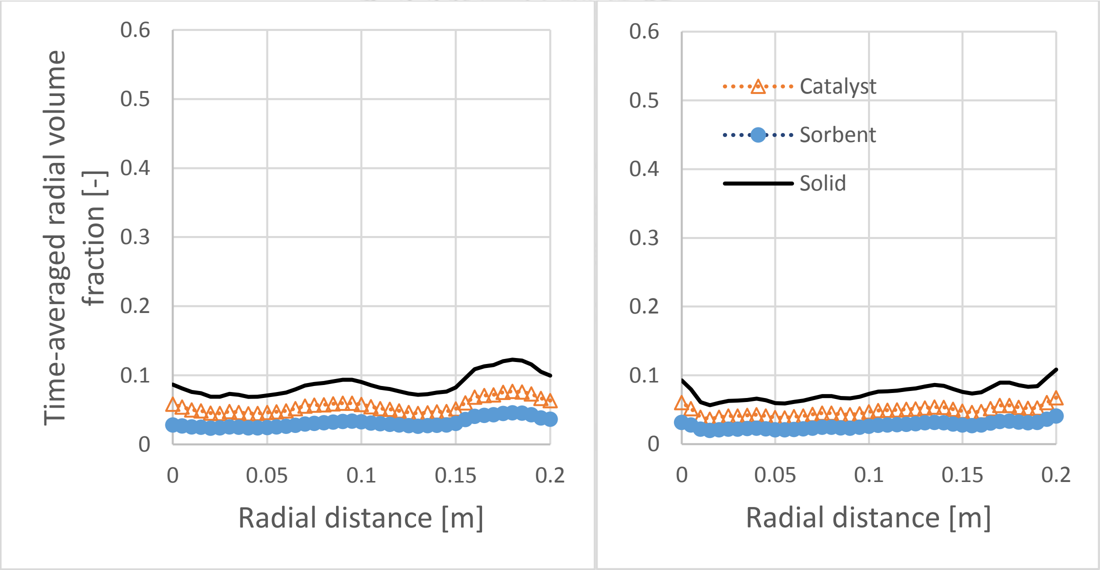

(g) 6.0 m height (h) 6.9 m height

**Figure 4.13** (continued)

Figure 4.13 shows the time-averaged radial profile of volume fraction of each solid phase at different heights. At the height over the solid entrance (0.1 m height), the total solid was dense near the solid entrance on the right but dilute at distance near the left wall. When the solids were flowed up to 4.0 m height, the volume fraction of solids at the right wall would gradually decrease to balance with at the left wall. In this height range (0.1-4.0 m height), the solids near the both wall were obviously denser than in the middle. These profiles were core-shell formation of fast fluidization. At heights over 5.0 m, the radial profiles had very low fraction and quite uniform distribution and accompany with the axial profile of volume fraction of the total solid discussed previously in figure 4.11, thus the fluidization occurred in the system of run 33 was in fast fluidization regime.

In figure 4.14, the time-averaged radial profile of volumetric catalyst to sorbent ratio at different heights were plotted comparing with the ratio where the solid entranced (1.778 vol./vol.). The results indicated that profiles near the left wall had little higher ratio than the inlet ratio but the ratios near the right wall were little less than the inlet ratio. This is because solids entranced from the channel on the right wall with normal direction to the wall, so the heavier catalyst would flow directly to the left wall more than the sorbent. While the lighter sorbent would be lifted up at right zone more than the catalyst. However, the ratios had only slightly change (were in 1.6 to 2.1 vol./vol.). Therefore, the mixing of the catalyst and the sorbent in radial direction was still in good condition and accompany with the axial profile of volumetric catalyst to sorbent ratio discussed previously in figure 4.12, thus SESMR could perform well at almost zone inside the riser and this maximized the $H_2$ flux and made the $H_2$ purity reach the equilibrium.

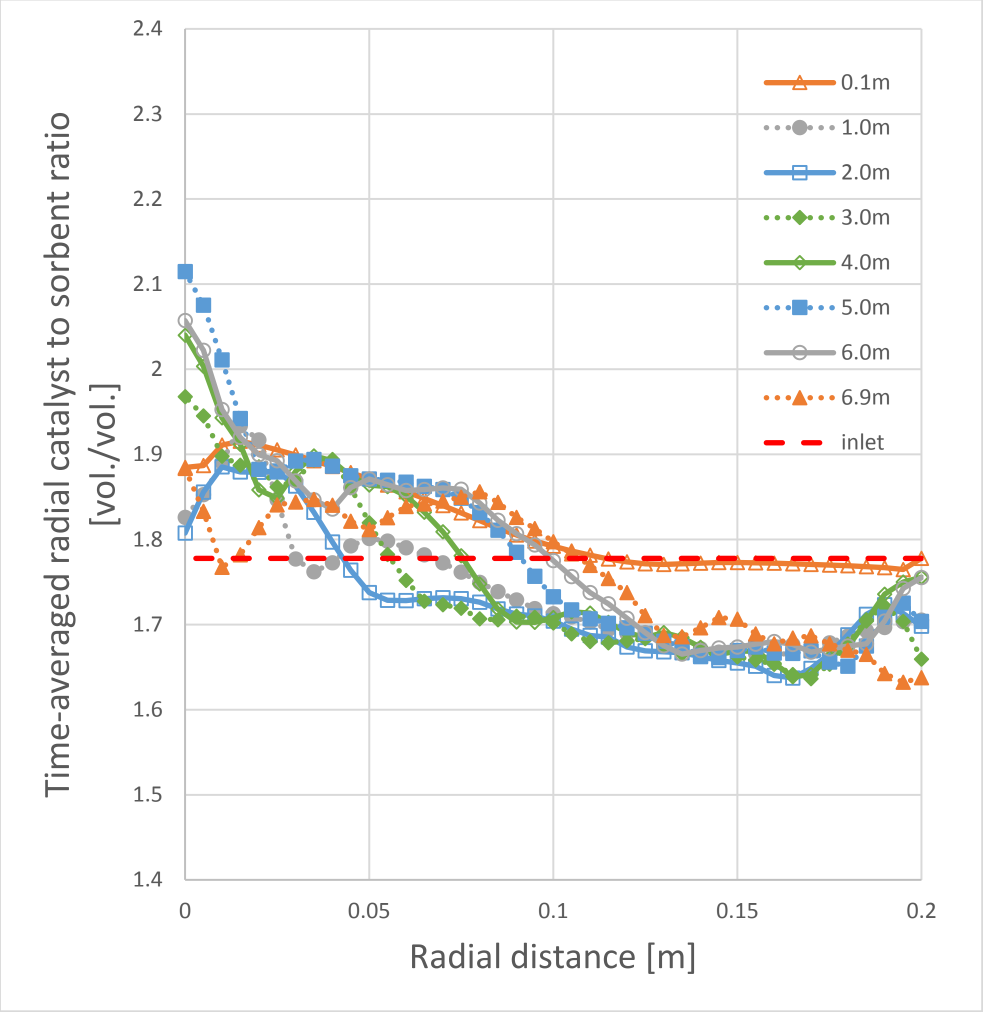

**Figure 4.14** The time-averaged radial profiles of volumetric catalyst to sorbent ratio at different heights of the SESMR riser in the best performance case (run 33).

### 4.3 SESRE performance in the riser

#### 4.3.1 Time average and mesh refinement of the SESRE reformer

Figure 4.15 shows the fluctuation in time dependence from simulation of an example case which the riser had diameter of 0.2 m, inlet temperature was 600°C, catalyst to sorbent ratio was 2.54 kg/kg, gas velocity was 4 m/s and solid flux was 200 kg/m$^2$s. In this case, $H_2$ flux at the exit of the riser was plotted every 0.1 s. and was stable after approximately 3 s. In each other runs of this study, the fluctuation had stability after 3-5 s. Thus, a time-averaged range of 10–20 s would be used to represent further simulation results in this study.

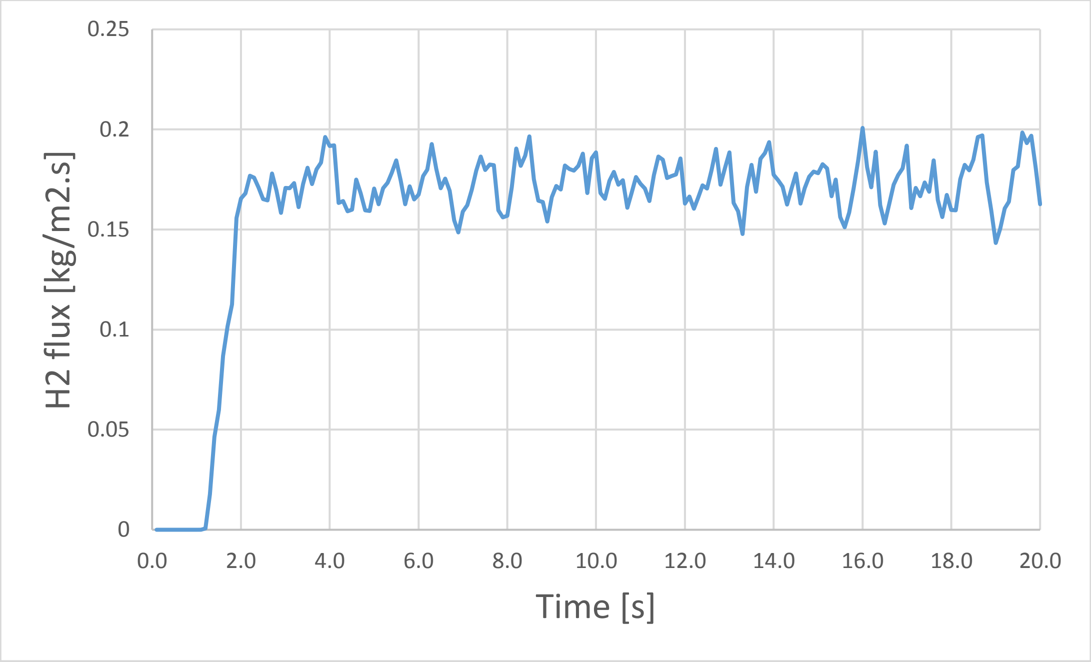

**Figure 4.15** The $H_2$ flux out of the SESRE riser as a function of time in case of id = 0.2 m, $T_{in}$ = 600°C, Cat/Sb = 2.54, U = 4 m/s and $G_s$ = 200 kg/m$^2$s.

In the same example case, mesh refinement was investigated by axial profiles of time-averaged $H_2$ flux with different sizes of cell ($\Delta x \cdot \Delta y$) as displayed in figure 4.16. The results of the $H_2$ flux showed that the 10 mm x 20 mm size differed from the others and was not precise. Whereas the other sizes had good agreement together, the 5 mm x 10 mm size was not chosen because the higher number of cells spent more unnecessary calculating time. Lastly, the 5 mm x 20 mm size and the 10 mm x 10 mm size had the same number of cells, but the 5 mm x 20 mm size should be chosen for further simulation because the radial profiles in the riser had obviously more variances than the axial profiles.

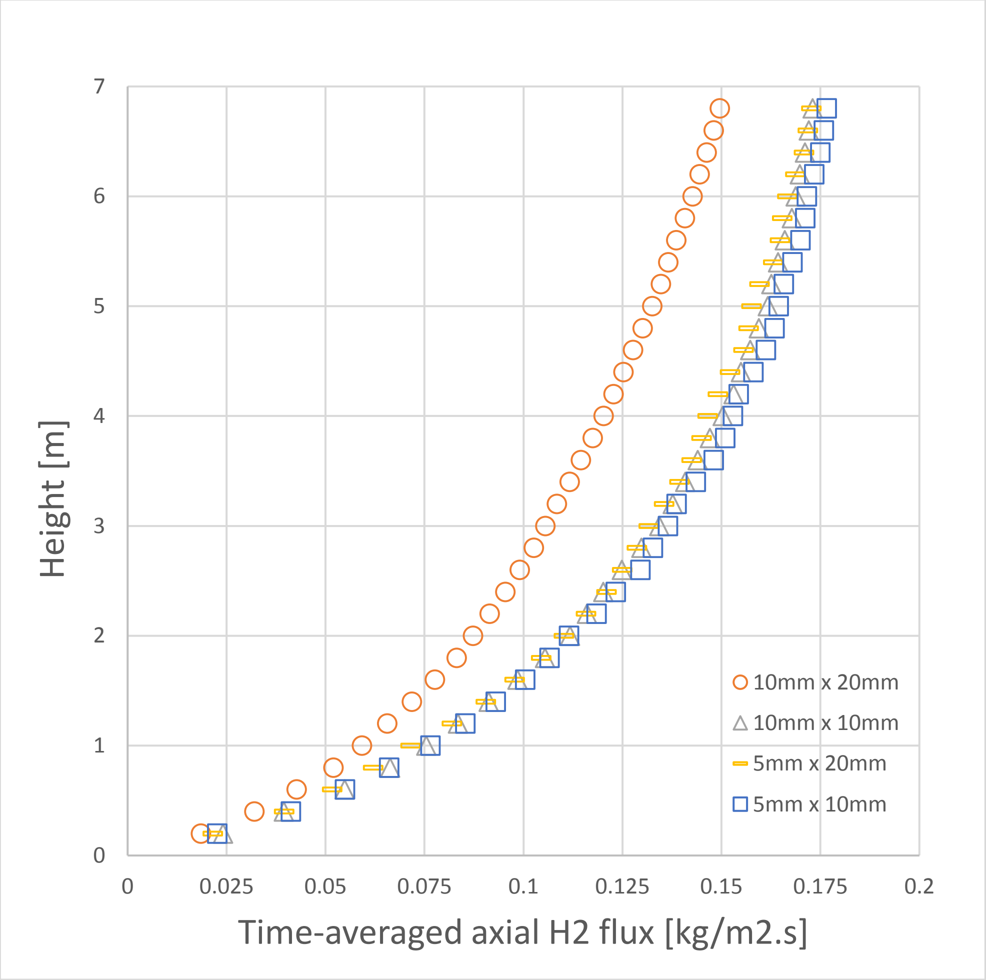

**Figure 4.16** The time-averaged axial profiles of $H_2$ flux of the SESRE riser with different cell sizes in case of id = 0.2 m, $T_{in}$ = 600°C, Cat/Sb = 2.54, U = 4 m/s and $G_s$ = 200 kg/m$^2$s.

### 4.3.2 Parametric analysis for SESRE operation

Similar to the SESMR riser, the gas inlet velocity, the solid flux, the diameter of riser, the catalyst to sorbent ratio and the temperature of inlets were studied with $2^5$ factorial design. Their two levels and other fixed values are shown in table 4.10.

**Table 4.10** The parameters chosen in the $2^5$ full factorial design of the SESRE riser.

| Parameters | Value | |
|---|---|---|
| Design parameters | | |
| Gas inlet velocity (U) | 3 and 4 | m/s |
| Solid flux ($G_s$) | 100 and 200 | kg/m$^2$s |
| Diameter of the riser (id) | 0.1 and 0.2 | m |
| Height of the riser (H) | 7 (Chosen) | m |
| Reaction parameters | | |
| Catalyst to sorbent ratio (Cat/Sb) | 0.58 and 2.54 | kg/kg |
| Steam/Ethanol molar ratio (S/E) | 6 (Chosen) | mol/mol |
| Temperature of inlets ($T_{in}$) | 600 and 700 | °C |
| CaO conversion of inlet sorbent ($X_{CaO,in}$) | 0 (Chosen) | % |

Table 4.11 shows the area-averaged values of $H_2$ flux, $H_2$ purity and CaO conversion near the outlet with the time-averaged of 10-20 s in all 32 runs. According to discussion in Johnsen *et al.* (2006), the dolomite would decrease its CaO capacity every cycle until be steady at 28% CaO conversion. There was no run which CaO conversion reached 28%, thus the dolomite could be circulated in this CFBR system for SESRE in these ranges of the parameters. Considering the $H_2$ flux and the $H_2$ purity as response variables, the lowest $H_2$ flux (0.0691 kg/m$^2$s) and the lowest $H_2$ purity (56.47% in dry basis) were occurred in the same run of no. 14. On the contrary, the highest $H_2$ flux was 0.174 kg/m$^2$s when operated in run 20 but the $H_2$ purity was only

87.57% in this case. Whereas the highest $H_2$ purity was 94.07% in run 27 but the $H_2$ flux dropped to 0.134 kg/m$^2$s. Hence, statistical analysis like the ANOVA was used for investigating the best case and for sensitivity analyses. In the ANOVA of the $H_2$ flux and the $H_2$ purity, the riser diameter (id), the inlet temperature ($T_{in}$), the catalyst to sorbent ratio (Cat/Sb), the solid flux ($G_s$), the gas velocity (U), the $H_2$ flux and the $H_2$ purity were coded as A, B, C, D, E, R1 and R2, respectively. Significant main effects and interactions, which had P-value less than 0.05 (Montgomery, 2012), of both the $H_2$ flux and the $H_2$ purity were descending sorted by the F-values or P-values as shown in tables 4.12 and 4.13.

**Table 4.11** The area-averaged $H_2$ flux, $H_2$ purity and CaO conversion ($X_{CaO}$) at the outlet of the SESRE riser from parametric study with the $2^5$ factorial design.

| Factor: | A | B | C | D | E | R1 | R2 | |
|---|---|---|---|---|---|---|---|---|
| Run | id [m] | $T_{in}$ [°C] | Cat/Sb [kg/kg] | $G_s$ [kg/m$^2$s] | U [m/s] | $H_2$ flux [kg/m$^2$s] | $H_2$ purity [% dry] | $X_{CaO}$ [%] |
| 1 | 0.1 | 600 | 2.54 | 100 | 3 | 0.132795 | 85.96 | 2.54 |
| 2 | 0.1 | 600 | 2.54 | 100 | 4 | 0.134116 | 78.85 | 2.36 |
| 3 | 0.1 | 600 | 2.54 | 200 | 3 | 0.142458 | 89.01 | 1.47 |
| 4 | 0.1 | 600 | 2.54 | 200 | 4 | 0.163118 | 85.17 | 1.53 |
| 5 | 0.1 | 600 | 0.58 | 100 | 3 | 0.107676 | 80.88 | 0.84 |
| 6 | 0.1 | 600 | 0.58 | 100 | 4 | 0.095864 | 72.13 | 0.71 |
| 7 | 0.1 | 600 | 0.58 | 200 | 3 | 0.118917 | 84.78 | 0.51 |
| 8 | 0.1 | 600 | 0.58 | 200 | 4 | 0.124579 | 80.10 | 0.50 |
| 9 | 0.1 | 700 | 2.54 | 100 | 3 | 0.122248 | 89.53 | 2.84 |
| 10 | 0.1 | 700 | 2.54 | 100 | 4 | 0.088973 | 59.58 | 0.08 |
| 11 | 0.1 | 700 | 2.54 | 200 | 3 | 0.129442 | 91.93 | 1.70 |

**Table 4.11** (continued)

| Factor: | **A** | **B** | **C** | **D** | **E** | **R1** | **R2** | |
|---|---|---|---|---|---|---|---|---|
| Run | id<br>[m] | $T_{in}$<br>[°C] | Cat/Sb<br>[kg/kg] | $G_s$<br>[kg/m$^2$s] | U<br>[m/s] | $H_2$ flux<br>[kg/m$^2$s] | $H_2$ purity<br>[% dry] | $X_{CaO}$<br>[%] |
| 12 | 0.1 | 700 | 2.54 | 200 | 4 | 0.150081 | 87.67 | 1.88 |
| 13 | 0.1 | 700 | 0.58 | 100 | 3 | 0.069700 | 59.82 | 0.02 |
| 14 | 0.1 | 700 | 0.58 | 100 | 4 | 0.069147 | 56.47 | 0.02 |
| 15 | 0.1 | 700 | 0.58 | 200 | 3 | 0.110062 | 87.66 | 0.62 |
| 16 | 0.1 | 700 | 0.58 | 200 | 4 | 0.116549 | 82.74 | 0.55 |
| 17 | 0.2 | 600 | 2.54 | 100 | 3 | 0.138739 | 88.94 | 1.54 |
| 18 | 0.2 | 600 | 2.54 | 100 | 4 | 0.162809 | 85.04 | 1.64 |
| 19 | 0.2 | 600 | 2.54 | 200 | 3 | 0.146765 | 91.30 | 0.84 |
| 20 | 0.2 | 600 | 2.54 | 200 | 4 | 0.173570 | 87.57 | 0.96 |
| 21 | 0.2 | 600 | 0.58 | 100 | 3 | 0.119885 | 84.64 | 0.52 |
| 22 | 0.2 | 600 | 0.58 | 100 | 4 | 0.128142 | 79.93 | 0.53 |
| 23 | 0.2 | 600 | 0.58 | 200 | 3 | 0.128984 | 87.32 | 0.30 |
| 24 | 0.2 | 600 | 0.58 | 200 | 4 | 0.142326 | 82.94 | 0.32 |
| 25 | 0.2 | 700 | 2.54 | 100 | 3 | 0.126764 | 91.89 | 1.68 |
| 26 | 0.2 | 700 | 2.54 | 100 | 4 | 0.143514 | 86.29 | 1.82 |
| 27 | 0.2 | 700 | 2.54 | 200 | 3 | 0.133745 | 94.07 | 0.95 |
| 28 | 0.2 | 700 | 2.54 | 200 | 4 | 0.152288 | 89.07 | 1.07 |
| 29 | 0.2 | 700 | 0.58 | 100 | 3 | 0.112057 | 88.65 | 0.63 |
| 30 | 0.2 | 700 | 0.58 | 100 | 4 | 0.115007 | 81.31 | 0.60 |
| 31 | 0.2 | 700 | 0.58 | 200 | 3 | 0.121366 | 91.26 | 0.38 |
| 32 | 0.2 | 700 | 0.58 | 200 | 4 | 0.132704 | 86.25 | 0.41 |

In table 4.12, all main effects had significance to the $H_2$ flux. The catalyst to sorbent ratio (C), the solid flux (D), the riser diameter (A), the inlet temperature (B) and the gas velocity (E) were very high significant with P-values < 0.0001, in descending order. Furthermore, the significant interactions were AD, DE and AE with the AD was the most significant among all interactions. In table 4.13, almost main effects had significance to the $H_2$ purity except the inlet temperature (B). However, interactions of the inlet temperature (AB, AD, BD and ABD) occurred significant to the $H_2$ purity. Whereas the solid flux (D), the riser diameter (A), the gas velocity (E) and the catalyst to sorbent ratio (C), in descending order, were very high significant with P-values < 0.0001. These indicated that the riser diameter (A) and the solid flux (D), both design parameters, were the key parameters for $H_2$ production performance in this ranges of the system.

**Table 4.12** The results of the ANOVA of the $H_2$ flux out of the SESRE riser.

| Source | Sum of squares | Degree of freedom (DF) | Mean square | F-value | P-value |
|---|---|---|---|---|---|
| C (Cat/Sb) | 0.005737 | 1 | 0.005737 | 79.93976 | <0.0001 |
| D ($G_s$) | 0.003190 | 1 | 0.003190 | 44.45680 | <0.0001 |
| A (id) | 0.002868 | 1 | 0.002868 | 39.96242 | <0.0001 |
| B ($T_{in}$) | 0.002229 | 1 | 0.002229 | 31.06468 | <0.0001 |
| AD | 0.000702 | 1 | 0.000702 | 9.778820 | 0.004733 |
| E (U) | 0.000538 | 1 | 0.000538 | 7.493613 | 0.011736 |
| DE | 0.000419 | 1 | 0.000419 | 5.836395 | 0.024042 |
| AE | 0.000399 | 1 | 0.000399 | 5.552999 | 0.027341 |
| Residual | 0.001651 | 23 | 7.18E-05 | | |
| Cor Total | 0.017732 | 31 | | | |

From the ANOVAs, regression models for prediction the $H_2$ flux and the $H_2$ purity were determined using eqs. 4.3 and 4.4, respectively.

$$H_2 \text{ flux} = 0.126700 + 0.0095A - 0.0083B + 0.0134C + 0.0100D + 0.0041E - 0.00468AD + 0.00353AE + 0.00362DE \quad (4.3)$$

$$H_2 \text{ purity} = 83.40 + 3.88A + 2.97C + 4.03D - 3.33E + 1.96AB - 2.58AD + 2.04BD - 1.92ABD \quad (4.4)$$

where A, B, C, D and E in the regression models were coded variables which transformed low to high levels of considered parameters into -1 to +1 range.

**Table 4.13** The results of the ANOVA of the $H_2$ purity out of the SESRE riser.

| Source | Sum of squares | Degree of freedom (DF) | Mean square | F-value | P-value |
|---|---|---|---|---|---|
| D ($G_s$) | 519.2369 | 1 | 519.2369 | 26.61521 | <0.0001 |
| A (id) | 481.9729 | 1 | 481.9729 | 24.70513 | <0.0001 |
| E (U) | 354.6858 | 1 | 354.6858 | 18.18060 | 0.000292 |
| C (Cat/Sb) | 281.9324 | 1 | 281.9324 | 14.45138 | 0.000920 |
| AD | 213.7666 | 1 | 213.7666 | 10.95732 | 0.003054 |
| BD | 133.1668 | 1 | 133.1668 | 6.825905 | 0.015563 |
| AB | 122.3844 | 1 | 122.3844 | 6.273218 | 0.019790 |
| ABD | 117.8375 | 1 | 117.8375 | 6.040152 | 0.021944 |
| Residual | 448.7076 | 23 | 19.50902 | | |
| Cor Total | 2673.691 | 31 | | | |

In additions, the sensitivity analyses were determined. The main effects and interactions on the $H_2$ flux and the $H_2$ purity were plotted as shown in figures 4.17 and 4.18, respectively. The slopes could indicate either positive or negative effects on the response variable and the steepness of each slope could indicate the significant order, as well as the coefficients in regression models.

In case that the $H_2$ flux was the response variable in figure 4.17a, all of the main effects were positive trend except that the inlet temperature (B), according to their coefficients in the regression model. To obtain the suitable condition, the catalyst to sorbent ratio (C) prefers the high level (2.54 kg/kg) but in the other hand, the inlet temperature (B) prefers the low level (600°C). Even though SESRE had been found performing well around 600-700°C (Comas *et al.*, 2004; Olivas *et al.*, 2014), SESRE had a breakthrough of sorption enhancement and performed like SRE at about 750°C (Da Silva and Müller, 2011). At 700°C the sorbent would lose $CO_2$ capture ability and was closer to turn into decarbonation condition instead. So carbonation of CaO, which is exothermic reaction, preferred much lower temperature under the breakthrough. Positive direction of the solid flux (D) indicated that the low flux (100 $kg/m^2s$) gave insufficient contact between the feed gas and the particles of catalyst/sorbent. Considering the riser diameter (A), the larger diameter get more $H_2$ flux because the bigger area of gas inlet made the feed increased, even though the dilute region of solid might be wider. At last, increase of the gas velocity (E) made feed increased despite the residence time must be less. However, the SESRE has very fast kinetics, thus SESRE had sufficient time to approach system equilibrium.

Considering the main effects on the $H_2$ purity in figure 4.18a, the solid flux (D), the riser diameter (A) and the catalyst to sorbent ratio (C) had positive effects on the $H_2$ purity as well as on the $H_2$ flux. This meant that at the high levels of these parameters (id = 0.2 m, $G_s$ = 200 $kg/m^2s$ and Cat/Sb = 2.54 kg/kg), contact of gas-catalyst/sorbent was better than at the low levels. Such as the case of the $H_2$ flux in figure 4.17a, these confirmed that the solid flux of 100 $kg/m^2s$ gave too less amount of catalyst/sorbent to contact with the feed if compared with the solid flux of 200 $kg/m^2s$. And the catalyst to sorbent ratio of 0.58 kg/kg had insufficient catalyst to produce more $H_2$ although the reforming was enhanced by $CO_2$ capture. Only the gas velocity (E) had negative effect on the $H_2$ purity which was opposed to the $H_2$ flux.

This is because the higher gas velocity (4 m/s) might made more feed but the residence time was less and far from the SESRE equilibrium.

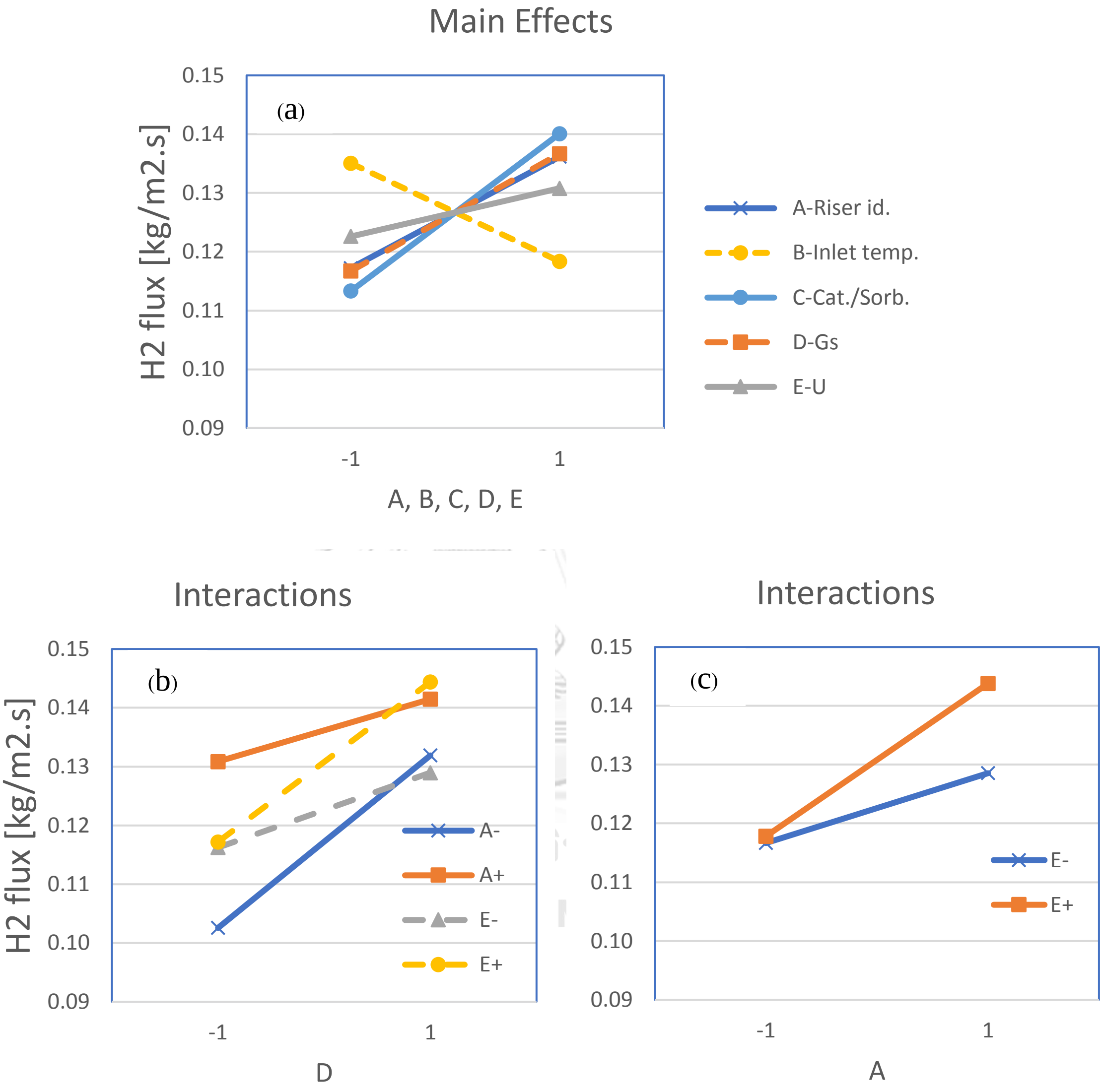

**Figure 4.17** The main effects (a) and the interactions (b and c) on the $H_2$ flux out of the SESRE riser.

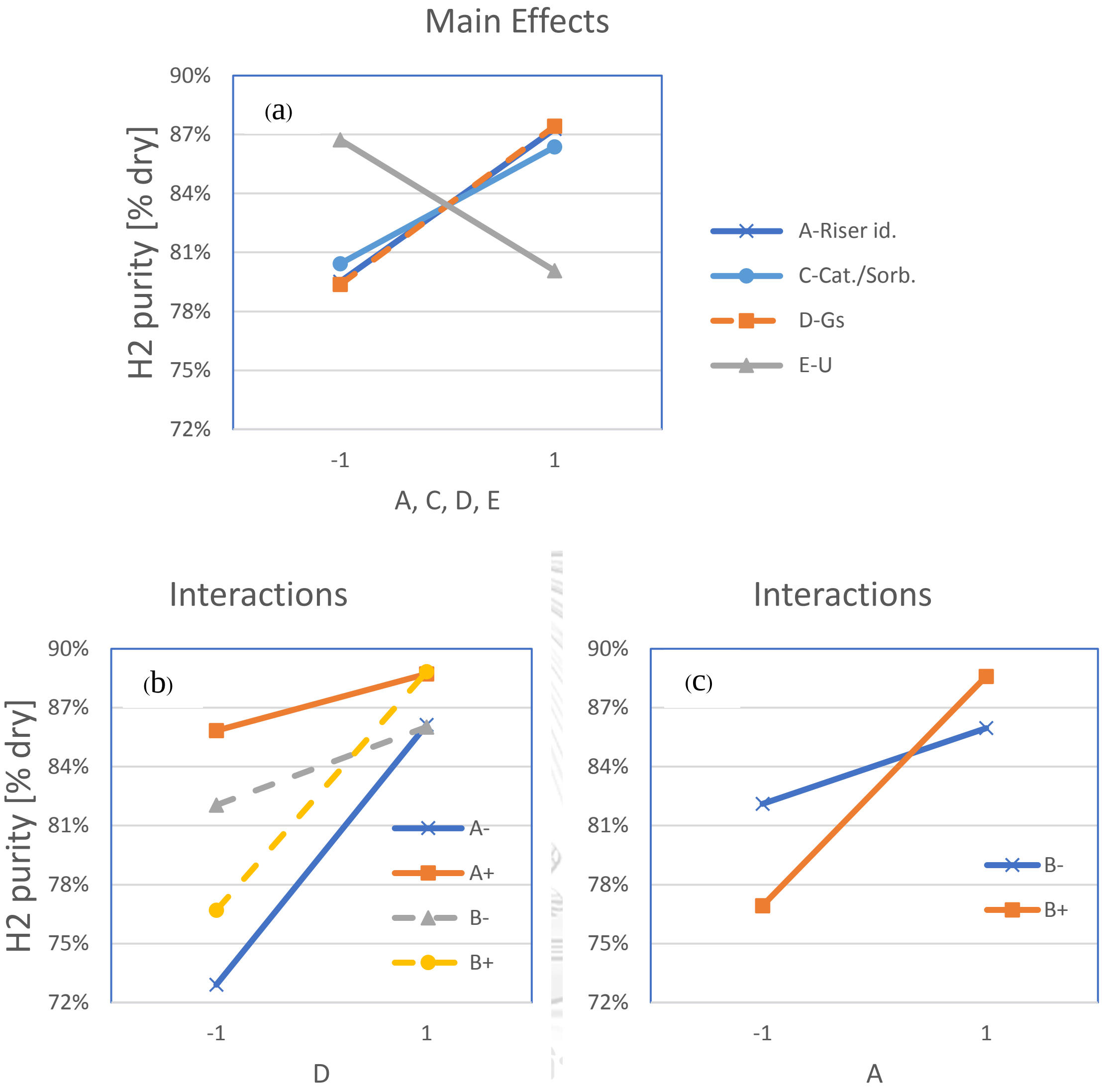

**Figure 4.18** The main effects (a) and the interactions (b and c) on the $H_2$ purity out of the SESRE riser.

A part of figures 4.17b and 4.18b show similarity of interaction between the solid flux and the riser diameter (AD) on the $H_2$ flux and the $H_2$ purity, respectively. When the solid flux (D) was considered constant, lines of the high riser diameter (A+) gave higher values of both the $H_2$ flux and the $H_2$ purity than lines of the low riser diameter (A-). These because their main effects (A and D) were positive, thus at their high levels, they mutually enhance both the $H_2$ flux and the $H_2$ purity. The slopes of all lines of the riser diameter (A+ and A-) still had the same positive direction as the main effect (D) with slight changes of steepness. This indicated that the interaction (AD) were less effective than the main effects (D), according to their P-values in tables 4.12 and 4.13 and their regression coefficients in eqs. 4.3 and 4.4. However, at high level side of the solid flux (D+), the positive effect of the high riser diameter (A+) over the low riser diameter (A-) was less than that at low level side of the solid flux (D-). In other words, when the diameter of riser was larger, increase of the solid flux was less effective (or less significant) than in the smaller diameter. This was in accord with the small negative regression coefficients of their interaction (AD) in eqs. 4.3 and 4.4 which would a little decrease the values of both the $H_2$ flux and the $H_2$ purity when both the solid flux and the riser diameter were positive.

Considering the interaction of the gas velocity (E) on the $H_2$ flux in figures 4.17b and 4.17c. Because all of the main effects (A, D and E) were positive, thus their interactions (AE and DE) were more positive to the $H_2$ flux. When the solid flux (D) and the riser diameter (A) were at preferred high level as previous discussed in figure 4.17a and were enhanced with higher gas velocity (D+E+ and A+E+), the $H_2$ flux would get much higher because the increase of the gas velocity was increase of the feed as well. Whereas when the riser diameter (A) was at smallest, the interactions with gas velocity (A-E- and A-E+) were very close i.e. had rarely affect the $H_2$ flux. This indicated that although the higher gas velocity would increase the feed, the resident time would be insufficient if the riser diameter was too small. These very small deviations also indicated that the interactions (AE and DE) were less effective than the main effects (A and D), corresponding to their high P-values in table 4.12 and their very small regression coefficients in eq. 4.3.

Lastly, considering the interaction of the inlet temperature (B) on the $H_2$ purity in figures 4.18b and 4.18c. The line of high inlet temperature (B+) crossed with the line of low inlet temperature (B-) when both interacting with the solid flux (D) and the riser diameter (A). That meant in this range of the inlet temperature (600-700°C), there was no clearly favorite temperature for getting higher $H_2$ purity. Moreover, the little deviations of the steepness of the interactions (AD, BD, and AB) indicated that these interactions were less effective than the main effects (A and D), consistent with their P-values in table 4.13 and their regression coefficients in eq. 4.4.

**Table 4.14** The maximum $H_2$ flux out of the SESRE riser from the regression models and a simulation.

| Factor: | A | B | C | D | E | R1 | R2 | |
|---|---|---|---|---|---|---|---|---|
| | id [m] | $T_{in}$ [°C] | Cat/Sb [kg/kg] | $G_s$ [kg/m$^2$s] | U [m/s] | $H_2$ flux [kg/m$^2$s] | $H_2$ purity [% dry] | $X_{CaO}$ [%] |
| Optimizing R1 prior to R2 | 0.200 | 600.00 | 2.539 | 199.86 | 3.96 | 0.173570 | 86.53 | |
| Simulation (Run 20) | 0.200 | 600.00 | 2.540 | 200.00 | 4.00 | 0.173570 | 87.57 | 0.96 |

Table 4.14 shows optimizing the $H_2$ flux from the regression models in eq. 4.3 prior to optimizing the $H_2$ purity from eq. 4.4. The maximum $H_2$ purity was predicted only 86.53% in dry basis and the $H_2$ flux reached 0.174 kg/m$^2$s in the riser with 0.2 m diameter, the inlet temperature of 600°C, the catalyst to sorbent ratio of 2.54 kg/kg, the solid flux of 200 kg/m$^2$s and the gas velocity of 4 m/s. These results from the

prediction confirmed very well to the results from simulation with these values of the parameters, i.e. run 20. The $H_2$ purity and the $H_2$ flux from run 20 were 87.57% in dry basis and 0.174 kg/m$^2$s, respectively.

**Table 4.15** The maximum $H_2$ purity out of the SESRE riser from the regression models and a simulation.

| Factor: | A | B | C | D | E | R1 | R2 | |
|---|---|---|---|---|---|---|---|---|
| | id<br>[m] | $T_{in}$<br>[°C] | Cat/Sb<br>[kg/kg] | $G_s$<br>[kg/m$^2$s] | U<br>[m/s] | $H_2$ flux<br>[kg/m$^2$s] | $H_2$ purity<br>[% dry] | $X_{CaO}$<br>[%] |
| Optimizing R2 prior to R1 | 0.200 | 627.11 | 2.540 | 199.94 | 3.00 | 0.147427 | 94.07 | |
| Simulation (Run 33) | 0.200 | 627.00 | 2.540 | 200.00 | 3.00 | 0.145503 | 88.62 | 0.72 |

In case that optimizing the $H_2$ purity prior to optimizing the $H_2$ flux as shown in table 4.15, the maximum $H_2$ purity was predicted up to 94.07% in dry basis and the $H_2$ flux was dropped to 0.147 kg/m$^2$s in the riser with 0.2 m diameter, the inlet temperature of 627°C, the catalyst to sorbent ratio of 2.54 kg/kg, the solid flux of 200 kg/m$^2$s and the gas velocity of 3 m/s. To confirm the results from the prediction, another case with those values of parameters was simulated as run 33. But the predicted $H_2$ purity (94.07% in dry basis) did not conform to the $H_2$ purity from simulation of run 33 (only 88.62% in dry basis). Thus, the case of run 33 could not be the optimum case of the $H_2$ purity. In this case, the inlet temperature was predicted at 627°C, while the other parameters (the riser diameter, the catalyst to sorbent ratio, the solid flux and the gas velocity) were predicted at their bound. According to previous discussion about unclear preferred inlet temperature in figures 4.18b and

4.18c, then additional prediction cases were determined for the best case instead of run 33 by changing the inlet temperature to its bounds at 600°C and 700°C. The both cases would match simulations of run 19 and run 27, respectively, as shown in table 4.16.

**Table 4.16** The optimum cases of the SESRE riser from the regression models and simulations.

| Factor: | A | B | C | D | E | R1 | R2 | |
|---|---|---|---|---|---|---|---|---|
| | id [m] | $T_{in}$ [°C] | Cat/Sb [kg/kg] | $G_s$ [kg/m$^2$s] | U [m/s] | $H_2$ flux [kg/m$^2$s] | $H_2$ purity [% dry] | $X_{CaO}$ [%] |
| Run 27: Prediction | 0.200 | 700.00 | 2.540 | 200.00 | 3.00 | 0.135370 | 97.11 | |
| Run 27: Simulation | 0.200 | 700.00 | 2.540 | 200.00 | 3.00 | 0.133745 | 94.07 | 0.95 |
| Run 19: Prediction | 0.200 | 600.00 | 2.540 | 200.00 | 3.00 | 0.151970 | 92.95 | |
| Run 19: Simulation | 0.200 | 600.00 | 2.540 | 200.00 | 3.00 | 0.146765 | 91.30 | 0.84 |

As results in table 4.16, there was a deviation at the $H_2$ purity of run 27 which predicted at 97.11% but simulated at 94.07% in dry basis. However, as previous point in table 4.11 that run 27 got the highest $H_2$ purity among all 32 runs of simulation, the simulation of run 27 also got the $H_2$ purity higher than that simulated in run 33 (88.62% in dry basis) but got the $H_2$ flux (0.134 kg/m$^2$s) less than run 33 (0.146 kg/m$^2$s). Whereas in case of run 19, both the predicted $H_2$ flux and the predicted $H_2$ purity were well conformed to the results from simulation. Furthermore, the simulation of run 19 also got both the $H_2$ purity and the $H_2$ flux (91.30% in dry basis and 0.147 kg/m$^2$s, respectively) higher than those simulated in run 33 (88.62% in dry basis and 0.146 kg/m$^2$s, respectively). Thus, run 19 might be another candidate of the optimum case in this system.

**Table 4.17** The effluent gas composition of the SESRE riser from simulations in the optimum cases.

| | $H_2$ [% dry] | $CH_4$ [% dry] | CO [% dry] | $CO_2$ [% dry] | EtOH [% dry] |
|---|---|---|---|---|---|
| Run 27 | 94.07 | 3.87 | 1.21 | 0.36 | 0.49 |
| Run 19 | 91.30 | 0.37 | 7.42 | 0.61 | 0.31 |

In additional consideration, composition of effluent gas in simulations of run 27 and run 19 were shown in table 4.17. Even the $H_2$ purity of run 27 (which was the highest among all runs) seemed to reach the equilibrium, EtOH still had not been converted completely comparing with the experimental result and the validated result in table 4.3 of which EtOH content should be approximately 0.0% in dry basis. This described that SESRE could not be performed perfectly in this CFBR system with these ranges of parameters. Moreover, $CH_4$ content was still high in run 27, while CO was still high in run 19. These indicated that the reforming reactions of $CH_4$ (SMRs) did not reach equilibrium yet in case of run 27, while the shift reaction of CO (WGS) did not reach equilibrium yet in case of run 19. Because run 19 got both the $H_2$ flux and the $H_2$ purity higher than run 33. Moreover, an additional shift reactor would likely be preferable than other effluent gas separation units to purify $H_2$ due to further producing more $H_2$ in the same time. Thus, run 19 was chosen to be the best case for SESRE operated in this system with these ranges of the parameters.

### 4.3.3 Hydrodynamics of SESRE in the riser

Due to imperfect performance of SESRE in all cases of the system, considering hydrodynamics of the best case (run 19) compared with the worst case (run 14) would explain causes of imperfection more clearly than considering hydrodynamics of only the best case.

Figure 4.19 displays the instantaneous contour plots of volume fraction of each solid phase (catalyst and sorbent) and gas phase at 20 s in run 14 and run 19. The gradient shades of colors from blue to red represent low volume fraction to high volume fraction of each phases. The contour plots showed that both the catalyst and the sorbent particles were in dense clusters in lower zone (below 2.5 m height in run 19 and 0.5 m height in run 14, approximately) of the riser. In rest upper zone of the riser, the solid particles were dense only near the wall and dilute in the center line (core) of riser in run 19, whereas the solid particles were very dilute in run 14. The contours of volume fraction of the solids could explain that in the lower zone of both runs, the bed flow seemed to be in turbulent fluidization regime. Dissimilarly in the upper zone, the bed looked like flow in fast fluidization in run 19 and dilute transportation in run 14. However, the visual similarity of volume fraction of the catalyst phase and the sorbent phase indicated very good mixing of the catalyst and the sorbent in both runs.

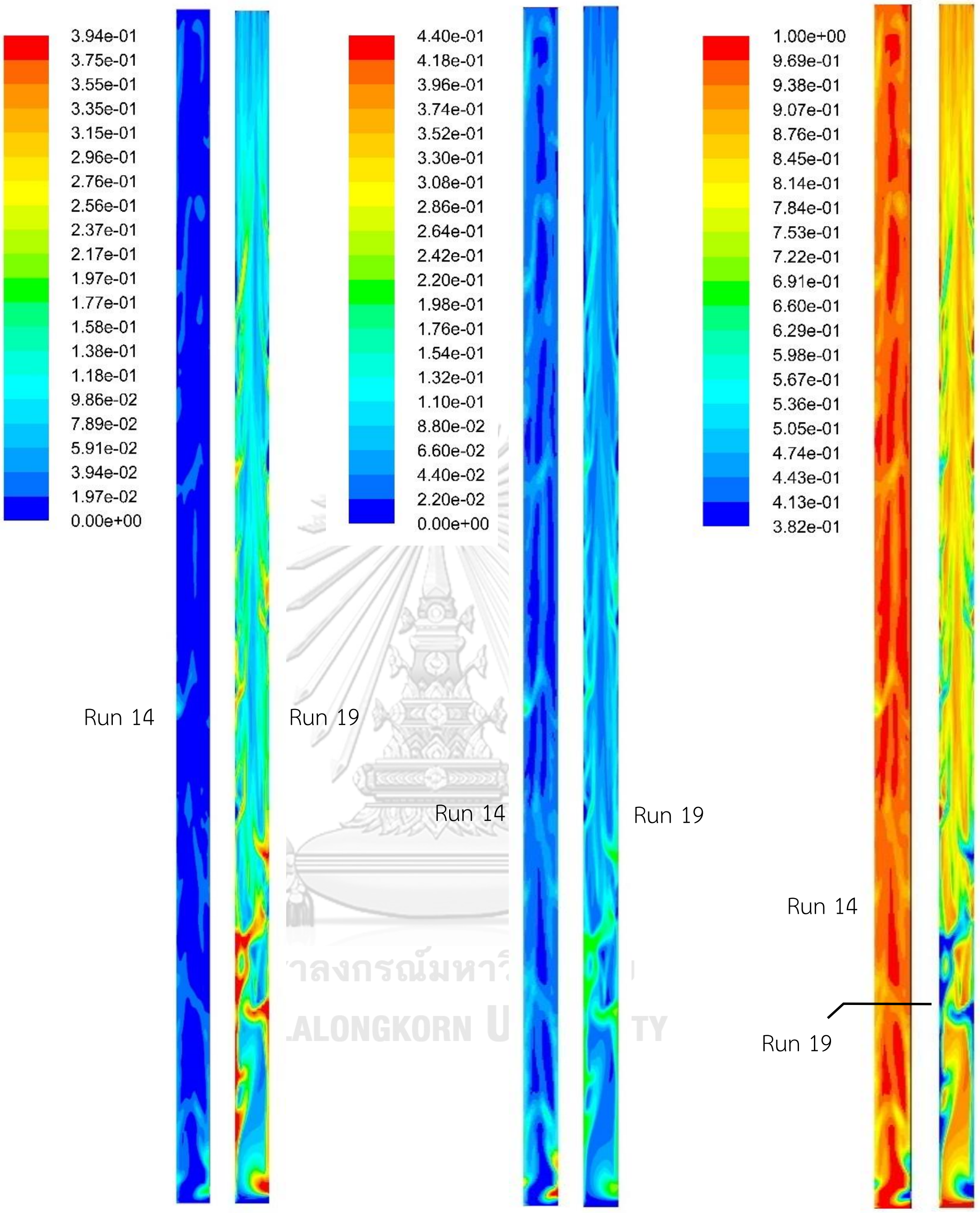

(a) Catalyst (b) Sorbent (c) Gas

**Figure 4.19** The instantaneous volume fraction of each phase in the SESRE riser at 20 s in the best performance case (run 19) and the worst performance case (run 14).

Figure 4.20 displays the instantaneous contour plots of mole fraction of $H_2$, EtOH and $CO_2$ in the gas phase at 20 s in both run 14 and run 19. The contour plots in run 19 showed that the mole fraction of each component in gas phase seemed approach full development since 2.0 m height of the riser which still be in the dense zone of the bed. However, above this zone to the exit, $H_2$ did not reach the equilibrium in the core of the riser. EtOH and $CO_2$ were not completely converted and adsorbed in the core, as well. These contours confirmed that SESRE could not be performed perfectly even in the best case of this system. Next, considering the contour plots in run 14, immediate increase of $H_2$ and $CO_2$ and immediate decrease of EtOH quite exactly matched with dense solids, as shown in figure 4.19, within the lower zone (below 0.5 m height). Above this zone, $H_2$ and $CO_2$ gradually increased while EtOH gradually decreased until to the outlet. Case of $CO_2$ was notable that in run 19, $CO_2$ immediately rose highest in the bottom core then rapidly reduced and kept steady in the upper core. Whereas in run 14, $CO_2$ immediately rose and gathered at the both sides of wall but not occurred in the core within the lower zone. These core-shell patterns of $CO_2$ in the bottom half of the riser, which also appeared in cases of produced $H_2$, might due to the solid cluster appearance inside the system in figures 4.19a and 4.19b. However, comparing $CO_2$ fraction along axial direction in overview, $CO_2$ fraction in run 14 increased gradually throughout the riser. On the contrary, $CO_2$ fraction in run 19 decreased in the bottom zone then seemed steady in the upper zone. Furthermore, $CO_2$ fraction in run 14 was higher than in run 19. The $CO_2$ fraction in run 14 indicated that the continuous increase of $CO_2$ in this upper zone could indicated that SRE, which produced $CO_2$, took place rather than the capturing of $CO_2$. In other words, insufficient amount of sorbent all along axial direction might made $CO_2$

increased gradually. Unlike in run 19, $CO_2$ fraction occurred higher in the bottom zone because carbonation was slower reaction than SRE, then $CO_2$ was more adsorbed until being steady in the rest upper zone. In conclusion, besides incomplete conversion of EtOH, which found in both runs but higher in run 14, the lack of sorption enhancement might be another cause of the worst performance of run 14.

The last contour plots in figure 4.21 show the instantaneous temperature of each phase in both runs at 20 s. In each run, all temperature contours were similar to the other phases. The contours in each run showed small deviations of temperature from their inlet temperature (973 K in run 14 and 873 K in run 19). Negative deviations were caused by highly endothermic reaction of reforming but they were neutralized by exothermic reaction of carbonation. It was noticeable that the decrease of temperature reached -13 K in run 14 but reached only -3 K in run 19, because the carbonation performed in run 14 less than in run 19. According to the mole fraction contours of gases in figure 4.20, in run 19, the temperature in the dense zone and in the core of the upper zone, where the gases still did not reach the equilibrium, was slightly lower than the temperature in where the gases reached equilibrium. While in case of run 14, the temperature gradually decreased from the bottom in accordance with the increasing of $H_2$ and $CO_2$ and the decreasing of EtOH, because the carbonation occurred higher only in the dense lower zone but the reforming took place in the rest zone, especially in the annular zone.

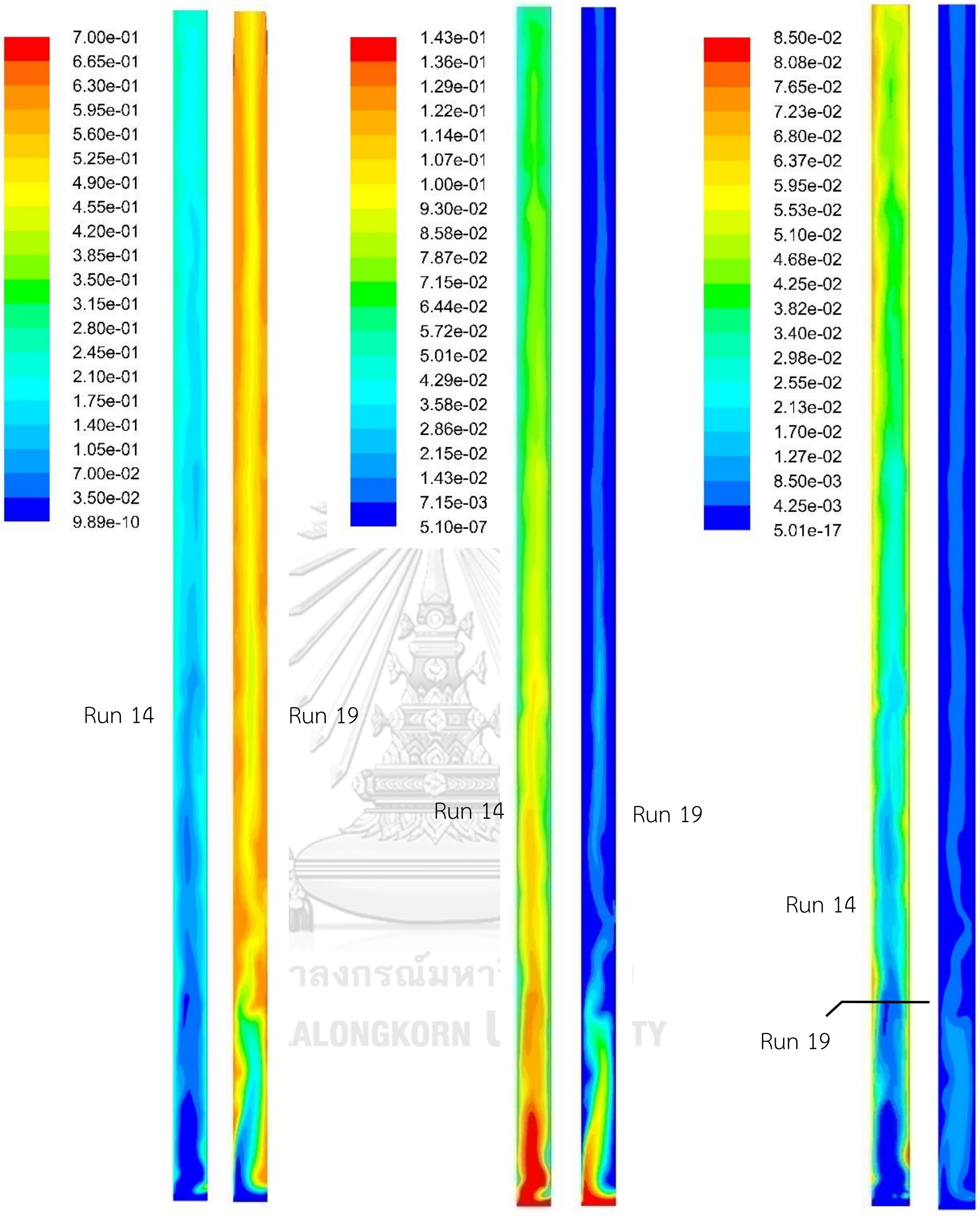

(a) $H_2$ (b) EtOH (c) $CO_2$

**Figure 4.20** The instantaneous mole fraction (wet basis) of $H_2$, EtOH and $CO_2$ in gas phase of the SESRE riser at 20 s in the best performance case (run 19) and the worst performance case (run 14).

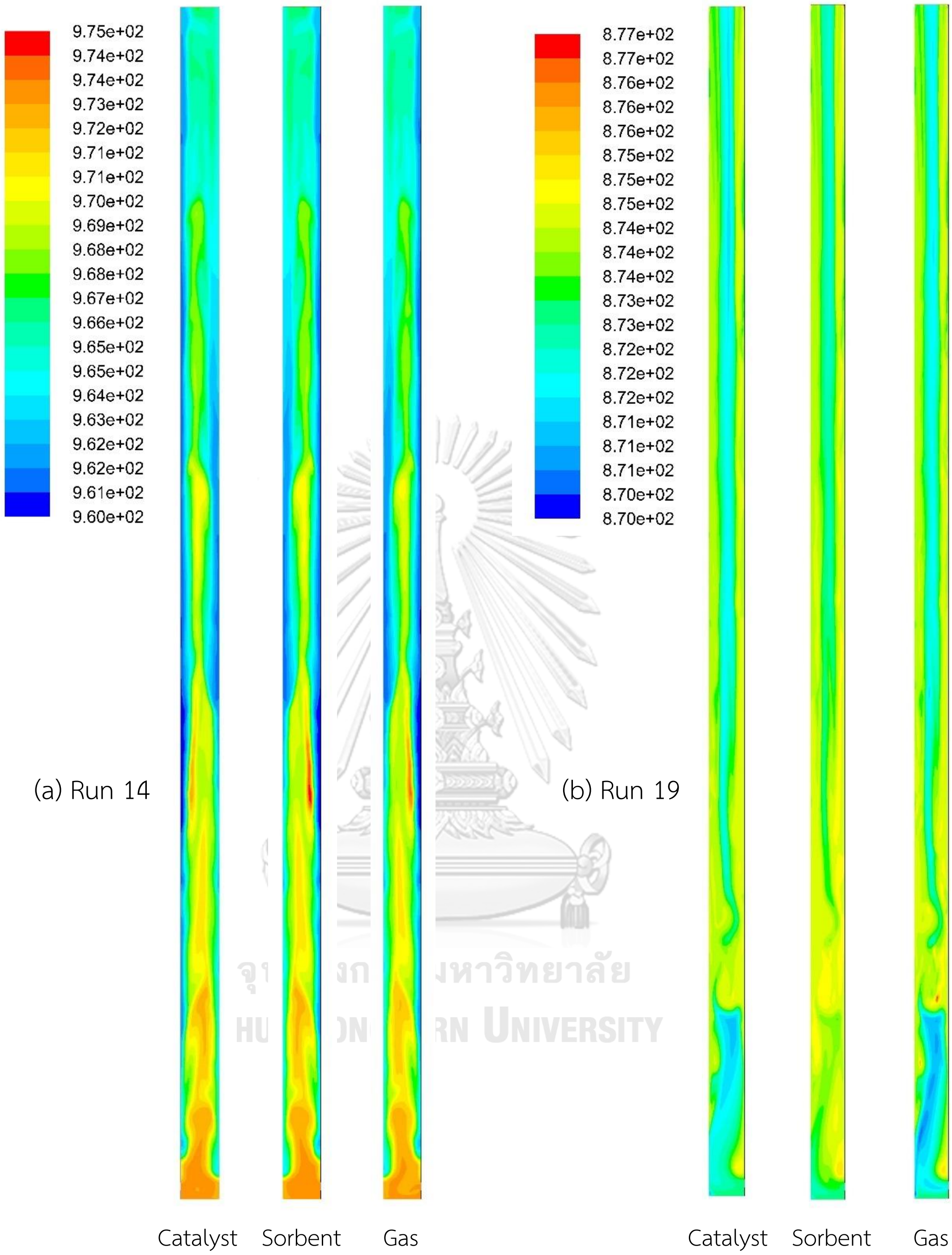

(a) Run 14

(b) Run 19

**Figure 4.21** The instantaneous temperature (in Kelvin) of each phase in the SESRE riser at 20 s for the best performance case (run 19) and the worst performance case (run 14).

Next, the catalyst and sorbent distributions along axial and radial direction were expected as key hydrodynamics parameter to explain the performance of SESRE in this riser system. Inside the riser of both runs, the volume fraction of both catalyst and sorbent phase, volumetric catalyst to sorbent ratio were compared to the $H_2$ flux and the $H_2$ purity as the following.

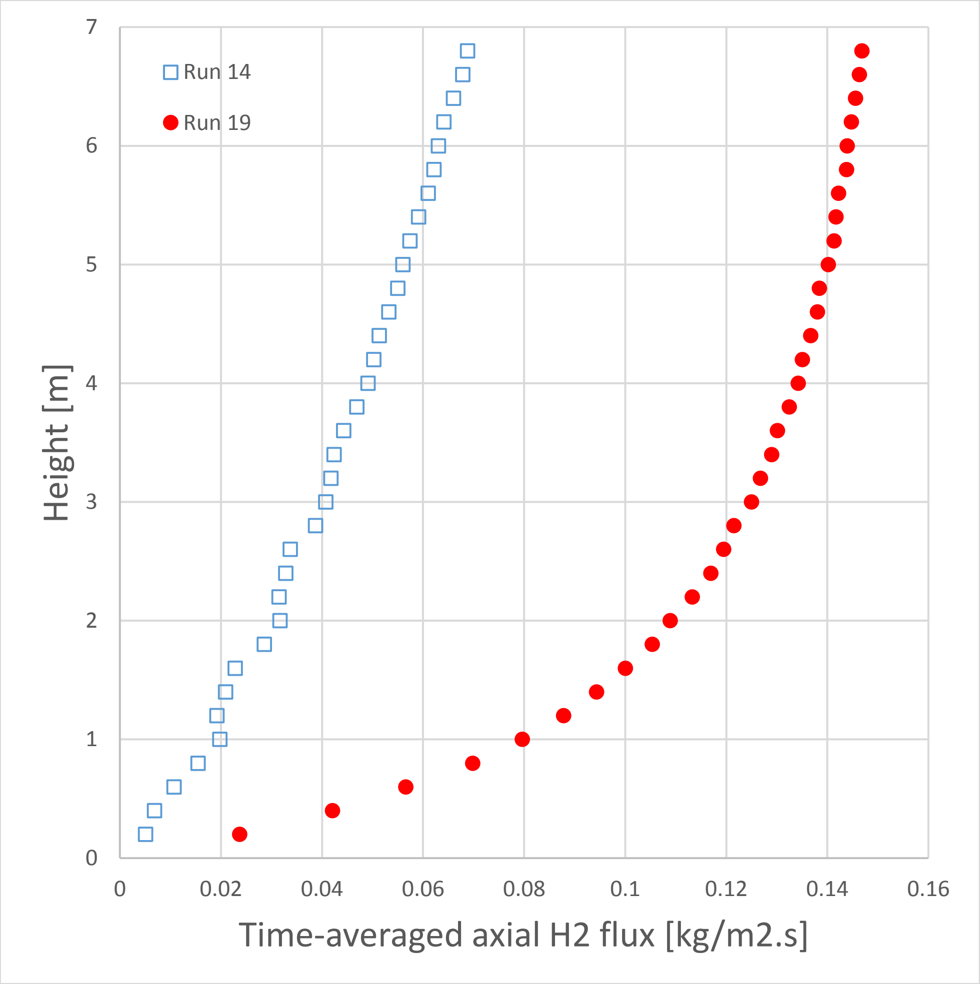

**Figure 4.22** The axial profiles of time-averaged $H_2$ flux out of the SESRE riser in the best performance case (run 19) and the worst performance case (run 14).

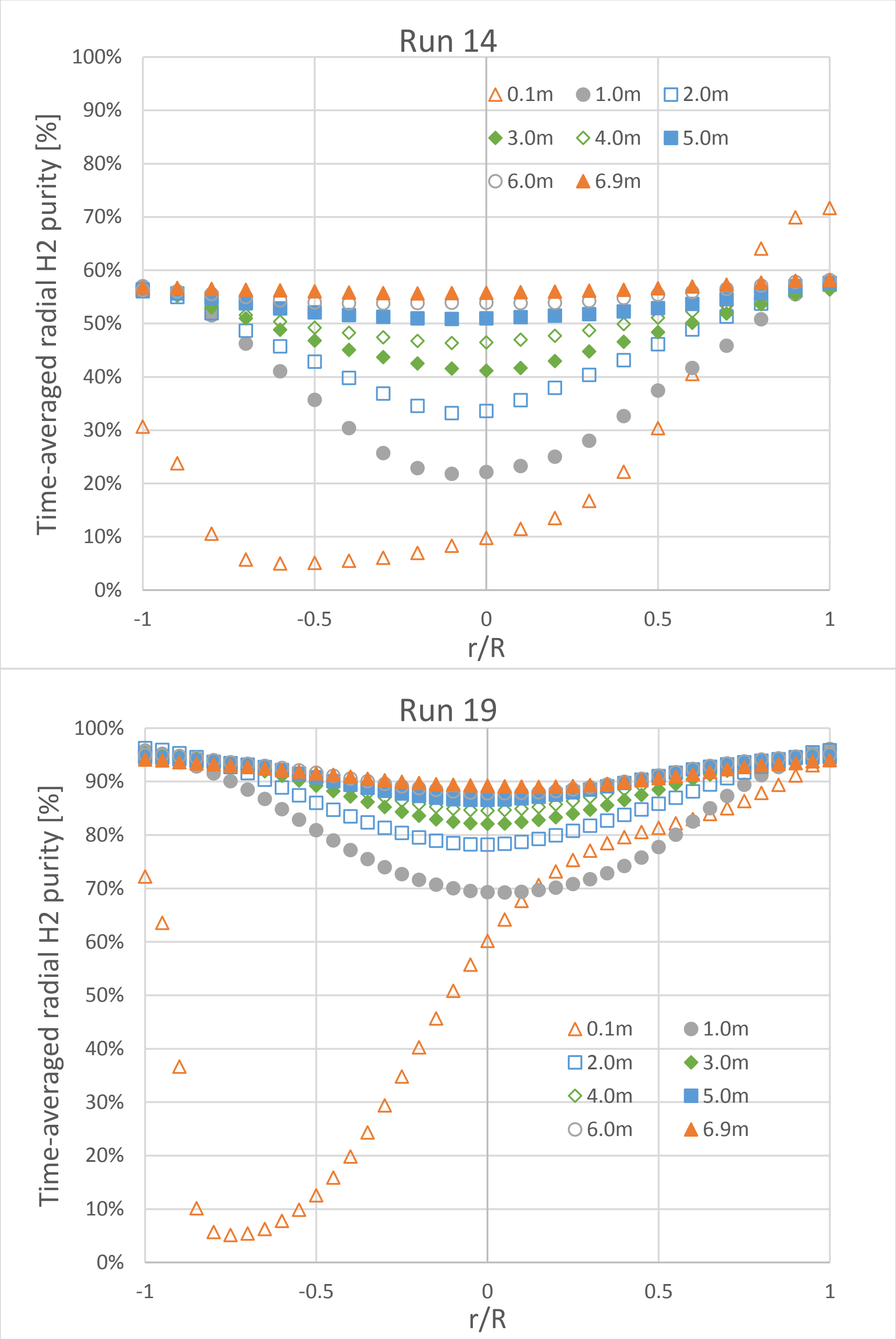

**Figure 4.23** The time-averaged radial profiles of $H_2$ purity at different heights of the SESRE riser in the best performance case (run 19) and the worst performance case (run 14).

In figure 4.22, the time-averaged $H_2$ flux in axial direction were plotted from 0.1 m height which was the exact height above the solid inlet channel. The $H_2$ flux of run 19 accumulated rapidly in the lower zone and approached maximum at the outlet, while the $H_2$ flux of run 14 increased gradually all along the axial direction. This increasing profiles of the $H_2$ flux was according to the contours of $H_2$ fraction in figure 4.20a.

Figure 4.23 shows the time-averaged radial distributions of the $H_2$ purity at different heights which solid inlet was on this right side at 0.05-0.10 m height. Each $H_2$ purity profile in run 14 looked similar to the $H_2$ purity profile in run 19 at the same height but had less purity. At exactly above solid inlet (0.1 m height) of both runs, the $H_2$ purity reached maximum immediately at the solid inlet on the right wall. The $H_2$ purity decreased along to left direction far from the solid inlet then increased near left wall. At 1.0 m height and above, the profiles in both runs were almost symmetric. Considering development of the $H_2$ purity profile at every height especially in the core of the riser, the $H_2$ purity in run 14 was gradually higher while the $H_2$ purity in run 19 rapidly increased since at 1.0 m height. The $H_2$ purity profiles between at 6.0 m and 6.9 m height of both runs were almost similar. Near the exit (6.9 m height) of both runs, the $H_2$ purity still had little drop in the core, conforming to the contour of $H_2$ fraction in figure 4.20a.

From figures 4.22 and 4.23, both the $H_2$ flux and the $H_2$ purity might be further developed to get little higher if using the riser which height was over 7 m. But in additional simulations with a 10 m high riser, there were some cases that solid accumulated in the riser and then caused errors in those simulations. Thus, the extent height of the riser over 7 m did not get better advantage for operating SESRE in this system.

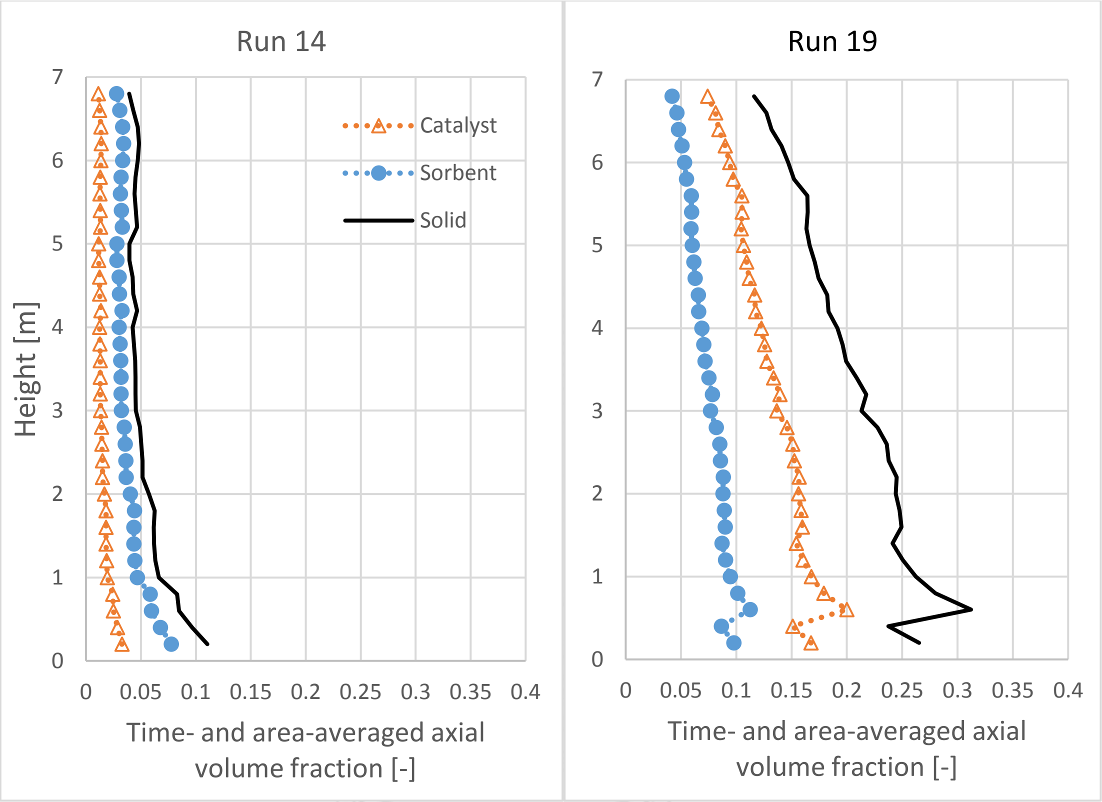

**Figure 4.24** The time- and area-averaged axial profiles of volume fraction of solid phases in the SESRE riser in the best performance case (run 19) and the worst performance case (run 14).

Because SESRE was a very rapid reaction, solid distribution and mixing of the catalyst and the sorbent might be the cause that SESRE was not performed perfectly as previous discussion. Figure 4.24 shows time- and area-averaged axial profiles of volume fraction of the solid phases in both runs. Firstly, in run 19, the amount of catalyst, sorbent and total solid were dense in the lower zone (volume fraction of total solid was about 0.25-0.30). In the upper zone, all the volume fractions of each solid continuously decreased until to the exit and the volume fraction of total solid was in 0.06-0.20 which was the range of fast fluidization regime (Kunii and Levenspiel, 1997). Considering in the lower zone, this zone could also be divided into initial acceleration region (0.5-1.5 m height) and dense phase region (1.5-2.5 m height). And in the upper zone, the decrease of total solid volume fraction was in transition region (not yet down into dilute transport region) (Mahmoudi *et al.*, 2012; Mousa *et al.*, 2014). This fluidization could also called high-dense circulation fluidized bed (HDCFB) system (Zhu, 2010). Lastly, because the bed was dense in the lower zone (the initial acceleration region and the dense phase region), thus the axial profile of $H_2$ flux of run 19 in figure 4.22 increased greatly in this lower zone. Whereas in run 14, the total solid was little dense and decreased (volume fraction about 0.10 less to 0.06) in the lower zone which not over 1.0 m height. Then all along upper height, each solid fraction hardly decreased and the total solid volume fraction was less than 0.06 that known as the flow in the dilute transport regime (Kunii and Levenspiel, 1997). The dilute fraction of each solid could cause the gradual increase of the $H_2$ flux in run 14 as discussed in figure 4.22.

In figure 4.25, the time- and area-averaged axial profile of volumetric catalyst to sorbent ratio of each run was plotted comparing with the ratio where the solid entranced (1.778 vol./vol. in run 19 and 0.4085 vol./vol. in run 14). The result showed that after sufficient height, the ratios in each run quite equaled to each inlet ratio. These indicated the good mixing of the catalyst and the sorbent which made the sorption enhancement uniform in the upper zone. Above the entrance of solid until 3.0 m height in run 14, the ratio was slightly higher because the catalyst had higher density (2,200 kg/m$^3$) than the sorbent (approximately 1,540 kg/m$^3$), so the lighter sorbent was lifted easier than the catalyst. While in run 19, the ratio was quite the same as the inlet ratio almost along the axial direction. However, the less ratio near the solid entrance might be affected by the turbulence.

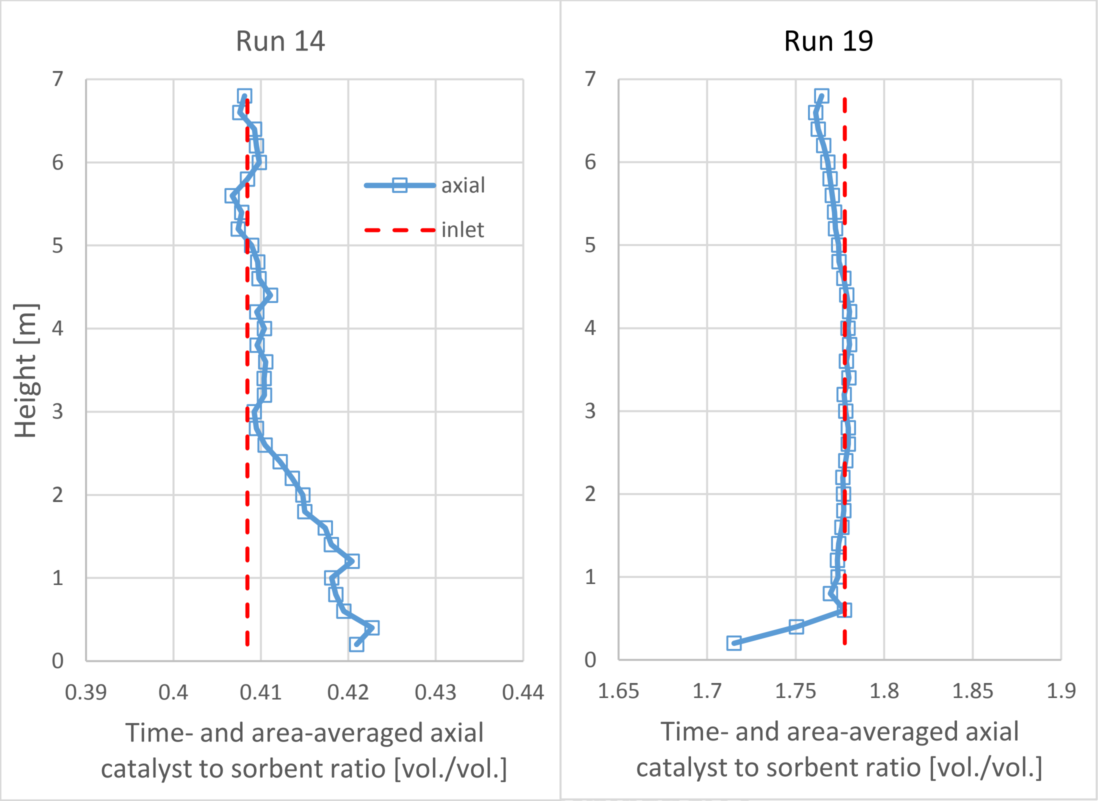

**Figure 4.25** The time- and area-averaged axial profiles of volumetric catalyst to sorbent ratio in the SESRE riser in the best performance case (run 19) and the worst performance case (run 14).

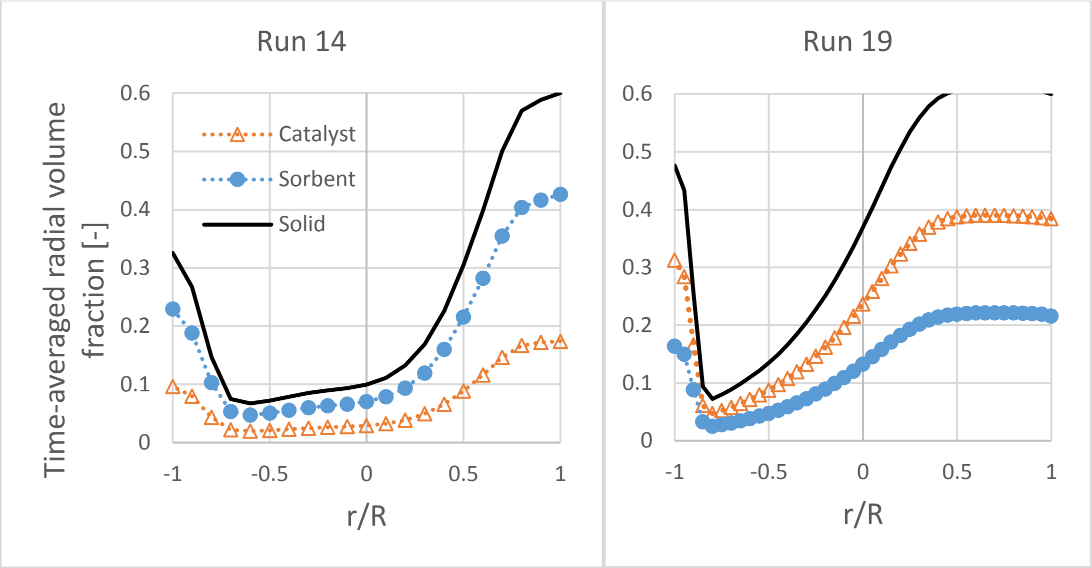

(a) 0.1 m height

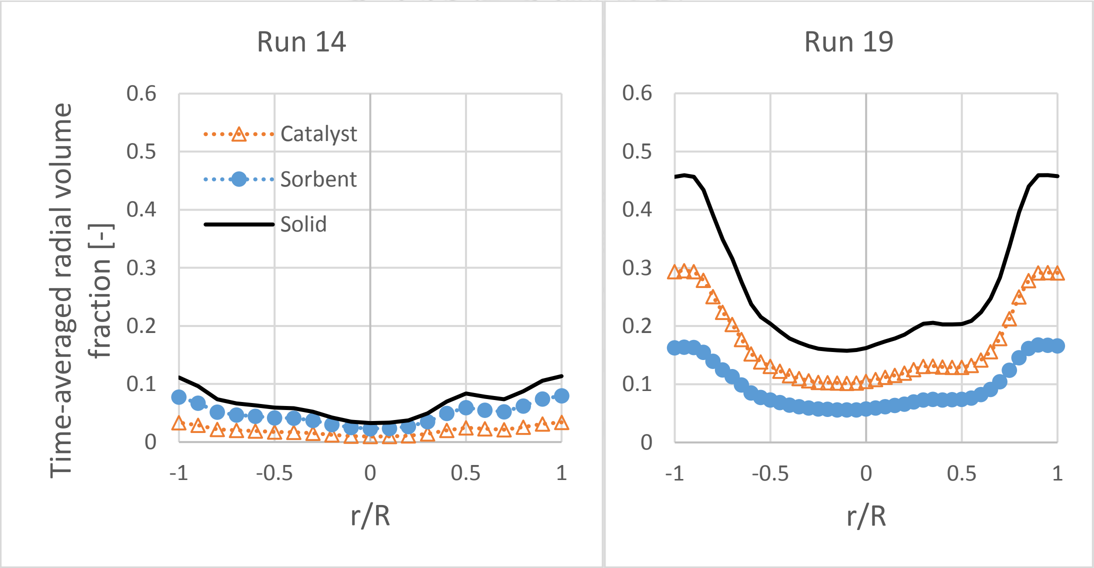

(b) 1.0 m height

**Figure 4.26** The time-averaged radial profiles of volume fraction of solid phases at different heights of the SESRE riser in the best performance case (run 19) and the worst performance case (run 14).

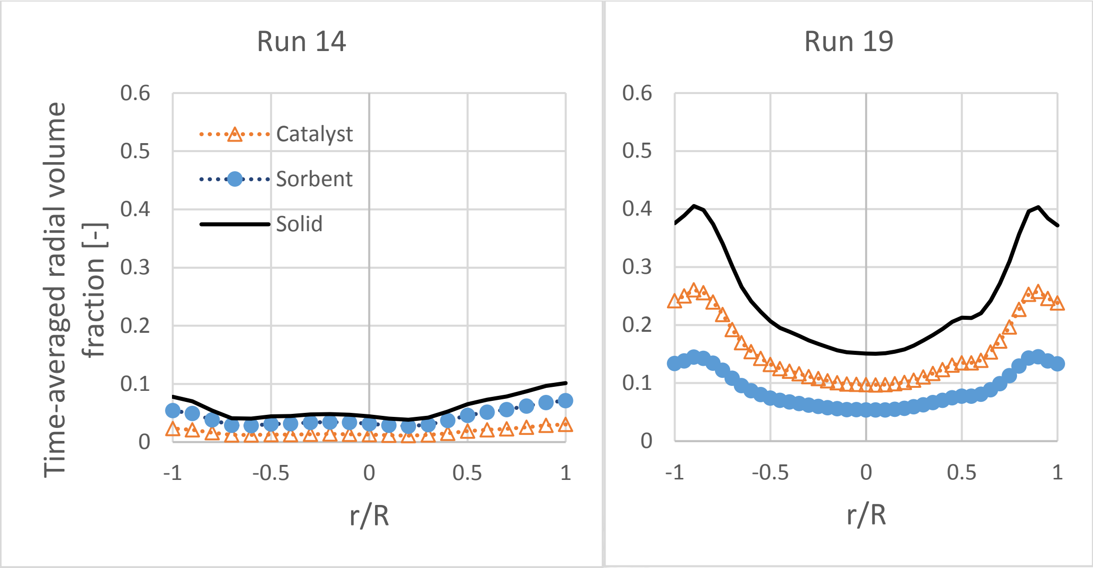

(c) 2.0 m height

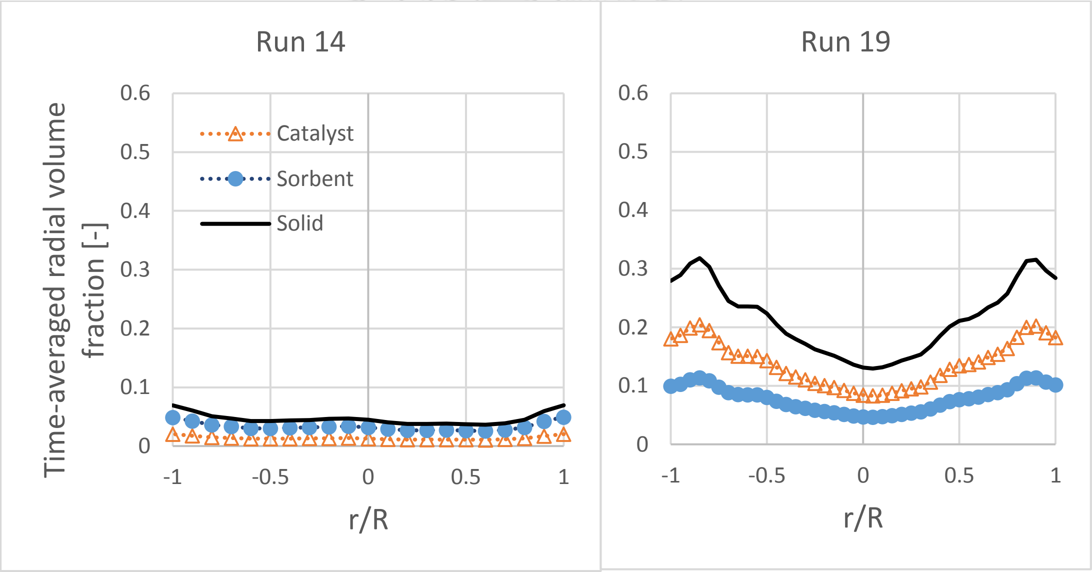

(d) 3.0 m height

**Figure 4.26** (continued)

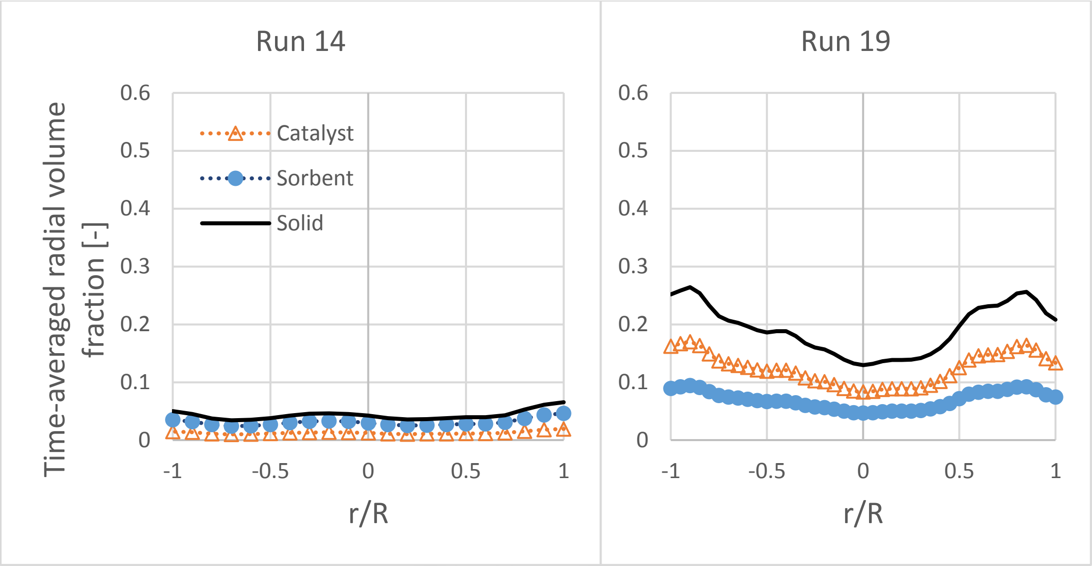

(e) 4.0 m height

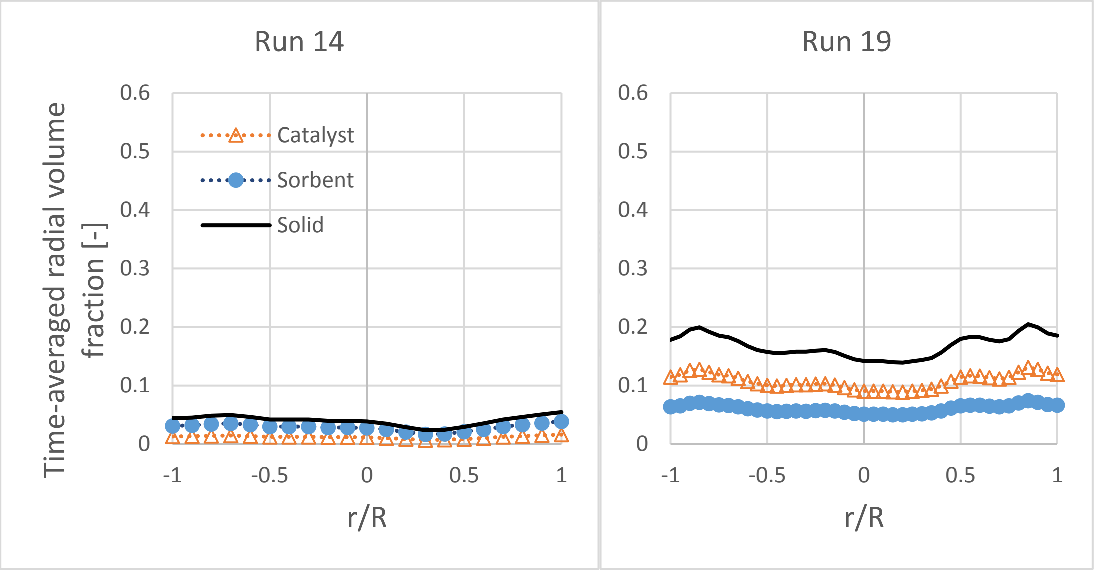

(f) 5.0 m height

**Figure 4.26** (continued)

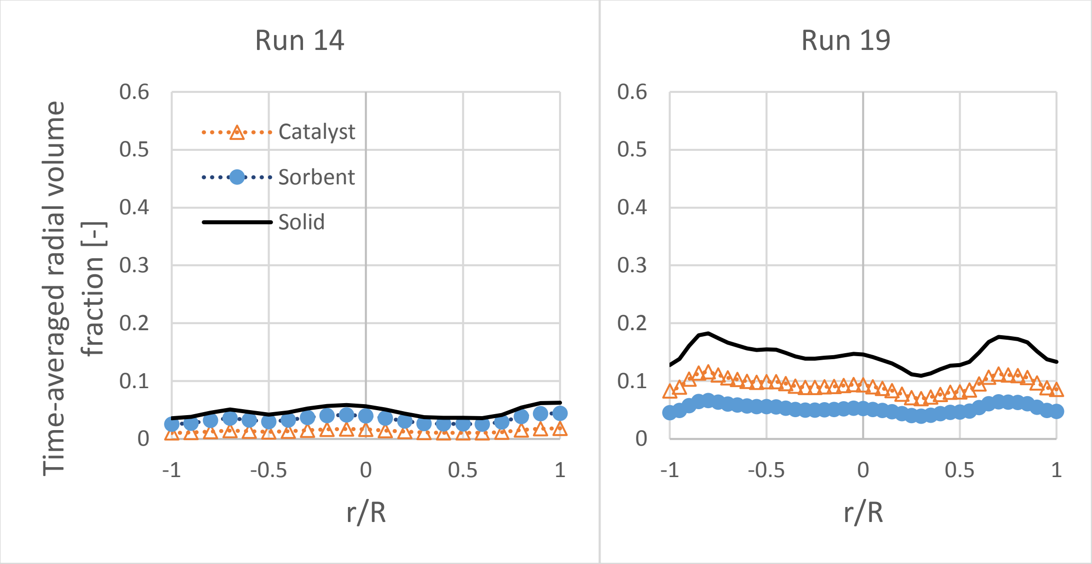

(g) 6.0 m height

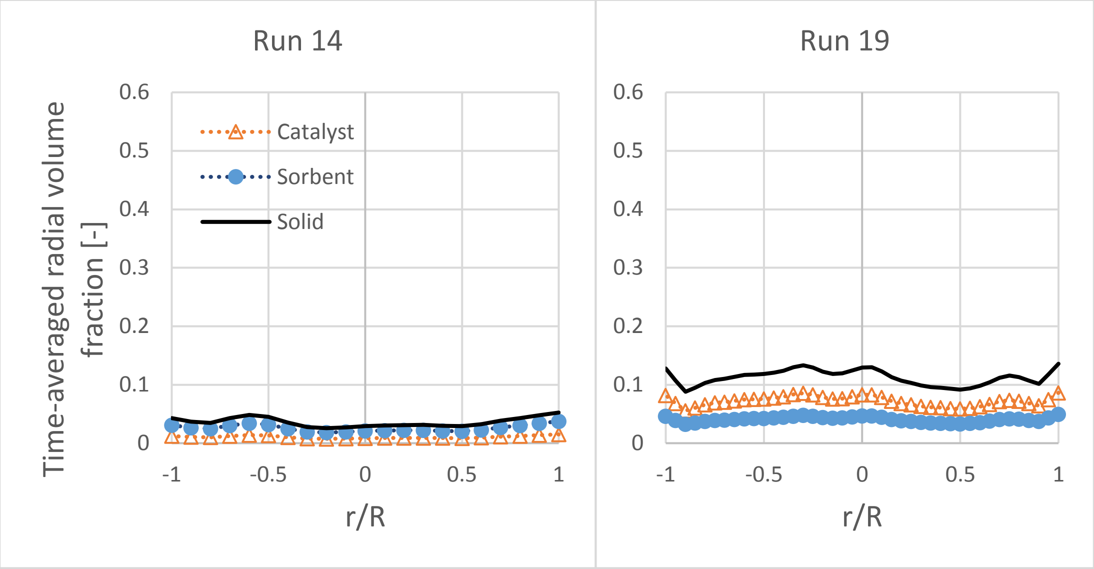

(h) 6.9 m height

**Figure 4.26** (continued)

Figure 4.26 shows the time-averaged radial profiles of volume fraction of each solid phase at different heights. At the height over the solid entrance (0.1 m height), the total solid of both runs were similarly dense near the solid entrance on the right but dilute at distance near the left wall. Whereas there was difference between each run at upper heights. In run 19 at 1.0 m height, the volume fraction of solids at the right wall would rapidly decrease to balance with at the left wall. In 1.0-4.0 m height, these profiles show core-annular flow of fast fluidization. However, the denser bed near the both wall sides would be less dense when the bed was blown higher. Until the height was over 6.0 m, the radial distribution was quite uniform. Considering at the core of each height, the bed was very dilute (the total solid volume fraction was about 0.15 and likely to be less) since the 1.0 m height. This was the major cause of incomplete conversion of EtOH and other intermediates, confirming the results in table 4.17 and the contours of run 19 in figure 4.20. In case of run 14, the volume fraction profiles of each solid tended to develop to flat profiles (quite uniform) since 1.0 m height that faster than in run 19 and also were very dilute since this height in accordance with the axial profile in figure 4.24. These flat and very dilute profiles confirmed that flow pattern in run 14 was in dilute transportation and could be a cause of the lowest $H_2$ flux and the lowest $H_2$ purity. Hence, from both runs the concentration of each solid was the key hydrodynamics of performing SESRE in the CFBR riser.

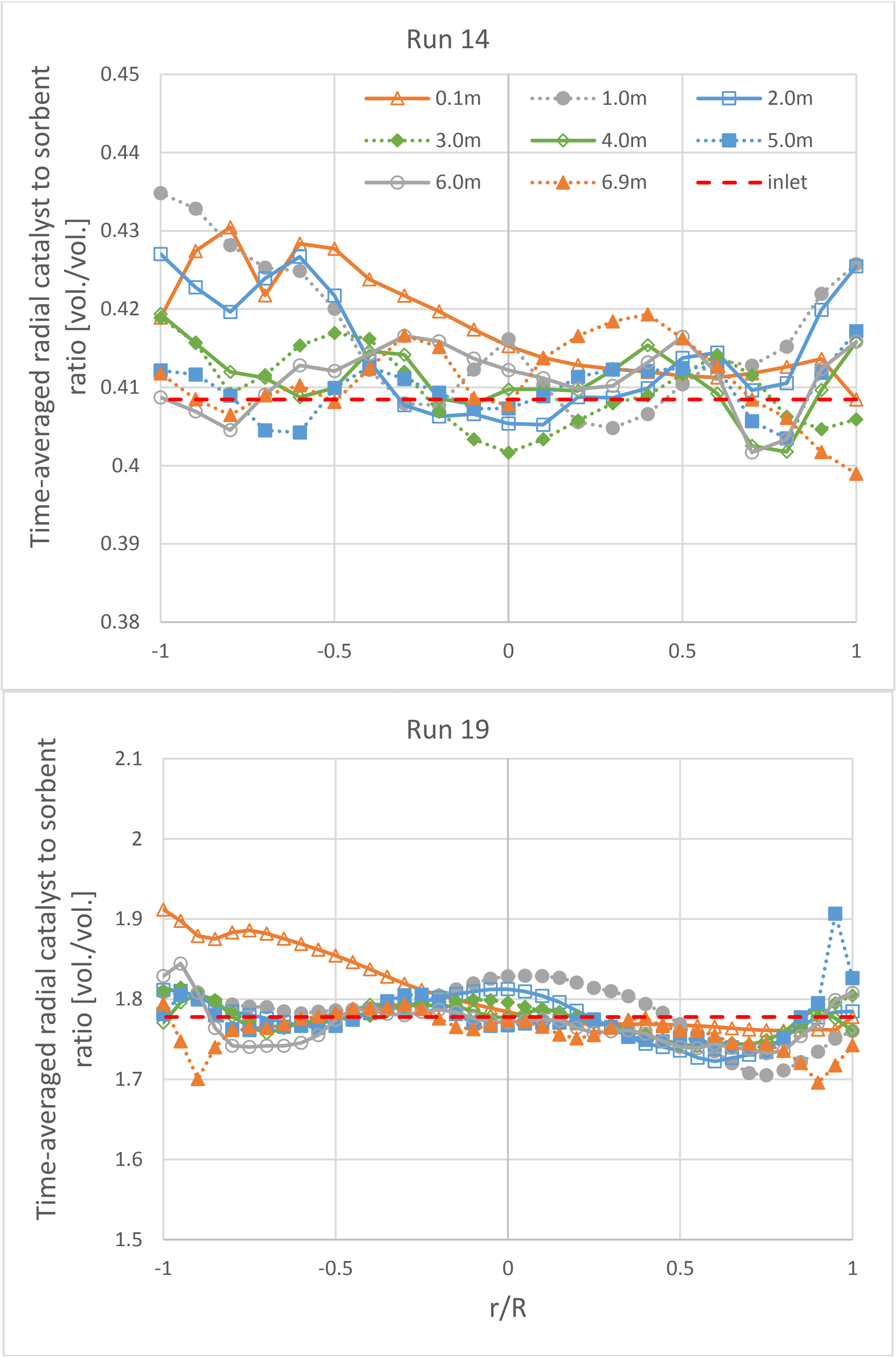

**Figure 4.27** The time-averaged radial profiles of volumetric catalyst to sorbent ratio at different heights of the SESRE riser in the best performance case (run 19) and the worst performance case (run 14).

In figure 4.27, the time-averaged radial profiles of volumetric catalyst to sorbent ratio at different heights in both runs were plotted comparing with the ratio where the solid entranced (1.778 vol./vol. in run 19 and 0.4085 vol./vol. in run 14). The profile of 0.1 m height in run 19 and profiles of 0.1-2.0 m height in run 14 near the left wall had little higher ratio than the inlet ratio. This is because solids entranced from the channel on the right wall with normal direction to the wall, so the heavier catalyst would flow directly to the left wall more than the sorbent. While the lighter sorbent would be lifted up at right zone more than the catalyst. However, the radial-averaged ratio of each height quite equaled to which of the entrance of solids. Thus, the mixing of the catalyst and the sorbent in radial direction was still good in both runs. Consistent with the axial profile of volumetric catalyst to sorbent ratio discussed previously in figure 4.25, the segregation between the catalyst and the sorbent did not cause incomplete performance of SESRE in this system.

Overall, the major cause of incomplete operations of SESRE in the CFBR system with these ranges of parameters was the dilute region in the core of the riser that made gas-solids contact insufficient before the gas leaving the riser. Even though the CFBR system with the best case still did not get the perfect SESRE performance, the $H_2$ purity could be raised highly up to 91.30% in dry basis by sorption enhancement. Comparing to the packed-bed reactor, which gas and solids had sufficient contacting time, SESRE could be performed perfectly with $H_2$ purity in dry basis of 96.2% in the experiment of Olivas *et al*. (2014) and 98.5% in validating simulation as shown in table 4.3. Thus, the CFB riser with better modifications of design and/or operation might get better gas-solid contact for perfect SESRE performance. However, the verifying experiments is suggested to confirm this system design as well.

## 4.4 Decarbonation performance in the regenerator system

### 4.4.1 The regenerator system design

After the regenerator reprocessed the lab-scale experiment in validation part, there were significant problems found from the results. Firstly, there was segregation zone, where the catalyst was denser and the sorbent was more dilute, in the right bottom corner of the reactor as shown in figure 4.28. This is because the catalyst (density of 2,200 kg/$m^3$) is heavier than the sorbent (density of 1,540 kg/$m^3$). Thus, the gas velocity had to be much higher than 0.056 m/s to avoid accumulation of the catalyst as well as segregation between the catalyst and the sorbent. Next, the single regenerator seemed not to be able to release all $CO_2$ off the sorbent, according to the results in table 4.4, because the atmosphere inside the regenerator was already saturated with $CO_2$. This was consistent with that partial pressure of $CO_2$ was significant effective parameter on the decarbonation rate (Okunev *et al.*, 2008).

The new system was modified by scaling up 20 times from the reactor width of 0.06 m to 1.20 m and the solid channel of 0.01 m to 0.20 m which equaled to designed diameter of the risers from both the reforming parts. The system also became double stage regenerator instead of the single stage regenerator to release more $CO_2$ off the sorbent as shown in figure 4.29. However, in this scale, the coming solids could not be thoroughly heated by hot wall of the top loop seal. Thus, there was an additional assumption that the coming solids was already preheated from some kind of unit. The top loop seal was also cut off to reduce demand of calculation. Because CaO conversion was averaged 1.48% with maximum fluctuated to 1.92% from the SESMR riser and averaged 0.84% with maximum fluctuated to 0.91% from the SESRE riser, the returning sorbent was assumed to get CaO conversion of 3% for further investigations in this part.

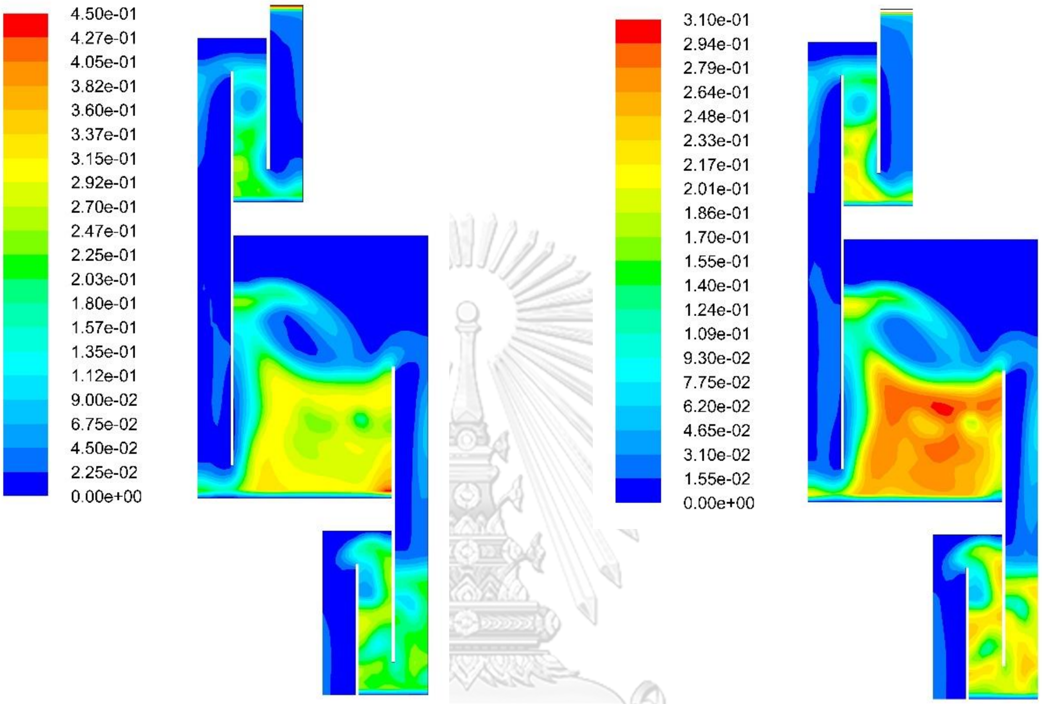

(a) Catalyst (b) Sorbent

**Figure 4.28** The instantaneous volume fraction of catalyst and sorbent at 45 s in the lab-scale regenerator which reprocessed the experiment of Arstad *et al.* (2009, 2012).

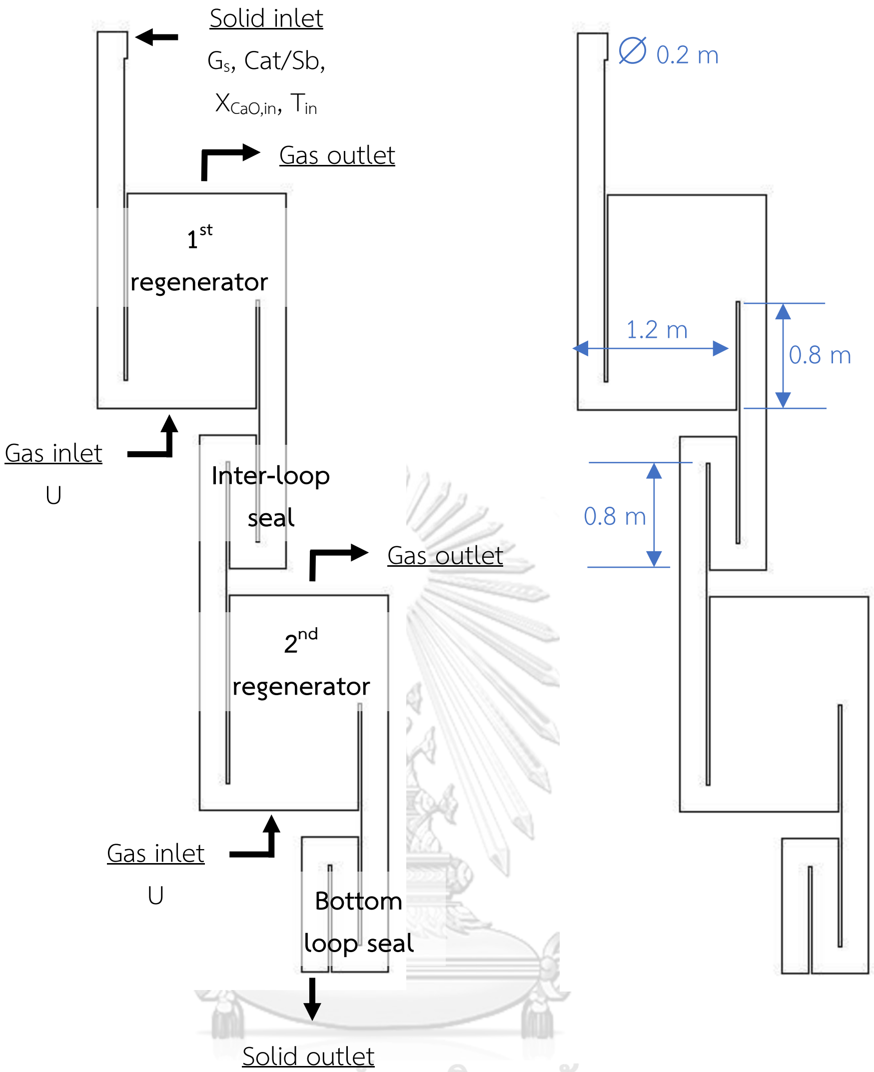

**Figure 4.29** The scale-up regenerator system and the effective parameters.

### 4.4.2 Time average and mesh refinement of the regenerator system

Figure 4.30 shows the averaged CaO conversion of sorbent at outlet which was the last point solid passed. This system operated with gas velocity of 0.1 m/s which would be the lowest velocity for further study and solid would take the longest time since had come from the inlet. At initial time, the CaO conversion was zero because the system had started with empty of solid. After the system was full of solids, the fluctuated results seemed steady since 50 s. Thus, a time-averaged range of 60–70 s would be used to average the simulation results in this part.

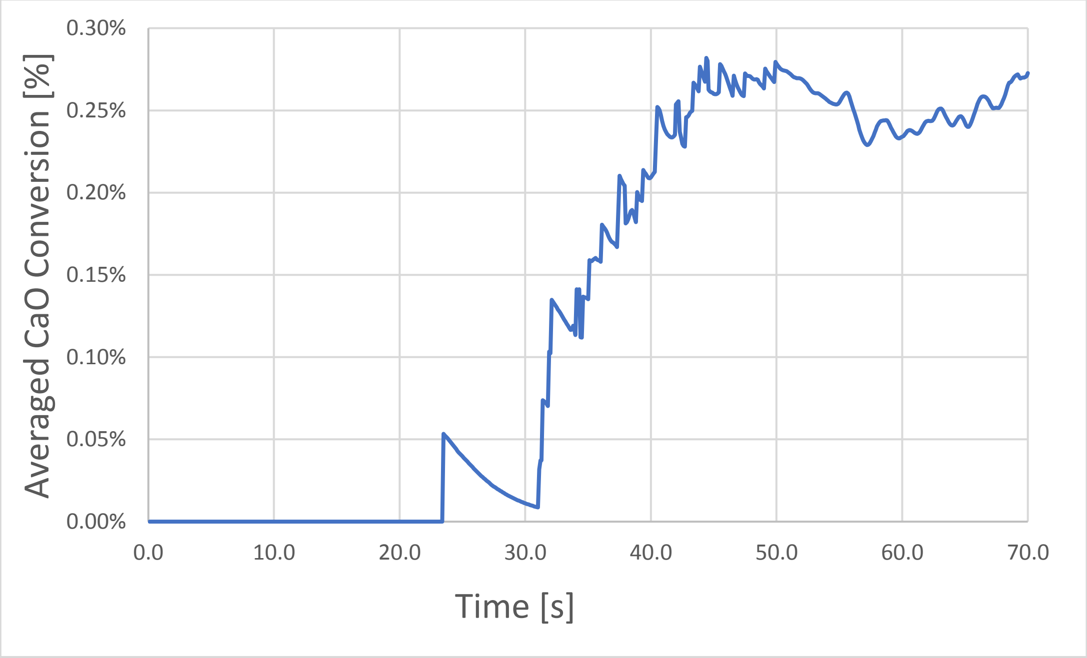

**Figure 4.30** The averaged CaO conversion of sorbent at outlet of the scale-up regenerator system as a function of time with U = 0.1 m/s.

The mesh refinement of the scale-up regenerator system was investigated with different sizes of cell ($\Delta x \cdot \Delta y$) as displayed in figure 4.31. The mesh comparison was done with results of the averaged CaO conversion and averaged temperature of sorbent in the bed of the 1$^{st}$ regenerator and the outlet $CO_2$ flux out of the 1$^{st}$ regenerator in time dependence as shown in figure 4.32. Ignore initial time of solid in coming about first 20 s, all results showed that the 80 mm x 80 mm size differed from the others and was not precise. Whereas the other sizes get along together but the 20 mm x 20 mm size was not chosen because the higher number of cells spent more calculating time. Thus, the mesh size of the 40 mm x 40 mm was sufficient fine for further simulations of this system.

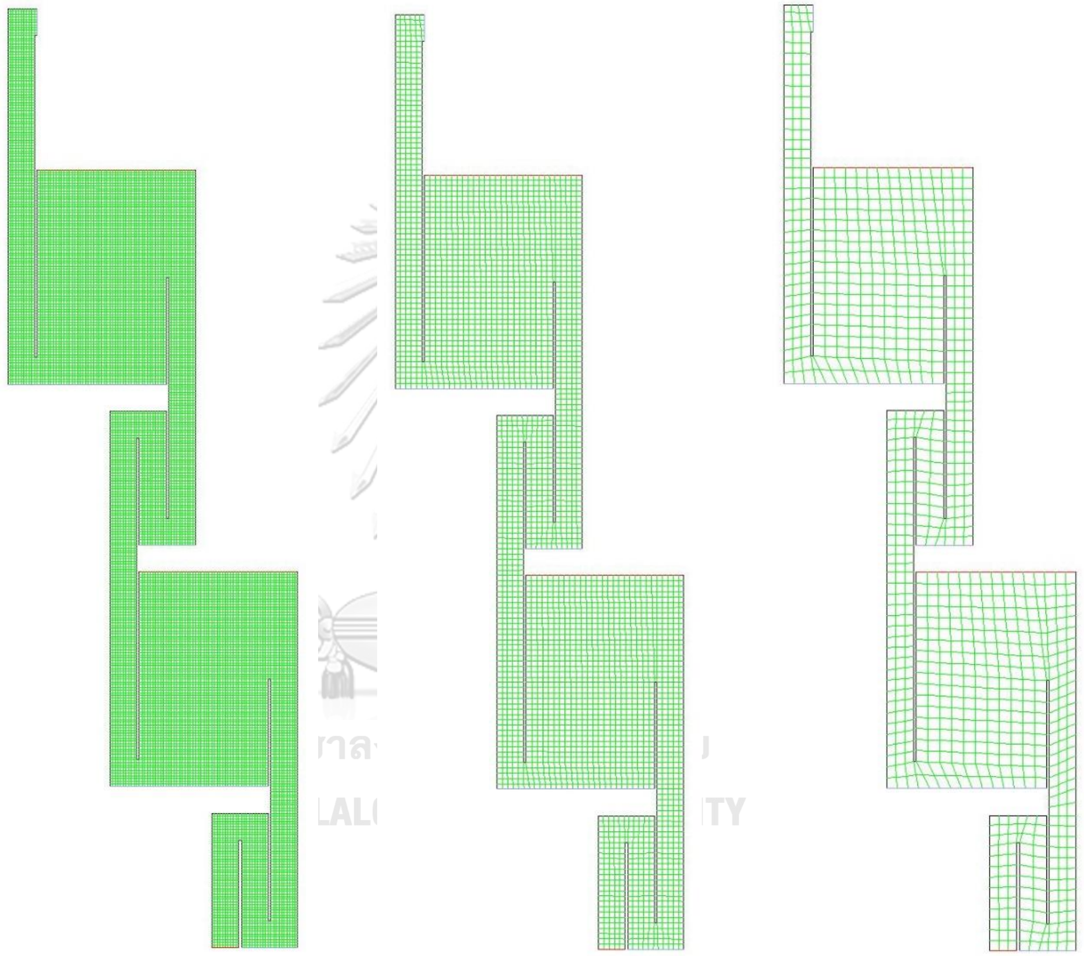

(a) 20mm x 20mm (b) 40mm x 40mm (c) 80mm x 80mm

**Figure 4.31** The scale-up regenerator system meshed with different cell sizes.

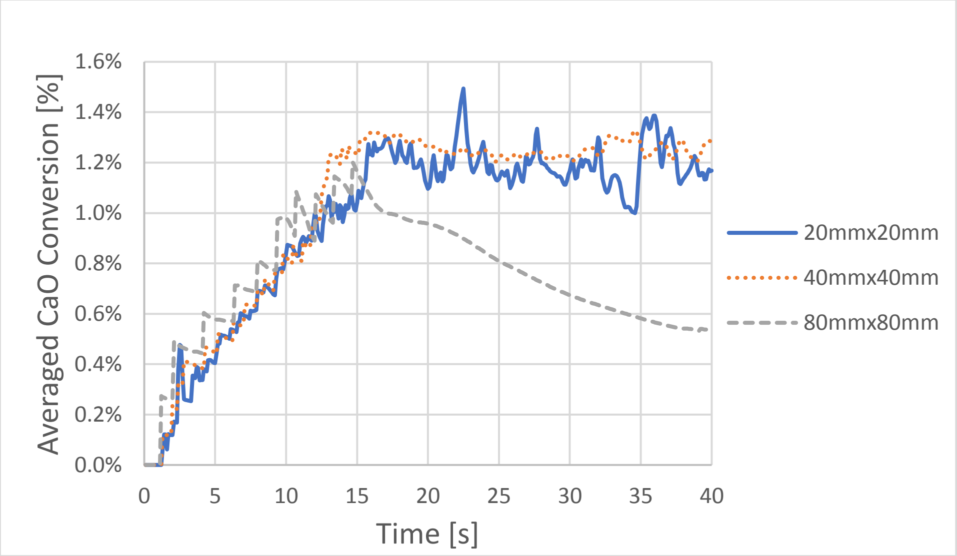

(a) Averaged CaO conversion of sorbent in the bed of the 1st regenerator

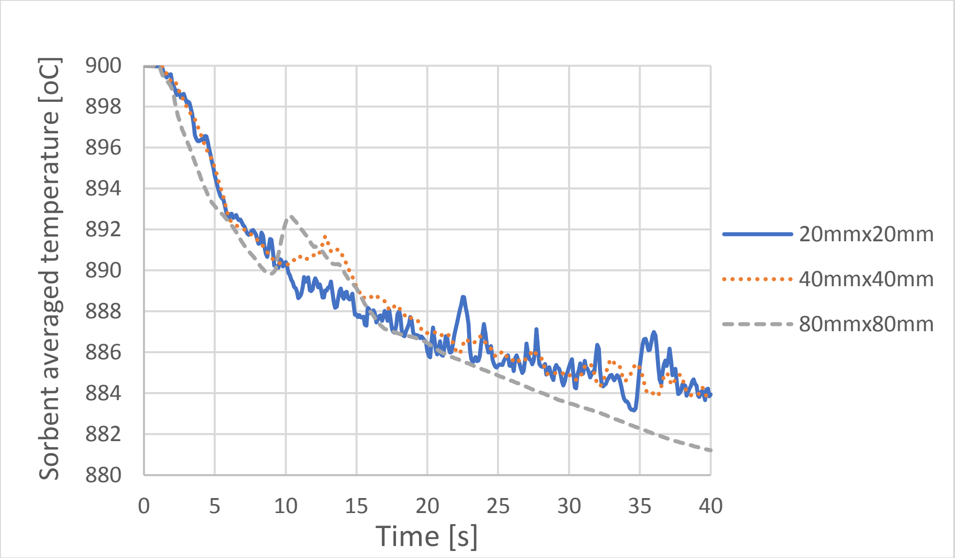

(b) Averaged temperature of sorbent in the bed of the 1st regenerator

**Figure 4.32** The averaged CaO conversion and sorbent temperature in the bed and the outlet $CO_2$ flux of the 1st regenerator as a function of time with different cell sizes resulted from the scale-up regenerator system.

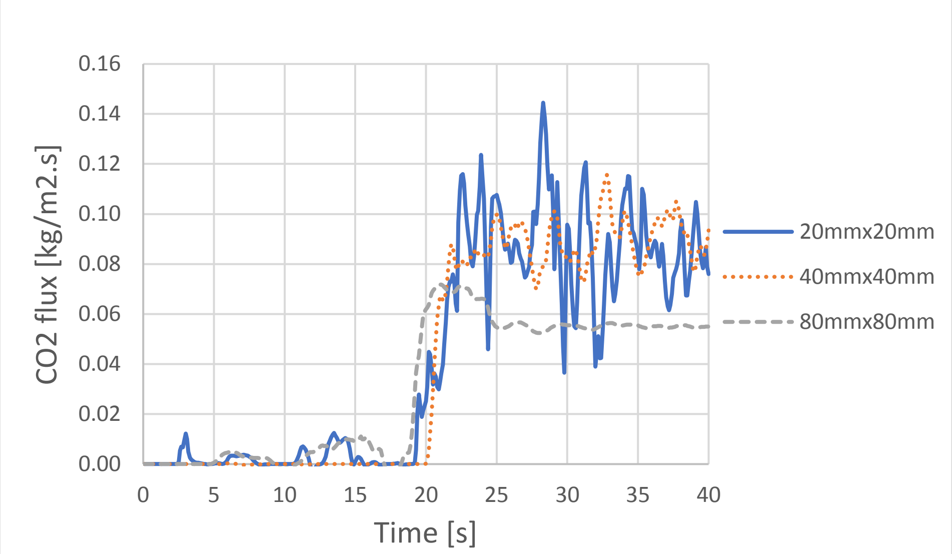

(c) $CO_2$ flux out of the 1st regenerator

**Figure 4.32** (continued)

### 4.4.3 Parametric study and hydrodynamics

From all concerning parameters in sorbent regeneration as previous described in figure 3.6, the solid flux, the catalyst to sorbent ratio and the CaO conversion of inlet sorbent were chosen a value from results of the risers design. Thus, there were only two parameters to investigate in this part, i.e the gas inlet velocity and the temperature of inlet solids. All fixed values and varied values of each parameters are shown in table 4.18.

**Table 4.18** The parameters chosen in the simulations of the scale-up regenerator system.

| Parameters | Value | |
|---|---|---|
| <u>Design parameters</u> | | |
| Gas inlet velocity (U) | 0.1, 0.2, 0.3 and 0.4 | m/s |
| Solid flux ($G_s$) | 200 (Chosen) | kg/m$^2$s |
| <u>Reaction parameters</u> | | |
| Catalyst to sorbent ratio (Cat/Sb) | 2.54 (Chosen) | kg/kg |
| Temperature of inlet solid ($T_{in}$) | 850, 900, 950 and 1,000 | °C |
| CaO conversion of inlet sorbent ($X_{CaO,in}$) | 3 (Chosen) | % |

The gas inlet velocity was the first parameter to be investigated. Figure 4.33 shows time- and area-averaged temperature and CaO conversion of sorbent at inlet, in bed of the 1st regenerator, in inter-loop seal, in bed of the 2nd regenerator and at outlet, in sequence. Both of temperature and CaO conversion of sorbent continuously decreased every position, especially in the 1st regenerator that the CaO conversion was reduced more than a half. There was no deviation of temperature among all gas velocities. The CaO conversion could be almost completely reduced at outlet whichever gas velocity was used. In comparison, results from the gas velocity of 0.3 m/s were very good as much as those of 0.4 m/s, and better than those of the other lower velocities. But when carefully investigated at gas outlet of both regenerators, it found that some amount of solids moved out of 2nd regenerator in some periods when using 0.3 m/s of the gas velocity as shown in figure 4.34. While the gas velocity of 0.4 m/s always blew the solids out of both regenerators.

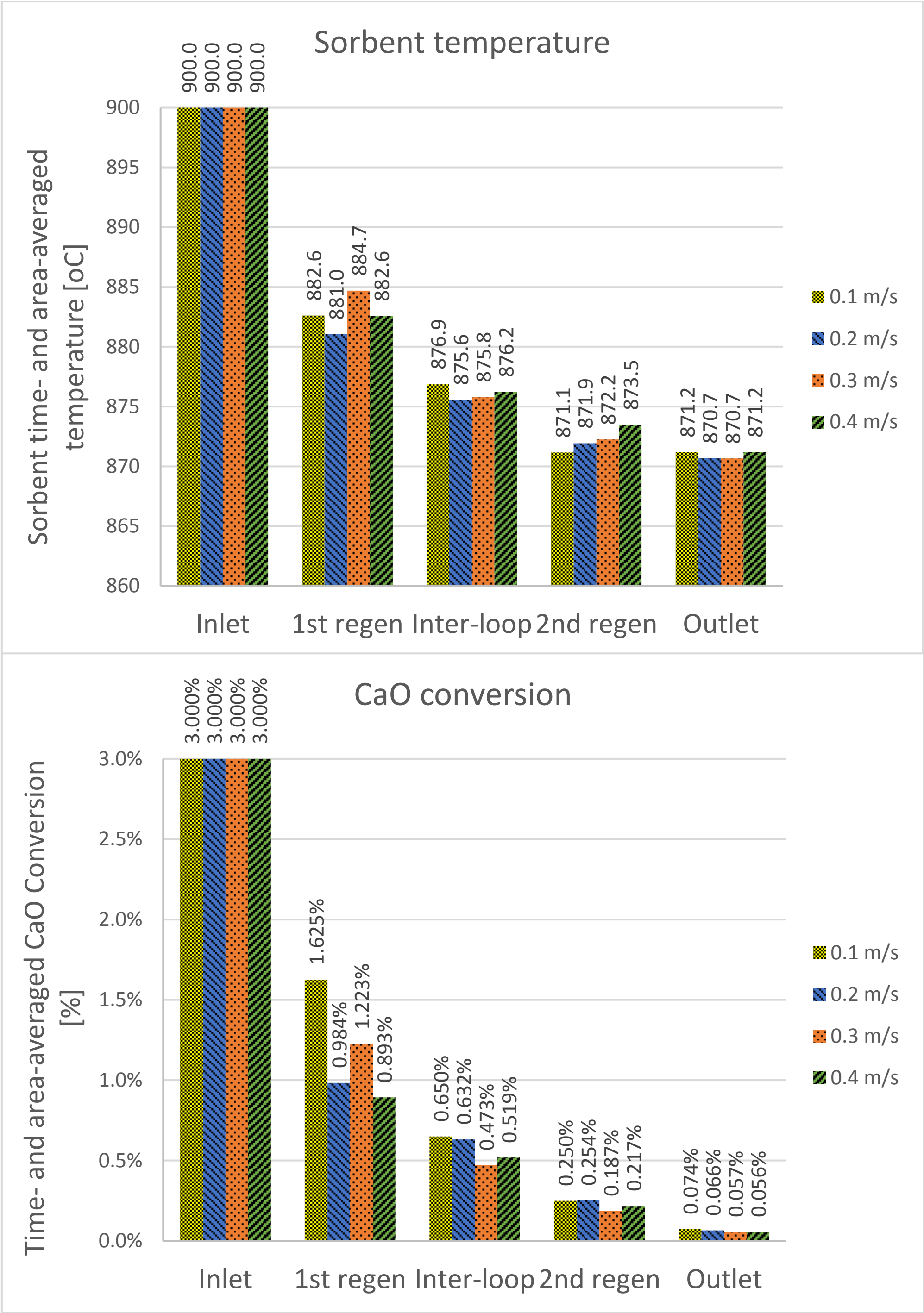

**Figure 4.33** The time- and area-averaged CaO conversion and temperature of sorbent at different positions in the scale-up regenerator system with various gas inlet velocities when $T_{in}$ = 900°C.

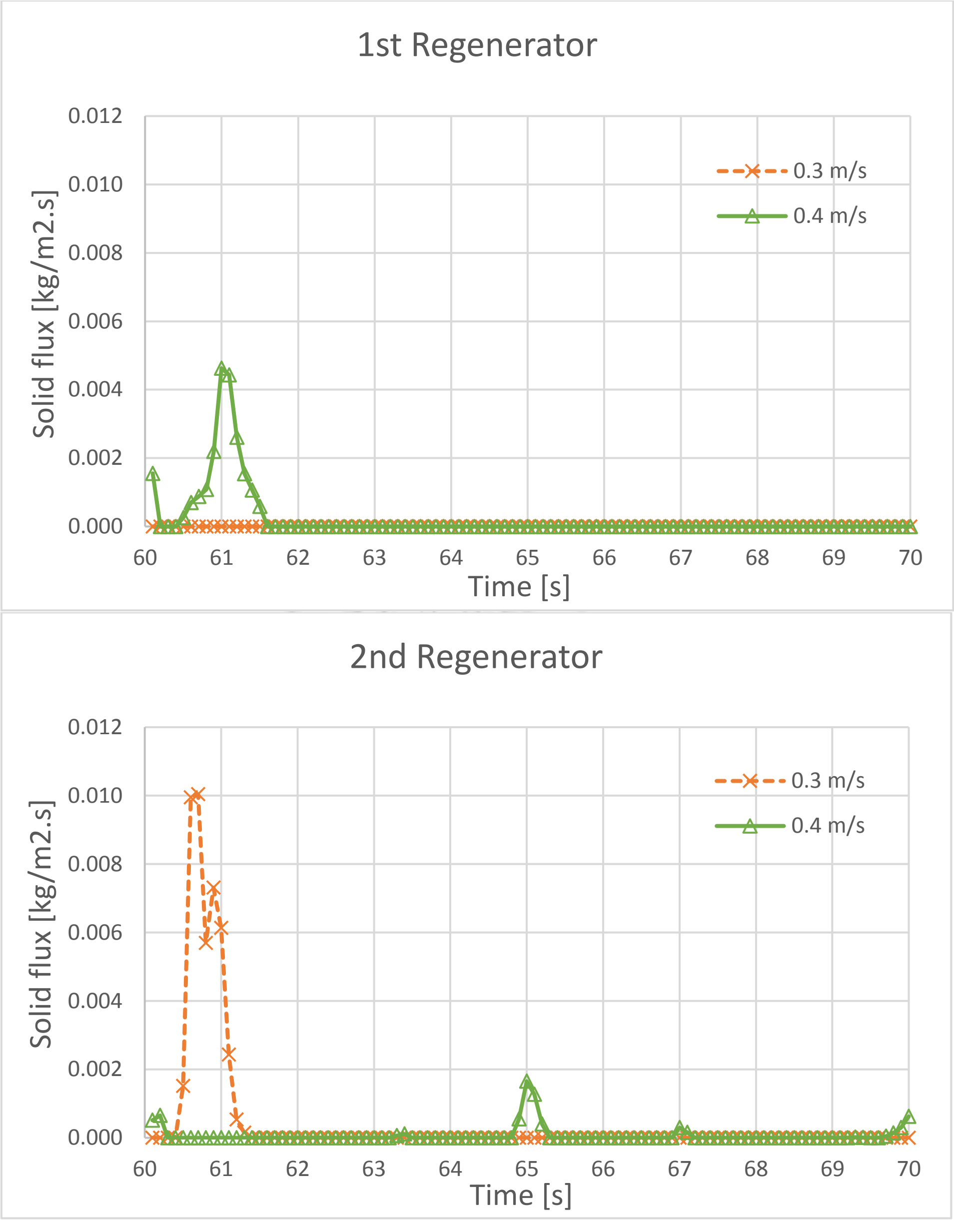

**Figure 4.34** The flux of solid blown out of the 1st regenerator and the 2nd regenerator in the scale-up regenerator system as a function of time with gas inlet velocities of 0.3 m/s and 0.4 m/s when $T_{in}$ = 900°C.

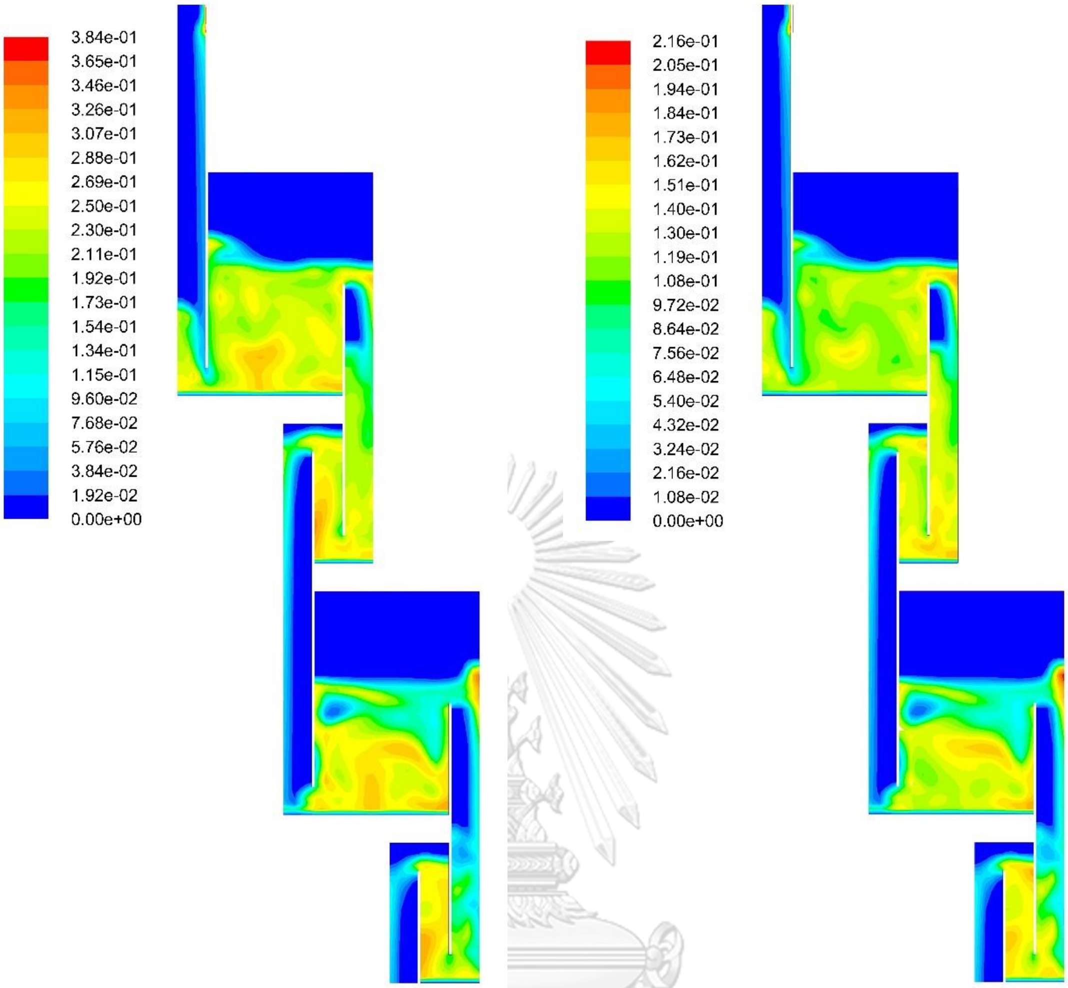

(a) Catalyst (b) Sorbent

**Figure 4.35** The instantaneous volume fraction of catalyst and sorbent at 70 s in the scale-up regenerator system in case of U = 0.2 m/s and $T_{in}$ = 900°C.

The gas velocity of 0.2 m/s could be the best choice because it had CaO conversion slightly less than the gas velocity of 0.1 m/s at the outlet, and obviously much better in the 1st regenerator. In addition, the gas velocity of 0.2 m/s was sufficiently higher than 0.056 m/s of gas velocity used in the lab-scale regenerator to prevent the accumulation of catalyst and segregation between the solids. This was also confirmed by figure 4.35 which shows instantaneous volume fraction contours of each solid phase in the scale-up regenerator system. Both contours visually looked similar in all zone unlike those contours at 45 s of the lab-scale regenerator as in figure 4.28, despite the fact that these contours were also at 70 s which took longer operation time.

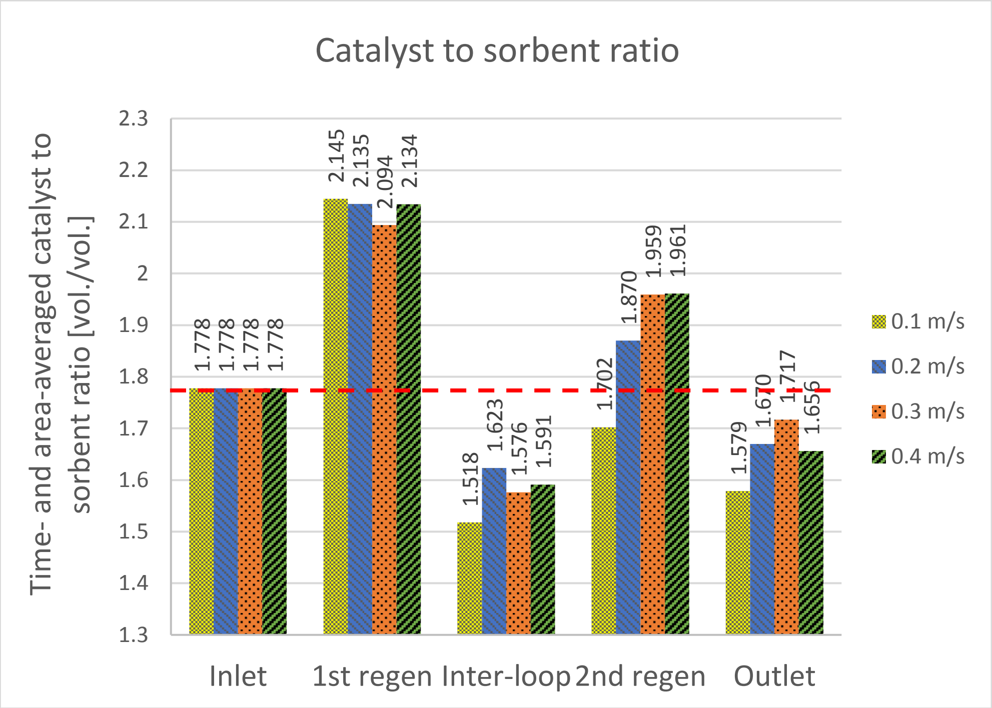

**Figure 4.36** The time- and area-averaged volumetric catalyst to sorbent ratio at different positions in the scale-up regenerator system with various gas inlet velocities when $T_{in}$ = 900°C.

Figure 4.36 shows time- and area-averaged volumetric catalyst to sorbent ratio at different positions with various gas inlet velocities compared with the ratio where the solid entranced (1.778 vol./vol.). The results show that there were deviations swinging in each position but there was no significant difference among the gas velocities. Although the catalyst had more proportion especially in the 1st regenerators, then the catalyst to sorbent ratio became closer to the inlet ration with slight deviation at the outlet. This could claim that the catalyst and the sorbent were mixed well throughout this regenerator system.

Investigating the rest parameter, inlet temperature of solids, the time- and area-averaged CaO conversion and temperature of sorbent are shown in figure 4.37. The averaged temperatures at the outlet of four cases decreased about 30-35°C from at the inlet due to endothermic reaction of decabonation, but still were much higher than 750°C of breakthrough point (Comas *et al.*, 2004). In comparison of inlet temperatures of solids, the results indicated that inlet temperature of 950°C and 1,000°C had satisfied CaO conversion, which was very close to zero, at the outlet. Thus, the inlet temperature of solids at 950°C could be sufficient for complete regeneration of the sorbent.

Overall, when the double stages regenerator system with the reactor width of 1.2 m operated with carrier gas velocity of 0.2 m/s and preheated returned solid at 950°C, the sorbent in solid mixture could be perfectly regenerated before returned into the reforming riser.

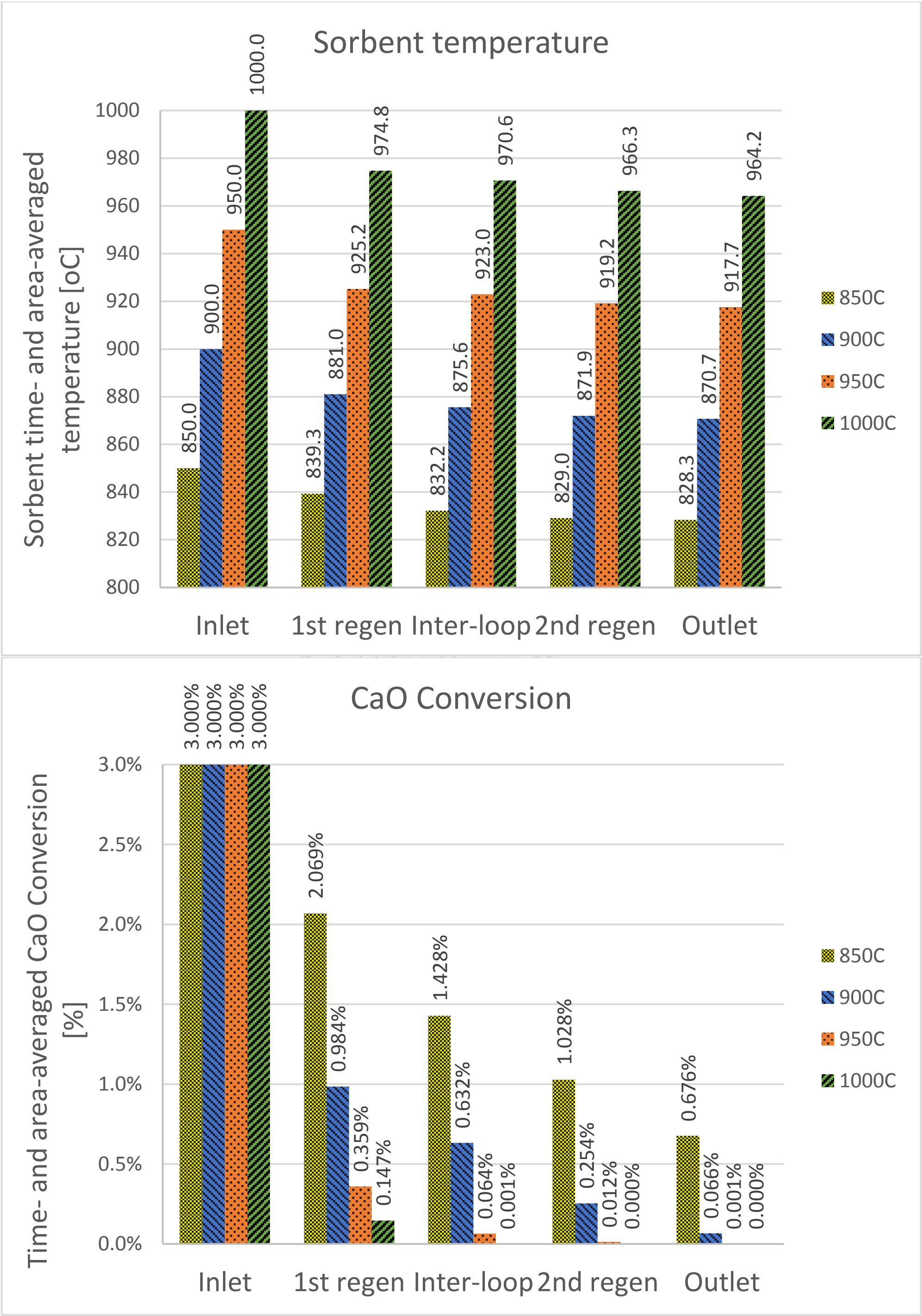

**Figure 4.37** The time- and area-averaged CaO conversion and temperature of sorbent at different positions in the scale-up regenerator system with various inlet temperatures of solid when U = 0.2 m/s.

# CHAPTER 5

# CONCLUSION AND RECOMMENDATIONS

## 5.1 Conclusion

Computational fluid dynamics (CFD) with two-dimensional transient models using Euler-Euler approach and kinetic theory of granular flows (KTGF) was applied for sorption enhanced steam methane reforming (SESMR) and sorption enhanced steam reforming of ethanol (SESRE) operating in a circulating fluidized bed reactor (CFBR) system. The solid in fluidized bed was a mixture of Ni-based catalyst and dolomite as sorbent. The aim of study was to design a proper pilot-scale CFBR system with suitable operating conditions for the highest $H_2$ production performance. The CFBR system design was separately investigated in 3 main units including a riser for SESMR, a riser for SESRE and a regenerator system supporting the risers. In the riser parts, the concerning parameters including riser diameter, inlet temperature, catalyst to sorbent ratio, solid flux and inlet gas velocity were examined with $2^5$ full factorial design and analysis of variance (ANOVA) to determine effects on $H_2$ flux and $H_2$ purity then optimized both of them. From ANOVA results of the SESMR riser, the gas velocity, the riser diameter and the solid flux, in descending order, were the most three significant parameters governing the $H_2$ flux and the $H_2$ purity. While in ANOVA of the SESRE riser, the riser diameter and the solid flux were the key parameters involved in both of the $H_2$ flux and the $H_2$ purity.

The best performance of the SESMR riser could get the $H_2$ purity reached equilibrium of 98.58% in dry basis with the highest $H_2$ flux of 0.301 kg/m$^2$s when operating with steam to carbon ratio of 4 mol/mol, gas velocity of 6 m/s, inlet temperature of 581°C. While the SESRE riser could get maximum $H_2$ purity only 91.30% in dry basis with the highest $H_2$ flux of 0.147 kg/m$^2$s when operating with Steam/Ethanol molar ratio of 6, gas velocity of 3 m/s, inlet temperature of 600°C. The best case of the SESMR riser and the SESRE riser had the same design with diameter of 0.2 m, height of 7 m operating with solid flux of 200 kg/m$^2$s and catalyst to sorbent ratio of 2.54 kg/kg. The hydrodynamics of both optimum cases showed that both SESMR and SESRE reached breakthrough within the bottom dense zone then gradually more developed in the core. But in difference, SESMR could be developed completely within 5.0 m height while SESRE could not. Because axial and radial distributions of solids were well developed with very good mixing of the catalyst and the sorbent. Thus, the dilute bed in the core of the riser was insufficient and actually caused incomplete conversion for SESRE but sufficient for SESMR.

Lastly in regenerator part, double-stage bubbling bed regenerators with 1.2 m width and 0.8 m height of bed could perfectly release $CO_2$ off the sorbent when operating with gas velocity of 0.2 m/s and preheating the solids at 950°C. This operation could also return the solids with good mixing of the catalyst and the sorbent as well. Overall, SESMR and SESRE had feasibility to continuously produce high purity hydrogen by this preferred design and conditions of CFBR system, which overcame fixed or bubbling bed reactors with higher production rate.

## 5.2 Recommendations

1) There were many ideal assumptions used in models of this study, so the good feasibility of the SESMR/SESRE performing in this CFBR system might be

overestimated. In the future works, some other models should replace their similar model for comparison. And experimental verifications are necessary as well.

2) These 2D models had been used for reducing computation times and could get precise results in quite symmetric and uniform sizing configurations such as the riser, which is a tube in practice. But the regenerator which actually has different sizes between the loop seal channel and the main reactor should be simulates in 3D models which preferable to asymmetric configuration for better design. Furthermore, if the whole system combining all units of CFBR is desired to be simulated, the cyclone is another recommended using 3D models because theoretically movement of solid in the cyclone use force vectors in three directions.

3) Attrition of solids is another concerning problem in high velocity fluidization. The attrition could deactivate both catalyst and sorbent in longer operation. Thus, the Ni-base catalyst and the dolomite should be further investigated about its attrition with the gas velocity around these range for modelling and/or in practice.

# REFERENCES

Abanades, J. C., E. J. Anthony, D. Y. Lu, C. Salvador and D. Alvarez (2004). "Capture of $CO_2$ from combustion gases in a fluidized bed of CaO." AIChE Journal **50**(7): 1614-1622.

ANSYS, I. (2013). ANSYS Fluent Theory Guide 15.0. USA, SAS IP, Inc.

Arstad, B., R. Blom, E. Bakken, I. Dahl, J. P. Jakobsen and P. Røkke (2009). "Sorption-enhanced methane steam reforming in a circulating fluidized bed reactor system." Energy Procedia **1**(1): 715-720.

Arstad, B., J. Prostak and R. Blom (2012). "Continuous hydrogen production by sorption enhanced steam methane reforming (SE-SMR) in a circulating fluidized bed reactor: Sorbent to catalyst ratio dependencies." Chemical Engineering Journal **189-190**: 413-421.

Barelli, L., G. Bidini, F. Gallorini and S. Servili (2008). "Hydrogen production through sorption-enhanced steam methane reforming and membrane technology: A review." Energy **33**(4): 554-570.

Callaghan, C. A. (2006). Kinetics and catalysis of the water-gas-shift reaction: A microkinetic and graph theoretic approach. Doctor of philosophy in chemical engineering, Worcester Polytechnic Institute.

Chalermsinsuwan, B., T. Samruamphianskun and P. Piumsomboon (2014). "Effect of operating parameters inside circulating fluidized bed reactor riser with ring baffles using CFD simulation and experimental design analysis." Chemical Engineering Research and Design **92**(11): 2479-2492.

Chao, Z., Y. Wang, J. P. Jakobsen, M. Fernandino and H. A. Jakobsen (2011). "Derivation and validation of a binary multi-fluid Eulerian model for fluidized beds." Chemical Engineering Science **66**(16): 3605-3616.

Chao, Z., Y. Wang, J. P. Jakobsen, M. Fernandino and H. A. Jakobsen (2012). "Numerical investigation of the sorption enhanced steam methane reforming in a fluidized bed reactor." Energy Procedia **26**: 15-21.

Chen, Y., Y. Zhao, C. Zheng and J. Zhang (2013). "Numerical study of hydrogen production via sorption-enhanced steam methane reforming in a fluidized bed reactor at relatively low temperature." Chemical Engineering Science **92**: 67-80.

Comas, J., M. Laborde and N. Amadeo (2004). "Thermodynamic analysis of hydrogen production from ethanol using CaO as a $CO_2$ sorbent." Journal of Power Sources **138**(1-2): 61-67.

Contreras, J. L., J. Salmones, J. A. Colín-Luna, L. Nuño, B. Quintana, I. Córdova, B. Zeifert, C. Tapia and G. A. Fuentes (2014). "Catalysts for $H_2$ production using the ethanol steam reforming (a review)." International Journal of Hydrogen Energy **39**(33): 18835-18853.

Cotton, A., K. Patchigolla and J. E. Oakey (2013). "Overview of, and experimental methodology for, sorption enhanced hydrogen production." Energy Procedia **37**: 2232-2244.

Cunha, A. F., Y. J. Wu, F. A. Díaz Alvarado, J. C. Santos, P. D. Vaidya and A. E. Rodrigues (2012). "Steam reforming of ethanol on a Ni/$Al_2O_3$ catalyst coupled with a hydrotalcite-like sorbent in a multilayer pattern for $co_2$ uptake." The Canadian Journal of Chemical Engineering **90**(6): 1514-1526.

Da Silva, A. L. and I. L. Müller (2011). "Hydrogen production by sorption enhanced steam reforming of oxygenated hydrocarbons (ethanol, glycerol, n-butanol and methanol): Thermodynamic modelling." International Journal of Hydrogen Energy **36**(3): 2057-2075.

De-Souza, M., G. M. Zanin and F. F. Moraes (2013). "Parametric study of hydrogen production from ethanol steam reforming in a membrane microreactor." Brazilian Journal of Chemical Engineering **30**(2): 355-367.

Di Carlo, A., E. Bocci, F. Zuccari and A. Dell’Era (2010). "Numerical investigation of sorption enhanced steam methane reforming process using computational fluid dynamics Eulerian-Eulerian code." Industrial & Engineering Chemistry Research **49**: 1561–1576.

Ebiad, M. A., D. R. Abd El-Hafiz, R. A. Elsalamony and L. S. Mohamed (2012). "Ni supported high surface area $CeO_2$–$ZrO_2$ catalysts for hydrogen production from ethanol steam reforming." RSC Advances **2**(21): 8145.

Gayubo, A. G., J. Vicente, J. Ereña, C. Montero, M. Olazar and J. Bilbao (2014). "Comparison of Ni and Co catalysts for ethanol steam reforming in a fluidized bed reactor." Catalysis Letters **144**(7): 1134-1143.

Gidaspow, D. (1994). Multiphase flow and fluidization: continuum and kinetic theory description. UK, ACADEMIC PRESS.

Harrison, D. P. (2008). "Sorption-enhanced hydrogen production: A review." Industrial & Engineering Chemistry Research **47**: 6486–6501.

Haryanto, A., S. Fernando, N. Murali and S. Adhikari (2005). "Current status of hydrogen production techniques by steam reforming of ethanol: A review." Energy & Fuels **19**: 2098-2106.

Hodapp, M. J., J. J. Ramirez-Behainne, M. Mori and L. Goldstein (2012). "Numerical studies of the gas-solid hydrodynamics at high temperature in the riser of a bench-scale circulating fluidized bed." International Journal of Chemical Engineering **2012**: 1-13.

Islam, A., S. H. Teo, E. S. Chan and Y. H. Taufiq-Yap (2014). "Enhancing the sorption performance of surfactant-assisted CaO nanoparticles." RSC Advances **4**(110): 65127-65136.

Joensen, F. and J. R. Rostrup-Nielsen (2002). "Conversion of hydrocarbons and alcohols for fuel cells." Journal of Power Sources **105**: 195-201.

Johnsen, K., J. R. Grace, S. S. E. H. Elnashaie, L. Kolbeinsen and D. Eriksen (2006). "Modeling of sorption-enhanced steam reforming in a dual fluidized bubbling bed reactor." Industrial & Engineering Chemistry Research **45**: 4133-4144.

Johnsen, K., H. J. Ryu, J. R. Grace and C. J. Lim (2006). "Sorption-enhanced steam reforming of methane in a fluidized bed reactor with dolomite as $CO_2$-acceptor." Chemical Engineering Science **61**(4): 1195-1202.

Kenarsari, S. D., D. Yang, G. Jiang, S. Zhang, J. Wang, A. G. Russell, Q. Wei and M. Fan (2013). "Review of recent advances in carbon dioxide separation and capture." RSC Advances **3**(45): 22739.

Koumpouras, G. C., E. Alpay, A. Lapkin, Y. Ding and F. Štěpánek (2007). "The effect of adsorbent characteristics on the performance of a continuous sorption-enhanced steam methane reforming process." Chemical Engineering Science **62**(18-20): 5632-5637.

Kunii, D. and O. Levenspiel (1991). Fluidization engineering. USA, Butterworth-Heinemann.

Kunii, D. and O. Levenspiel (1997). "Circulating fluidized-bed reactors." Chemical Engineerin Science **52**(15): 2471-2482.

Li, Z., N. Cai and J. Yang (2006). "Continuous production of hydrogen from sorption-enhanced steam methane reforming in two parallel fixed-bed reactors operated in a cyclic manner." Industrial & Engineering Chemistry Research **45**: 8788-8793.

Lin, J. S., M. M. Chen and B. T. Chao (1985). "A novel radioactive particle tracking facility for measurement of solids motion in gas fluidized beds." AIChE Journal **31**(3): 465–473.

Lindborg, H., M. Lysberg and H. A. Jakobsen (2007). "Practical validation of the two-fluid model applied to dense gas–solid flows in fluidized beds." Chemical Engineering Science **62**(21): 5854-5869.

Liu, F., Y. Qu, Y. Yue, G. Liu and Y. Liu (2015). "Nano bimetallic alloy of Ni–Co obtained from $LaCo_xNi_{1-x}O_3$ and its catalytic performance for steam reforming of ethanol." RSC Advances **5**(22): 16837-16846.

Liu, J. A. (2006). Kinetics, catalysis and mechanism of methane steam reforming. Master of science in chemical engineering, Worcester Polytechnic Institute.

Lysikov, A., V. Derevschikov and A. Okunev (2015). "Sorption-enhanced reforming of bioethanol in dual fixed bed reactor for continuous hydrogen production." International Journal of Hydrogen Energy **40**(42): 14436-14444.

Mahmoudi, S., C. W. Chan, A. Brems, J. Seville and J. Baeyens (2012). "Solids flow diagram of a CFB riser using Geldart B-type powders." Particuology **10**(1): 51-61.

Mas, V., M. L. Bergamini, G. Baronetti, N. Amadeo and M. Laborde (2008). "A kinetic study of ethanol steam reforming using a Nickel based catalyst." Topics in Catalysis **51**(1-4): 39-48.

Montgomery, D. C. (2012). Design and analysis of experiments. USA, John Wiley and Sons.

Mousa, M. B. M., S. E. K. Fateen and E. A. Ibrahim (2014). "Hydrodynamics of a novel design circulating fluidized bed steam reformer operating in the dense suspension upflow regime." ISRN Chemical Engineering **2014**: 1-13.

Ochoa-Fernandez, E., H. K. Rusten, H. A. Jakobsen, M. Ronning, A. Holmen and D. Chen (2005). "Sorption enhanced hydrogen production by steam methane reforming using $Li_2ZrO_3$ as sorbent: Sorption kinetics and reactor simulation." Catalysis Today **106**: 41-46.

Okunev, A. G., S. S. Nesterenko and A. I. Lysikov (2008). "Decarbonation rates of cycled CaO absorbents." Energy & Fuels **22**: 1911–1916.

Olivas, D. Y. A., M. R. B. Guerrero, M. A. E. Bretado, M. M. da Silva Paula, J. S. Gutiérrez, V. G. Velderrain, A. L. Ortiz and V. Collins-Martínez (2014). "Enhanced ethanol steam reforming by $CO_2$ absorption using CaO, CaO*MgO or $Na_2ZrO_3$." International Journal of Hydrogen Energy **39**(29): 16595-16607.

Ping, H. and S. Wu (2015). "Preparation of cage-like nano-$CaCO_3$ hollow spheres for enhanced $CO_2$ sorption." RSC Advances **5**(80): 65052-65057.

Prajongkan, Y. (2011). Three-dimentional simulation of hydrodynamics in riser of circulating fluidized bed reactor. Master of science program in fuel technology, Chulalongkorn University.

Ranade, V. V. (2002). Computational flow modeling for chemical reactor engineering. UK, ACADEMIC PRESS.

Rautio, A., P. K. Seelam, P. Mäki-Arvela, O. Pitkänen, M. Huuhtanen, R. L. Keiski and K. Kordas (2015). "Carbon supported catalysts in low temperature steam reforming of ethanol: study of catalyst performance." RSC Advances **5**(61): 49487-49492.

Rodrigues, A. E., Y. J. Wu, R. Faria and L. M. Madeira (2017). Sorption enhanced reaction processes. USA, World Scientific Publishing.

Rodríguez, N., M. Alonso and J. C. Abanades (2011). "Experimental investigation of a circulating fluidized-bed reactor to capture $CO_2$ with CaO." AIChE Journal **57**(5): 1356-1366.

Samruamphianskun, T., P. Piumsomboon and B. Chalermsinsuwan (2012). "Effect of ring baffle configurations in a circulating fluidized bed riser using CFD simulation and experimental design analysis." Chemical Engineering Journal **210**: 237-251.

Sánchez, R. A., Z. Chao, J. Solsvik and H. A. Jakobsen (2012). "One dimensional two-fluid model simulations of the SE-SMR process operated in a circulating fluidized bed reactor." Procedia Engineering **42**: 1282-1291.

Sánchez, R. A., Z. Chao, J. Solsvik and H. A. Jakobsen (2013). "An investigation of the heat integration between the two riser units constituting a circulating fluidized bed reactor for the SE-SMR process." Energy Procedia **37**: 1218-1227.

Sánchez, R. A. and H. A. Jakobsen (2012). Simulation of sorption enhanced steam methane reforming and chemical looping reforming in a circulating fluidized bed reactor. Ninth International Conference on CFD in the Minerals and Process Industries. Melbourne, Australia, CSIRO: 1-6.

Sánchez, R. A., J. Solsvik and H. A. Jakobsen (2012). "Modeling and simulation of cold flow fluidized bed reactors." Energy Procedia **26**: 22-30.

Sayyah, M., B. R. Ito, M. Rostam-Abadi, Y. Lu and K. S. Suslick (2013). "CaO-based sorbents for $CO_2$ capture prepared by ultrasonic spray pyrolysis." RSC Advances **3**(43): 19872.

Singh, R., M. K. Ram Reddy, S. Wilson, K. Joshi, J. C. Diniz da Costa and P. Webley (2009). "High temperature materials for $CO_2$ capture." Energy Procedia **1**(1): 623-630.

Solsvik, J., Z. Chao and H. A. Jakobsen (2012). "A one-dimensional two-fluid gas–solid model applied to fluidized bed reactors: The SMR and SE-SMR processes." Procedia Engineering **42**: 283-294.

Solsvik, J., Z. Chao, R. A. Sánchez and H. A. Jakobsen (2014). "Numerical investigation of steam methane reforming with $CO_2$-capture in bubbling fluidized bed reactors." Fuel Processing Technology **125**: 290-300.

Solsvik, J., R. A. Sánchez, Z. Chao and H. A. Jakobsen (2013). "Simulations of steam methane reforming/sorption-enhanced steam methane reforming bubbling fluidized bed reactors by a dynamic one-dimensional two-fluid model: Implementation issues and model validation." Industrial & Engineering Chemistry Research **52**(11): 4202–4220.

Song, S., Z. Hao, L. Dong, J. Li and Y. Fang (2016). "A bubble-based EMMS model for pressurized fluidization and its validation with data from a jetting fluidized bed." RSC Advances **6**(112): 111041-111051.

Sun, J., X. Qiu, F. Wu and W. Zhu (2005). "$H_2$ from steam reforming of ethanol at low temperature over Ni-$Y_2O_3$, Ni-$La_2O_3$ and Ni-$Al_2O_3$ catalysts for fuel-cell application." International Journal of Hydrogen Energy **30**(4): 437-445.

Sun, P., J. R. Grace, C. J. Lim and E. J. Anthony (2008). "Determination of intrinsic rate constants of the CaO–$CO_2$ reaction." Chemical Engineering Science **63**(1): 47-56.

Uriz, I., G. Arzamendi, P. M. Diéguez and L. M. Gandía (2013). Computational fluid dynamics as a tool for designing hydrogen energy technologies. Renewable hydrogen technologies. L. M. Gandía, G. Arzamendi and P. M. Diéguez. Poland, Elsevier B.V.**:** 401-435.

Vaidya, P. D. and A. E. Rodrigues (2006). "Insight into steam reforming of ethanol to produce hydrogen for fuel cells." Chemical Engineering Journal **117**(1): 39-49.

Vicente, J., C. Montero, J. Ereña, M. J. Azkoiti, J. Bilbao and A. G. Gayubo (2014). "Coke deactivation of Ni and Co catalysts in ethanol steam reforming at mild temperatures in a fluidized bed reactor." International Journal of Hydrogen Energy **39**(24): 12586-12596.

Wang, J., Y. Wang and H. A. Jakobsen (2014). "The modeling of circulating fluidized bed reactors for SE-SMR process and sorbent regeneration." Chemical Engineering Science **108**: 57-65.

Wang, Y., Z. Chao, D. Chen and H. A. Jakobsen (2011). "SE-SMR process performance in CFB reactors: Simulation of the $CO_2$ adsorption/desorption processes with CaO based sorbents." International Journal of Greenhouse Gas Control **5**(3): 489-497.

Wang, Y., Z. Chao and H. A. Jakobsen (2010). "3D Simulation of bubbling fluidized bed reactors for sorption enhanced steam methane reforming processes." Journal of Natural Gas Science and Engineering **2**(2-3): 105-113.

Wang, Y., Z. Chao and H. A. Jakobsen (2010). "CFD modelling of $CO_2$ capture in the SE-SMR process in the fluidized bed reactors." Chemical Engineering Transactions **21**: 601-606.

Wu, G., C. Zhang, S. Li, Z. Huang, S. Yan, S. Wang, X. Ma and J. Gong (2012). "Sorption enhanced steam reforming of ethanol on Ni–CaO–$Al_2O_3$ multifunctional catalysts derived from hydrotalcite-like compounds." Energy & Environmental Science **5**(10): 8942.

Wu, Y. J., P. Li, J. G. Yu, A. F. Cunha and A. E. Rodrigues (2013). "Sorption-enhanced steam reforming of ethanol on NiMgAl multifunctional materials: Experimental and numerical investigation." Chemical Engineering Journal **231**: 36-48.

Wu, Y. J., P. Li, J. G. Yu, A. F. Cunha and A. E. Rodrigues (2014). "High-purity hydrogen production by sorption-enhanced steam reforming of ethanol: a cyclic operation simulation study." Industrial & Engineering Chemistry Research **53**(20): 8515-8527.

Wu, Y. J., P. Li, J. G. Yu, A. F. Cunha and A. E. Rodrigues (2014). "Sorption-enhanced steam reforming of ethanol for continuous high-purity hydrogen production: 2D adsorptive reactor dynamics and process design." Chemical Engineering Science **118**: 83-93.

Wu, Y. J., J. C. Santos, P. Li, J. G. Yu, A. F. Cunha and A. E. Rodrigues (2014). "Simplified kinetic model for steam reforming of ethanol on a Ni/$Al_2O_3$ catalyst." The Canadian Journal of Chemical Engineering **92**(1): 116-130.

Xiu, G., P. Li and A. E. Rodrigues (2002). "Sorption-enhanced reaction process with reactive regeneration." Chemical Engineering Science **57**: 3893–3908.

Xu, J. and G. F. Froment (1989). "Methane steam reforming, methanation and water-gas shift: I.Intrinsic kinetics." AIChE Journal **35**(1): 88-96.

Yeoh, G. H. and J. Tu (2010). Computational techniques for multi-phase flows. UK, Elsevier Ltd.

Zhao, Z., P. Ren and W. Li (2016). "Supported Ni catalyst on a natural halloysite derived silica–alumina composite oxide with unexpected coke-resistant stability for steam-$CO_2$ dual reforming of methane." RSC Advances **6**(55): 49487-49496.

Zhu, J. (2010). "Circulating turbulent fluidization—A new fluidization regime or just a transitional phenomenon." Particuology **8**(6): 640-644.

# APPENDIX

# VITA

Mr. Kiattikhoon Phuakpunk was born on March 31, 1985 in Phitsanulok, Thailand. He finished secondary school from Phitsanulok Pityakom School, Phitsanulok, Thailand in 2000 and high school from Triam Udom Suksa School, Bangkok, Thailand in 2003. He graduated with a bachelor degree in chemical engineering from Chulalongkorn University, Bangkok, Thailand in 2007. He received master degree of engineering in energy technology from King Mongkut' s University of Technology Thonburi, Bangkok, Thailand in 2012.